

EXPERIMENTAL IMPACT TESTING AND ANALYSIS OF COMPOSITE FAN CASES

By

Andrew Joe Vander Klok

A DISSERTATION

Submitted to
Michigan State University
in partial fulfillment of the requirements
for the degree of

Mechanical Engineering - Doctor of Philosophy

2016

ABSTRACT

EXPERIMENTAL IMPACT TESTING AND ANALYSIS OF COMPOSITE FAN CASES

By

Andrew Joe Vander Klok

For aircraft engine certification, one of the requirements is to demonstrate the ability of the engine to withstand a fan blade-out (FBO) event. A FBO event may be caused by fatigue failure of the fan blade itself or by impact damage of foreign objects such as bird strike. An uncontained blade can damage flight critical engine components or even the fuselage. The design of a containment structure is related to numerous parameters such as the blade tip speed; blade material, size and shape; hub/tip diameter; fan case material, configuration, rigidity, etc. To investigate all parameters by spin experiments with a full size rotor assembly can be prohibitively expensive. Gas gun experiments can generate useful data for the design of engine containment cases at much lower costs. To replicate the damage modes similar to that on a fan case in FBO testing, the gas gun experiment has to be carefully designed.

To investigate the experimental procedure and data acquisition techniques for FBO test, a low cost, small spin rig was first constructed. FBO tests were carried out with the small rig. The observed blade-to-fan case interactions were similar to those reported using larger spin rigs. The small rig has the potential in a variety of applications from investigating FBO events, verifying concept designs of rotors, to developing spin testing techniques. This rig was used in the developments of the notched blade releasing mechanism, a wire trigger method for synchronized data acquisition, high speed video imaging and etc. A relationship between the notch depth and the release speed was developed and verified. Next, an original custom designed spin testing facility was constructed. Driven by a 40HP, 40,000rpm air turbine, the spin rig is housed in a

vacuum chamber of $\Phi 72\text{in} \times 40\text{in}$ ($1829\text{mm} \times 1016\text{mm}$). The heavily armored chamber is furnished with 9 viewports. This facility enables unprecedented investigations of FBO events.

In parallel, a 15.4ft (4.7m) long $\Phi 4.1\text{inch}$ (105mm) diameter single stage gas gun was developed. A thermodynamic based relationship between the required gas pressure and targeted velocity was proposed. The predicted velocity was within $\pm 7\%$. Quantitative measurements of force and displacement were attempted. The transmitted impact force was measured with load cells. The out-of-plane deformation was measured with a projection grating profilometry method.

The composite panels and fan cases used in this work were made of S2-glass plain weave fabrics with API SC-15 toughened epoxy resin using the vacuum assisted resin transfer molding (VARTM) method. Using the gas gun, the impact behavior of the composite was investigated at velocities ranging from 984ft/s to 1502ft/s (300m/s to 458m/s) following a draft ASTM testing standard. To compare the ballistic protection capability of different materials, a new parameter E_{BL} , the projectile kinetic energy at the target ballistic limit normalized by the contact area of the projectile, was proposed. S2-glass/epoxy composite is ranked very high in E_{BL} per areal weight.

Finally, a testing method for replicating spin pit testing with a gas gun test was developed. Major differences between the two tests are the initial conditions of the blade upon contact with the target. In spin testing, the released blade has two velocity components, rotational and translational whereas in gas gun testing, the projectile has only the translational velocity. To account for the influence of the rotational velocity, three projectile designs were experimentally investigated. The results show that to generate similar damage modes in gas gun testing, it is critical to ensure the deformation of the projectile before testing is similar to that of a released blade. With the pre-bent blade, the gas gun experiment was able to replicate the damage modes of the fan case in FBO test on flat composite panels.

Copyright by
ANDREW JOE VANDER KLOK
2016

ACKNOWLEDGEMENTS

I would like to express my gratitude to my major advisor Dr. Xinran Xiao for her guidance, support, and expertise in all works accomplished. I would also like to show my appreciation for all the love, support, and patience from friends and family during this project especially to the love of my life Dr. Amy Lynn Montague. Additionally, I thank Andy Stamm, Ryan Dutour, and Matthew Auvenshine for supporting and making possible all of the experimental work. Also, I thank Dr. Tim Luchini and Steve Sommerlot for producing an enjoyable environment in the laboratory. All project planning as well as careful guidance throughout the phases of the project were assisted by Jim Dorer. Without his expertise, key aspects of this project would not be possible. Thank you Jim! This work is supported by NASA Glenn Research Center's Dr. Mike Pereira, and Dr. Gary Roberts through grant NNX12AL14A. Thank you both for your guidance and support.

TABLE OF CONTENTS

LIST OF TABLES	vii
LIST OF FIGURES	ix
KEY TO SYMBOLS OR ABBRIVIATIONS	xv
CHAPTER 1 INTRODUCTION	1
1.1 Problem Definition.....	2
1.2 Research Objective	4
1.3 Approach.....	5
1.4 Scope of Work	5
1.5 Executive Summary	6
CHAPTER 2 BACKGROUND INFORMATION	7
2.1 Initial Blade Dynamics	8
2.2 Ballistic Impact	11
2.3 Impact Response of Composite Structures	12
2.4 Ballistic Limit	15
CHAPTER 3 FAN-BLADE-OUT EXPERIMENT AT SMALL SCALE	16
3.1 Introduction.....	17
3.2 Experimental Setup.....	18
3.2.1 Spin Rig	18
3.2.1.1 Notched Blade Release Mechanism.....	20
3.2.1.2 Testing Articles	22
3.2.1.3 Data Acquisition	23
3.2.2 Blade Release Prediction	24
3.2.3 FBO Response	25
3.3 Conclusions.....	29
3.4 Summary.....	30
CHAPTER 4 INVESTIGATION OF HIGH VELOCITY IMPACT RESPONSES OF COMPOSITE PANELS WITH A GAS GUN	31
4.1 Introduction.....	32
4.2 Experimental Setup.....	33
4.2.1 Gas Gun	33
4.2.3 Projectile Velocity Measurement.....	35
4.2.4 Gas Pressure and Impact Velocity	36
4.2.5 Transmitted Impact Force Measurement	42
4.2.6 Out-of-Plane Deformation Measurement	44
4.2.7 Composite Panel Manufacturing.....	45

4.2.8 Post-mortem Inspection	46
4.3 Results and Discussion	46
4.3.1 Ballistic Limit	48
4.3.2 Force and Deformation Histories.....	49
4.3.3 Energy Absorption.....	54
4.3.4 Damage and Failure Mode Analysis.....	54
4.3.5 Comparison of Energy Absorption at Ballistic Limit.....	58
4.4 Conclusions.....	60
4.5 Summary.....	61
CHAPTER 5 COMPARISON OF IMPACT DAMAGE FROM SPIN PIT AND FLAT PANEL GAS GUN TESTING.....	63
5.1 Introduction.....	64
5.2 Experimental Setup.....	65
5.2.1 Spin Pit Set-up and FBO Experiment	65
5.2.2 Gas Gun Set-up.....	69
5.2.3 Manufacturing Composite Panels and Fan Cases.....	71
5.2.4 Out-of-Plane Deformation Measurement	72
5.2.5 Damage evaluation by frequency measurements.....	73
5.3 Projectile Design for Gas Gun Experiments.....	75
5.3.1 Spin pit and gas gun projectile velocity characterization	75
5.3.2 Projectile/target interactions	76
5.3.3 Projectile Design for Flat Panel Gas Gun Testing.....	77
5.3.3.1 Method I: blade segment.....	77
5.3.3.2 Method II: energy-based similitude design.....	77
5.3.3.3 Method III: pre-bent projectile.....	81
5.4 Results and Discussions.....	86
5.4.1 Spin pit testing	86
5.4.2 Gas Gun experiments.....	89
5.4.3 Comparison of gas gun and spin tests.....	91
5.5 Conclusion	97
CHAPTER 6 CONCLUSION.....	98
6.1 Concluding Remarks.....	99
6.2 Contributions.....	100
6.3 Future work.....	101
6.3.1 Testing of additional material systems	101
6.3.2 Blade-to-blade interaction investigation.....	101
6.3.3 Optimizing thickness for maximum energy absorption with strain energy assumptions.....	101
APPENDICES	103
Appendix A: Gas gun operation manual.....	104
Appendix B: Spin pit user manual and technical notes	110
Appendix C: Flat plate VARTM manufacturing	126
REFERENCES	131

LIST OF TABLES

Table 1 material and geometric parameters of Aluminum fan blade.....	22
Table 2 geometrical parameters for blades as received and after modification M1 and M2.....	22
Table 3 experiments conducted with cooling fan	24
Table 4 camera specifications.....	36
Table 5 initial and calculated parameters of the gas gun system. Items on the left are known, and items on the right are calculated through the solution process. For IT_6 through IT_10, use V_1^* and V_2^* from earlier gas gun setup.....	40
Table 6 predicted velocity of projectiles at different gases for $m_p=183.5g$, $p_1=1.02MPa$	40
Table 7 predicted ($n=1.26$) and measured impact velocity versus the gas pressure	41
Table 8 gas gun experimental results.....	48
Table 9 data sources for Figure 31.....	59
Table 10 method III list of variables.....	85
Table 11 results of spin tests; highlighted is test being matched with gas gun testing.....	87
Table 12 Summary of the gas gun testing with flat panel.....	90

LIST OF FIGURES

Figure 1 the centrifugal force on a rotating fan blade [10]	9
Figure 2 the velocity profile of a rotating blade before (a) and after (b) blade release.	9
Figure 3 numerical simulation of a blade release event at 40,000 RPM. (a) A release blade at the moment before impacting the fan case. (b) The tangential and radial velocities of the released blade at nodal locations indicated on the blade at the moment when the marked node came in contact with the fan case wall.	10
Figure 4 definition of impact velocity range.....	11
Figure 5 projectile with yaw, pitch and roll motion is moving from the left to right. The target obliquity is α	12
Figure 6 schematic of the small spin pit rig.....	19
Figure 7 (a) Assembled small spin rig: the setup of motor, gearbox and the vacuum chamber. (b) An aluminum cooling fan is held in with a steel shaft inside a steel fan case. The assembly is installed inside the vacuum chamber.	19
Figure 8 schematic shows that sections of blade dr at radius distance r , under an angular speed of ω resulting in a centrifugal force F_c on the section.	21
Figure 9 trigger wire mechanism and fan blade system.	24
Figure 10 comparison of the predicted release speed (lines) and experimental results (symbols) for cooling fan blades with and without modification.	25
Figure 11 the hoop strain on the fan case in fan blade release (FBO) experiment with a cooling fan. The blade was released at 16,135 RPM. There was no interaction between the release blade and other blades.	27
Figure 12 the hoop strain on the fan case in FBO experiment with a cooling fan. The blade was released at 17,021 RPM. The FBO was followed by hub failure.	28
Figure 13 the hoop strain on the fan case in FBO experiment with a modified cooling fan. The blade was released at 17,026 RPM. The blade to blade interaction was observed.	29
Figure 14 the schematic of a single stage gas gun. Camera #1 phantom V12 for determining the projectile initial velocity and orientation. Camera #2 phantom V7 for determining the projectile residual velocity and the out-of-plane deformation using a projection grating profilometry method.....	34

Figure 15 (a) the gas gun used in experiment. The gun barrel length is 4.7m (15.5 ft) long with an inner diameter of 108mm (4.25 in). (b) The poppet valve is made of Mylar with embedded Nichrome wire and a spent valve shown bottom. (c) The sabot is made of polylactic acid (PLA) and features a recess to hold projectile in position by press fit. (d) An aluminum 60g projectile machined to a flat on both ends.	35
Figure 16 determining projectile velocity using high speed video footage. Shown left is a calibration image taken before testing with scale in direct flight path of projectile. Shown right is the projectile moving right to left towards target.	36
Figure 17 flowchart describing the solution process to get vessel pressure. The final equation can be solved for the absolute pressure, p_1 . To find the gage pressure needed after vacuuming the gun barrel, subtract the vacuum pressure from p_1	39
Figure 18 predicted and measured impact velocity	41
Figure 19 (a) the four resistance strain gage load cells and their mounting in the target retainer system. (b) Close up view of a load cell. (c) Load cell schematic for full bridge configuration where two diametrically opposing gages are mounted off axial direction as denoted by $-v\epsilon$ where v is Poisson's Ratio.....	43
Figure 20 isometric view of testing frame with panel installed. The thin wire in center of panel provides a switch for triggering and synchronizing of data acquisition equipment. On the right is a schematic of the circular frame with a 24 count hole pattern on a radius of 136.5mm (5.375in), specimen test radius of 127.0mm (5in), and test area of 0.05067m^2	44
Figure 21 the schematic of the projection grating profilometry experimental setup for the out-of-plane deformation measurement.	45
Figure 22 manufacturing composite panels using VARTM Process.....	46
Figure 23 material ballistic limit is determined at the x-axis intercept of a linear trend line from residual vs. initial velocities	49
Figure 24 the force history traces recorded by the load cell. The force is the summation of four load cells.....	50
Figure 25 the recorded peak force versus the impact velocity of the projectile.	51
Figure 26 3D profile of the back side of the panel during impact testing under the ballistic limit. The 10 ply panel (IT_10) reached the maximum displacement $136\mu\text{s}$ before the 6 ply panel (IT_8).....	53
Figure 27 the maximum displacement on non-perforated 6 and 10-ply panels.....	54
Figure 28 energy absorption vs initial projectile velocity.	56

Figure 29 the inspection of tested panels with LED backlight. The surface shown is the impact face.	58
Figure 30 the back side of the composite panel from IT_12, 6-ply panel tested at 458m/s: dry fiber tows are protruded and form a hut shaped sub-structure.	58
Figure 31 comparison of E_{BL} , the energy absorbed by the target material at the ballistic limit normalized by the contact area, versus the areal weight of the target. Material tested in this work is identified by arrows.....	60
Figure 32 spin pit test facility: (a) vacuum chamber and testing rig; (b) schematic of the armored layers; and (c) data acquisition for fringe projection and axial high speed camera, air turbine controller, temperature and accelerometer health monitoring of rotating assembly. (d) A composite fan case is attached by clamps.	66
Figure 33 cross-sectional view of the rotating assembly including bearing house back structure and fan case (left). Assembled inner housing structure (right).....	68
Figure 34 rotor and shaft assembly with a full set of blades, and the cross-sectional dimensions (in mm) of the blade.	68
Figure 35 the schematic of a single stage gas gun. Camera #1 phantom V12 for determining the projectile initial velocity and orientation. Camera #2 phantom V7 for determining the projectile residual velocity and the out-of-plane deformation using a projection grating profilometry method.....	70
Figure 36 (a) the single stage gas gun. The gun barrel length is 4.7m (15.5 ft) long with an inner diameter of 108mm (4.25 in). (b) The sabot with a titanium blade secured at a 45° orientation. (c) The back side of the composite plate with fringe projection. (d) The impact side of the panel where a 76.2mm (3 in.) wide strip of composite is exposed. The plate is bolted to a testing fixture through two steel bars to replicate the clamped boundary condition for the fan case in Figure 32d.....	71
Figure 37 manufacturing composite articles using VARTM Process. For composite fan cases, Al liner was used as the tool plate.	72
Figure 38 schematic of the projection grating profilometry experimental setup for the out-of-plane deformation measurement.	73
Figure 39 experimental set-up for frequency response measurement.	74
Figure 40 comparison of the velocity profile of a released blade in spin test to that of a projectile in gas gun test.	76
Figure 41 mass, velocity and energy profiles of a wedge shaped blade in spin testing. Longer arrow length corresponds to a larger magnitude.	79

Figure 42 the thickness profile of the projectile for energy-based similitude design	80
Figure 43 bending of the blade in spin testing can be simplified as a beam being subjected to 3-point bend. The free body diagram is for the instance when the blade tip becomes in contact with the fan case wall. Here, R_{cg} is a reaction force developed at the blade center of gravity cg. l_a is the distance from the blade root or failure point to the blade cg and l_b is the distance from cg to the blade tip.	82
Figure 44 free body diagram of blade geometry along chord length to determine moment equations M1 from left (a) and M2 right (b).....	83
Figure 45 pre-bending a blade using a 3 point fixture on the Instron 1321 testing frame (left) and the finished pre-bent blade (right).....	86
Figure 46 high speed images of FBO spin test of sp_2 and sp_4. The rotor rotates clockwise.....	88
Figure 47 the schematic shows the initial contact of the blade with the fan case and the subsequent deformation and motion of the blade observed in FBO spin test. This results in two damage regions on the fan case separated by the pitching point of the blade.	89
Figure 48 high speed images of the gas gun experiment with Method I, Test 3. From left to right: blade before impact ($0\mu s$), tip impact ($115\mu s$), blade bending ($346\mu s$), and scraping ($653\mu s$). As seen, the blade tip strikes the panel, bends, and slides	91
Figure 49 high speed images of the gas gun experiment, Method II, Test 4. The blade tip strikes the panel and goes straight through ($154\mu s$ after the left image).	91
Figure 50 comparison of deformed projectiles. Left: released blades from spin tests. Right: projectiles tested in gas gun experiments. The scale shown is in centimeter.....	95
Figure 51 comparison of damage. Left: spin testing sp_4. Right: panels after gas gun experiments. Darker regions represent more severe damage.....	96
Figure 52 the out of plane deformation of the panels tested with Method III.	97
Figure 53 instrumented target loadcell callout.....	104
Figure 54 flat panel rig setup where threaded rod allows for adjustment of exposed composite area to blade on front face (shown in figure is back face).....	105
Figure 55 sabot arrestor and positioning of 0.005” thick Mylar sheet to retain vacuum in barrel. This Mylar sheet is shot through.....	105

Figure 56 bolting hardware sequence shown to the left torqued to 11 ft-lbf. Target installation and trigger wire setup (right). The trigger wire starts data acquisition and synchronizes high speed cameras.....	106
Figure 57 LED light source placement for initial projectile velocity measurement.....	106
Figure 58 calibration image (left) and projectile image processing example image (right).....	107
Figure 59 sabot with Ti blade shaped projectile (left) and another sabot with Al cylindrical projectile for instrumented target testing (right).....	107
Figure 60 in-house manufactured poppet valve with Nichrome wire taped with same diameter as ID of barrel	108
Figure 61 trigger wire connection.....	108
Figure 62 assembled inner bearing housing mocked up for temperature monitoring of forward and aft bearing.....	111
Figure 63 lower bearing housing main shaft.....	112
Figure 64 compression tube and forward bearing installation.....	112
Figure 65 aft bearing carrier installation.....	113
Figure 66 forward bearing carrier O-ring installation.....	113
Figure 67 rotating assembly installation into the inner bearing housing. Before pressing in the aft bearing carrier (a) and after seating the aft bearing carrier with woodruff key lined up with slot (b)	114
Figure 68 finished rotating assembly with forward bolt and aft retaining bolt	115
Figure 69 balance hardware laser speed pickup setup left and operating balance rig (right)	116
Figure 70 EasyBalance rotor configuration	117
Figure 71 EasyBalance software results showing acceptable balance for both right and left planes.....	118
Figure 72 drive air control valve offset calibration	119
Figure 73 bearing housing assembly and test article installation on air turbine bulkhead.....	121
Figure 74 oil and airline quick connectors are labeled on the mounting base plate of the air turbine.....	122
Figure 75 vacuum pump accessory.....	123

Figure 76 oil pump accessory	123
Figure 77 addition of peel-ply layer to Aluminum tool plate	126
Figure 78 addition of fabric composite layers	127
Figure 79 addition of permeable peel ply to top surface	127
Figure 80 addition of distribution media layer	128
Figure 81 placement of tacky tape and vacuum bag – direction of flow specified	128
Figure 82 depiction of high temp tacky tape used to seal hose connections	129
Figure 83 tube positioned for infusion.....	129
Figure 84 a method to kink tube when finished with resin.....	130

KEY TO SYMBOLS OR ABBREVIATIONS

A	-	cross sectional area of blade
a	-	blade notch length
a_r	-	chord length
b	-	axial width of blade at root near the hub
cg	-	center of gravity
c_v	-	specific heat at constant volume
E	-	change in total energy
E_a	-	absorbed energy
E_{BL}	-	material parameter of kinetic energy at the ballistic limit
E_e	-	modulus of elasticity
E_r	-	residual energy
F_c	-	centrifugal force
h_r	-	discretized blade height
I	-	mass moment of inertia
I_A	-	area moment of inertia at a specified radial distance
K	-	stress concentration factor
KE_{tot}	-	total kinetic energy
KE_{rot}	-	rotational kinetic energy
KE_{trans}	-	translational kinetic energy
$KE_{\delta r}$	-	incremental kinetic energy
ℓ	-	total blade chord length
ℓ_a	-	distance from root to center of gravity of blade

ℓ_b -	distance center of gravity of blade to tip
M -	moment
m -	mass
m_p -	mass of projectile
$m_{\delta r}$ -	incremental mass
$m_{p\delta r}$ -	proposed discretized mass distribution
n -	polytropic efficiency
P_{case} -	reaction load from fan case to blade tip
p -	pressure
R -	gas constant
R_a -	reaction load at root of fan blade
R_{cg} -	reaction load at blade center of gravity
r -	radial distance from center of rotation
r_h -	radius of hub
r_g -	radial distance
r_t -	radius of blade tip
r_δ -	incremental radial distance
T -	temperature
t -	blade thickness
t_r -	root blade thickness
t_t -	tip blade thickness
U -	change in internal energy
U_{bend} -	bending strain energy
U_{shear} -	shearing strain energy
V -	volume

v - velocity
 v_t - tangential blade velocity
 $v_{\delta r}$ - incremental blade velocity
 $v_{\delta tip}$ - incremental tip velocity
 W - work

α - blade taper angle
 ρ - density of blade material
 σ_c - centrifugal stress
 σ_{UTS} - ultimate tensile stress
 Φ - diameter
 ω - angular velocity

CHAPTER 1 INTRODUCTION

1.1 Problem Definition

In 2002 the New GENx Engine from GE aviation demonstrates a major milestone in aviation history [1]. This new engine holds the world record for most sustained thrust of 127,900 lbs. Introduction of composite fan blades and fan case are major accomplished milestones and are significant for the reported GENx's performance. The use of composite reduced the total weight of the engine by 350lbs. The weight savings directly leads to better fuel economy, increased payload, and greater aircraft range.

One of the largest components in an aero-engine is the fan case. Traditionally, fan cases are made of metallic materials such as titanium and steel alloys which are heavy in comparison to composites. Because of the relatively large size of the fan case structure the opportunity of switching to a lighter weight composite structure has greater influence on overall weight savings compared to smaller engine components.

Typically an engine fan case is used for structural support, ducting air flow, and containment of engine components and debris in the rare occurrence of engine failure. In aircraft engine design, one of the requirements for engine certification is to demonstrate the engine's ability to withstand a fan blade-out (FBO) event per 33.94 FAA regulation [2]. It states, "It must be demonstrated by engine tests that the engine is capable of containing damage without catching fire and without failure of its mounting attachments when operated for at least 15 seconds". This test is necessary to ensure the safety of the aircraft in the event of FBO during a flight mission [3].

During engine operation a FBO event may be caused by fatigue failure of the fan blade which can be triggered from sudden impact from bird strike or other foreign objects. The mature design procedures for metal fan cases allow for industry to proceed with confidence in certifying

engines. However, the same cannot be said for an engine that would use a composite fan case. There is very little information and test data available on key aspects of composite fan case design including ballistic characterization of composite materials, and experimental FBO testing procedures [4].

NASA Glenn Research Center (GRC) has pioneered the research into the development of a design methodology for composite fan cases [5]–[7]. In collaboration with A&P Technology and Williams International, a composite fan case had been developed and tested. The FBO design of this fan case was largely based on ballistic impact testing. Then, post FBO fan case structural strength was investigated with an orbital loading test frame [8]. This composite fan case had successfully passed the engine blade-out test for that particular configuration.

The project at GRC revealed a number of areas requiring further research. Firstly, the laboratory scale ballistic testing is cost effective but it has to be designed carefully to simulate the initial impact due to FBO. A number of parameters in ballistic tests may be optimized, such as (a) the design of the projectile; (b) the orientation of the projectile; and (c) the configuration and orientation of the composite target. In composite fan case testing, these parameters were determined by matching the damage modes of metallic targets with the known results of engine test of metallic fan cases. The design of ballistic testing for FBO of composite fan cases has not been examined systematically. Secondly, the orbital loading test frame investigates the fan cases that had been tested in FBO. The post FBO dynamics immediately after blade releasing was not investigated.

Ideally the FBO event may be investigated in a realistic setting such as in engine blade-out tests and full scale rig tests [4], [9]. However, this method is very costly and may not be the most effective method of investigation for considering new composite fan case designs. It is proposed

that an alternative would be to simulate the FBO in laboratory setting with a specially designed spin pit and separate gas gun testing facility. Commercially available spin pits are typically designed for nondestructive testing and without viewports which requires a custom designed spin pit rig. Some engine manufacturers may conduct FBO tests in-house, but this data is proprietary and unavailable for contributing to improvement of composite fan case design. Conducting a FBO under controlled conditions can closely replicate actual engine testing and will unlock even more simplistic testing procedures. The methods investigated here exist on a scale of complexity and cost between laboratory scale ballistic testing and full scale rig or engine blade-out testing.

The FBO event and the post FBO response in an aero-engine is a complex problem. This dissertation will be focused on the development of an experimental ballistic material characterization method as well as experimental FBO testing methodologies.

The potential damage by FBO happens in two stages. Firstly, an uncontained blade can damage the fuselage and other structures. Secondly, the sudden unbalance upon FBO forces the fan rotor to rotate in an eccentric path such that the tips of the remaining fan blades will come in contact with the fan case and cause further damage to the fan case and the blades. This stage is called rubbing [8]. The vibratory load of the unbalanced rotor may also damage other supporting structures.

1.2 Research Objective

The overall objective of the proposed work is to propose experimental testing methods that will assist in design procedures for composite engine structures. This objective is pursued through a combined experimental and separate computational approach by a team of researchers.

1.3 Approach

As mentioned in 1.1, in order to generate the impact similar in a FBO event using ballistic tests, a number of testing parameters such as the design of the projectile, the orientation of the projectile, and the configuration and orientation of the composite targets, must be carefully investigated. In other published work, these parameters were determined based on the tests on metallic fan cases. In this work, these parameters will be examined by comparing the results of ballistic tests and spin pit FBO tests on composite targets. In addition, a new energy based design concept for the projectile will be investigated. The experimental work will be guided by numerical simulations being conducted in parallel by James Dorer in his PhD dissertation. This dissertation will focus on the experimental aspects of the methodology development.

The following are the major tasks in this thesis:

1. design and assembly of a component spin test set-up
2. manufacture of the composite panels and fan case structures
3. design of ballistic impact experiment
4. ballistic impact experiment of composite panels and fan case structures
5. experimental investigation of FBO using a spin test set-up
6. analysis and correlation of the gas gun and spin pit experimental results

1.4 Scope of Work

As a part of a large project, the focus of this thesis is on the development of gas gun ballistic testing methodology based on experimental spin pit results. The methodology developed will only take into consideration initial impact of a released fan blade to the fan case.

1.5 Executive Summary

This document consists of six chapters. Chapter 1 provides the problem definition, the overall objective, the focus of the thesis work, and a list of specific tasks. Chapter 2 discusses the important concepts on ballistic impacts relevant to this work and background information on composite fan case development. Chapter 3 investigates the use of a small scale fan blade out rig. Speed prediction for a blade release mechanism is investigated as well as data acquisition methods for a spin pit. Chapter 4 discusses about ballistic testing with a gas gun. Gas gun velocity predictions as well as a material characterization method are introduced. Chapter 5 discusses the spin pit testing and correlation to gas gun testing. A new design concept for projectile aimed at stimulating impact due to FBO is introduced. The design of spin pit, the blade release methods, and data acquisition techniques are presented. Chapter 6 presents the research plan and expected contributions from this work. Appendices will cover user manuals for the developed experimental equipment the gas gun and spin pit. Here, the manufacturing process used to manufacture specimens/targets is also explained.

CHAPTER 2 BACKGROUND INFORMATION

2.1 Initial Blade Dynamics

Blade tip speeds seen in aero-engines where a released blade or projectiles could be released into the fan case containment structure can exceed tip velocities of 500m/s. A few examples of the upper limit of blade speed is typically limited by stress for some materials roughly at 450 m/s [10]. However in [11] reports that high quality titanium and aluminum alloys could attain 550 m/s, but 400-450m/s is a realistic speed limitation because of choking prevention. Over speed of a transonic fan stage system tested by [12] attained a tip speed of 537.2 m/s. Reported in [1] the operating composite blade tip speed for the Boeing GENx engine is 369 m/s. The high speed of these blades comes with a very high centrifugal loading tradeoff.

During engine operation, the fan blades are considered to be statically loaded in an equilibrium state relative to the rotating system. The loads on the blades originate from the centrifugal force, bending and torsion of the blade due to air/gas resistance, and imbalance caused by radial offset of the center of gravity.

In normal aero-engine operations, the centrifugal load is the dominant loading mechanism. Figure 1 depicts this load on a blade rotating at angular speed ω . The fan blade is statically loaded in a radially distributed outward direction. This load can be explained from Newton's first law, in that as the blade rotates, a centrifugal load develops to keep blade position and direction changing relative to a reference coordinate system at the center of rotation. The centrifugal load on a blade segment dr at a distance r from its center of rotation is shown in Eq. 1.

1

$$dF_c = \omega^2 r dm$$

with

$$dm = \rho_m A(r) dr$$

Where ρ is the density of the blade material, A is the cross section area.

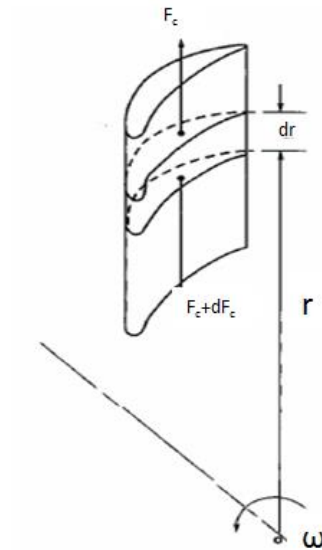


Figure 1 the centrifugal force on a rotating fan blade [10]

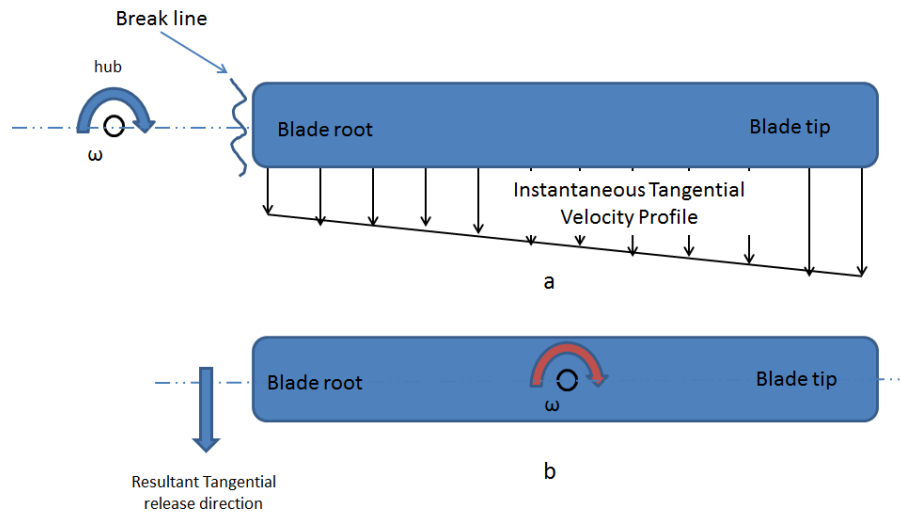


Figure 2 the velocity profile of a rotating blade before (a) and after (b) blade release.

As shown in Figure 1, a rotating blade has a tangential velocity V_t varying linearly along the radial direction

3

$$V_t = r\omega$$

When a rotating blade is suddenly released, the blade will move along a trajectory tangential from its rotation. Due to the varying tangential velocity at different segment of the blade, it will also rotate about its center of gravity with an angular velocity of ω . As a result, the blade tip will impact the fan case with a high tangential velocity at an angle nearly normal to the fan case wall, as shown in Figure 3a as revealed by the finite element simulation of FBO event. Figure 3b shows the tangential velocity and radial velocity V_r of the released blade at different nodal locations at the moment when they come to contact with the fan case wall. In this numerical simulation, the blade tip has a tangential velocity of 530 m/s.

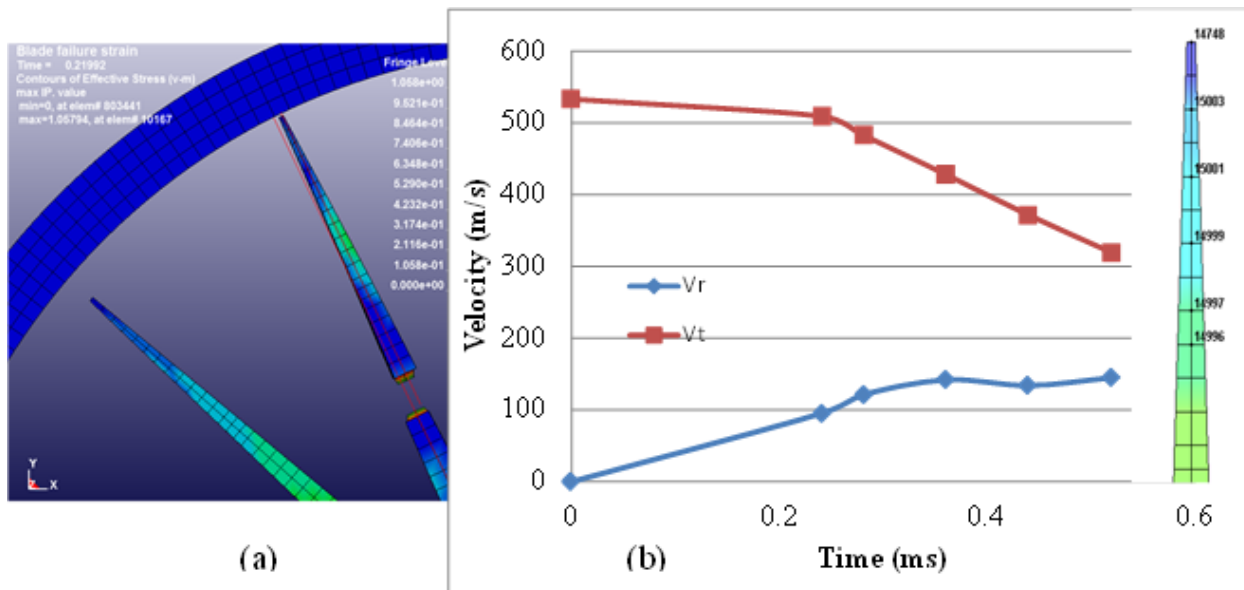


Figure 3 numerical simulation of a blade release event at 40,000 RPM. (a) A release blade at the moment before impacting the fan case. (b) The tangential and radial velocities of the released blade at nodal locations indicated on the blade at the moment when the marked node came in contact with the fan case wall.

2.2 Ballistic Impact

The impact phenomenon is an important topic in engineering mechanics. Within this topic, it is further divided into sub topic areas. A common method to categorize impact problems is by impact velocity [13]–[15]. Figure 4 shows the ranges for low, high and ultra-high velocity impact. The low velocity impact is in the range up to 25m/s, which can be generated in drop weight tests. The high velocity impact ranges from 25m/s to 1300m/s. The impact at above 1300m/s is categorized as the ultra-high. Impact events in space applications are in this range. The impact associated with FBO is within the range of high velocity impact. The high velocity impact is usually generated by ballistic experiments such as gas guns.

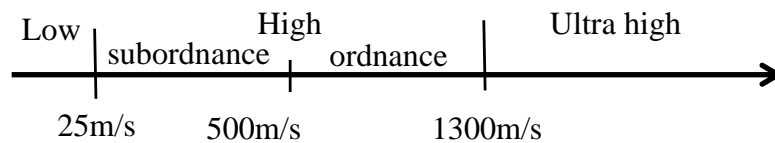


Figure 4 definition of impact velocity range.

Besides the impact velocity, the other important parameters are: the angle of incidence of the impact, the configuration and material characteristics of the target, and the configuration and material characteristics of the penetrator.

Figure 5 provides the definition of impact angle α , which is the angle between the trajectory of the projectile and the normal of the target. $\alpha=90$ degree is defined as the normal impact which occurs when the trajectory of the projectile is perpendicular to the target. Impact with α other than 90 degree is called oblique impact.

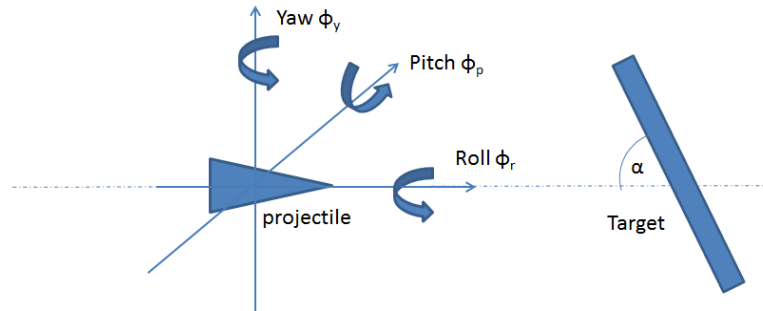


Figure 5 projectile with yaw, pitch and roll motion is moving from the left to right. The target obliquity is α .

Classification of targets can be of semi-infinite, thick, intermediate, and thin. Each classification is a function of how the boundary influences the travel of the projectile. Within each case a semi-infinite target is considered to have no influence of the boundary, thick targets will influence the travel of the projectile only after considerable travel through, intermediate targets the rear surface influences the deformation process, and thin targets do not have any deformation gradients throughout their thickness.

The structure response of the fan case during FBO impact is the results of dynamic interaction between the blade and fan case. The released blade commonly exhibits large deformation. Some even rupture into segments or fragments [3]. To successfully simulate FBO in ballistic testing, the deformation mode of the projectile is one of the factors to be investigated.

2.3 Impact Response of Composite Structures

To understand how to manufacture a fan case that will contain a failed rotor blade, the dynamics response and failure mechanisms of the fan case material should be carefully characterized. For structural response, it should be determined if the impact will be of high or low velocity as most materials exhibit different failure modes and responses from low to high strain rates [16]. Low velocity impacts allow the entire component or structure to respond to the time dependent load and therefore global deformation can take place. The high velocity impacts are characterized by

local damage as it occurs before the stress waves can propagate throughout the component to reach its boundary. As a result the boundary conditions of the component may be neglected in high velocity impact [17].

For composites, a quantified threshold of where the high to low velocity impact takes place was determined in [18]. For composites with a failure strain of approximately 0.5 to 1.0%, the transition stress to high velocity is at $10\text{-}20\text{ms}^{-1}$. In FBO events, the blade tip speeds typically are at hundreds of meters per second. As a result composite a fan case under FBO impact can be characterized as high velocity impact events.

Failure mechanisms in composite materials have long been investigated by a myriad of researchers. Composite laminates have four key distinct modes of failure defined as: matrix mode, delamination mode, fiber mode, and penetration. Each damage mode can be seen in both high and low velocity impacts; however certain modes will dominate depending on loading orientation and impact velocity [19][20].

For resistance to impact, the ability to store elastic energy is paramount [21]. For example, carbon fiber has the highest strength and stiffness values with strain to failure at 0.5 to 2.4%, also making it the most brittle. Glass has a strain to failure of approximately 3.2% [22]. Kevlar has a strain to failure value between the carbon and glass fibers [23]. In other words, E-glass fibers can absorb much more energy caused by impact than the carbon fibers. Traditional thinking of strongest structurally performing materials may not translate to the best used material for resistance to impact. This could even open the possibility of combining glass and Carbon composites in a hybrid composite design that may lead to a better performing impact resistant structure.

The work on reinforced carbon composite reported in [24] show that there exists an optimum thickness where energy to incident damage initiation for high velocity impact is maximized. This shows that there is a possibility to optimally reduce a structures weight to accommodate high velocity damage. However, specimen thickness is crucial in determining perforation impact energy where the thicker the specimen the greater amount of impact energy is needed for perforation to occur. Balance between damage initiation energy and perforation energy could be beneficial for making lightweight large composite structures. The study had also shown that the specimen geometry and size is dependent upon loading rates. For low velocity testing of the specimen, a reduction in total delamination area and an increase in damage initiation thresholds vary almost linearly with increasing specimen length. However, the high velocity impact had shown nearly no dependence upon specimen length as most of the damage occurs locally and is not dependent upon the specimen size. An analytical model produced by [25] can accurately predict the perforation velocity of composites and may be able to extend to hybrid composites of different material layers. The model considers three main energy absorbing parameters to determine the perforation velocity: energy absorbed in tensile failure of primary yarns, elastic deformation of secondary yarns, and energy absorbed due to kinetic energy of a moving damage cone. Other researchers [26], [27] use a similar approach in accounting for absorbed energy, including energy absorbed due to matrix cracking, shear plugging, and friction in woven fabrics.

2.4 Ballistic Limit

The ballistic limit is defined as the velocity in which a projectile is at the threshold of perforating the target. Commonly known as the V_{50} limit, a statistical approach is utilized where at the critical velocity of V_{50} there exist a 50% probability that the projectile will perforate the barrier. It can be determined by averaging six velocities where three are of lowest velocity in which complete penetration occurred and three are of highest velocity in which full penetration occurred. [15]

CHAPTER 3 FAN-BLADE-OUT EXPERIMENT AT SMALL SCALE

3.1 Introduction

In aircraft engine design, one of the requirements is to demonstrate the ability of the engine to withstand a fan blade-out (FBO) event [28], [29]. A FBO event may be caused by fatigue failure of the fan blade itself or by impact damage of foreign objects such as bird strike. The potential damage by FBO happens in two stages. Firstly, the released blade will impact the fan case. A contained blade may interact with the remaining blades and result in further damage. An uncontained blade may damage the fuselage and other structures. Secondly, the sudden unbalance upon FBO will force the fan rotor to rotate in an eccentric path such that the tips of the remaining blades may come in contact with the fan case and cause further damage to the fan case and the blades. The dynamic load of an unbalanced rotor may also damage the bearings and rotor [9], [29], [30].

The analysis and design procedure for turbines and structures is a sensitive topic for aircraft engine producers [31]. Besides the certification required full scale engine FBO test, the information on FBO is rather scarce in open literature. The reported studies include the investigation of FBO events using spin testing [32]–[35], ballistic impact simulated experiments [5], [8], [26], analysis [36], and numerical simulations [5], [28], [29], [35], [37], [38].

The design of a containment structure is related to numerous parameters such as the blade tip speed; blade material, size and shape; hub/tip diameter; fan case material, configuration, rigidity, the strain rate sensitivity of the material, etc. To investigate all parameters by spin experiments with a full size rotor assembly would be prohibitively expensive. Ballistic impact experiment is less costly but the data generated is useful only for the first stage of FBO. Furthermore, the result may not be representative if the experiments are not properly conducted. For example, in spin tests with two blades [34], it was observed that the released blade tend to make multiple impacts

on a hard wall fan case and the damage measured by the depth of penetration into the fan case wall caused by the second impact was greater than the initial impact. Numerical simulations [37] suggested that, when a full set of blades is present, the force resulted from blade to blade interaction would be considerably higher than if the blade is not in contact with other blades. Therefore, to produce similar results as in spin testing, the ballistic impact experiments must be carefully designed for each specific system [39]. Measures such as firing a projectile at an angle to the fan case [5], [8], [26] and using a specially designed projectile instead of an actual blade segment [8] have been investigated.

Limited by the experimental capability, the current understanding on FBO events is incomplete. The data on blades and fan cases made of materials other than metallic systems is even rare. Furthermore, to extract more meaningful data from a test, new data acquisition techniques need to be explored. A low cost experimental apparatus for FBO will greatly facilitate these developments.

This paper presents a small scale spin rig for FBO experimentation. This set-up allows one to develop the experimental techniques for an FBO experiment and to investigate the dynamic characteristics of a high speed rotating system before a large size spin rig is built.

3.2 Experimental Setup

3.2.1 Spin Rig

A schematic of the small spin rig is shown in Figure 6. The rig is housed in a cylindrical vacuum chamber of $\Phi 203 \times 203$ mm. The top and the side wall of the chamber were made of steel with a thickness of 6.4 mm. For imaging, the bottom of the chamber was constructed with a clear,

impact resistant polycarbonate plate of 19 mm thickness, i.e. the bottom is a viewport of $\Phi 203\text{mm}$.

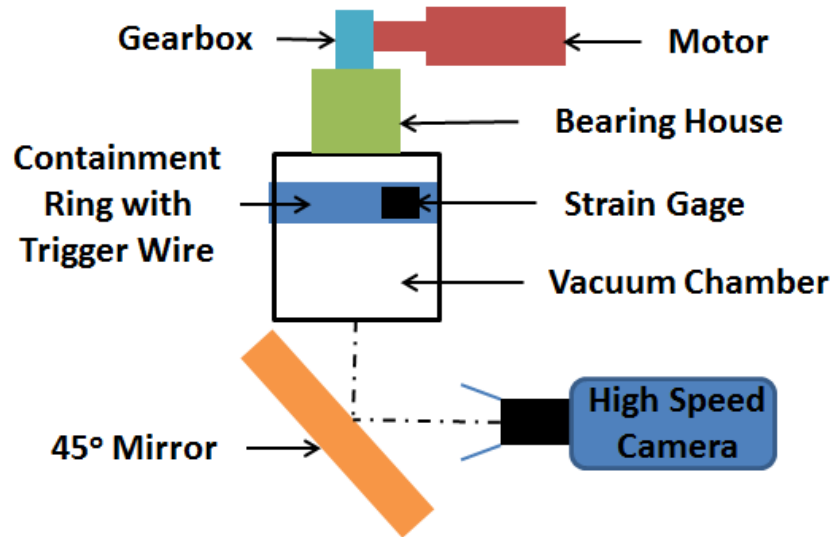


Figure 6 schematic of the small spin pit rig.

The high speed spin is generated by an electrical motor rated at 3HP, 20,000 RPM. Through a gear box of 31/13 ratio, the maximum nominal rotating speed of the current rig is 47000 RPM.

The gearbox shaft is fed through a bearing house to a flexible shaft coupling which protects the gearbox and motor from harmful vibration caused from the unbalance load after an FBO event.

Figure 7a show the completed spin rig. The total investment in small spin pit rig is \$3k.

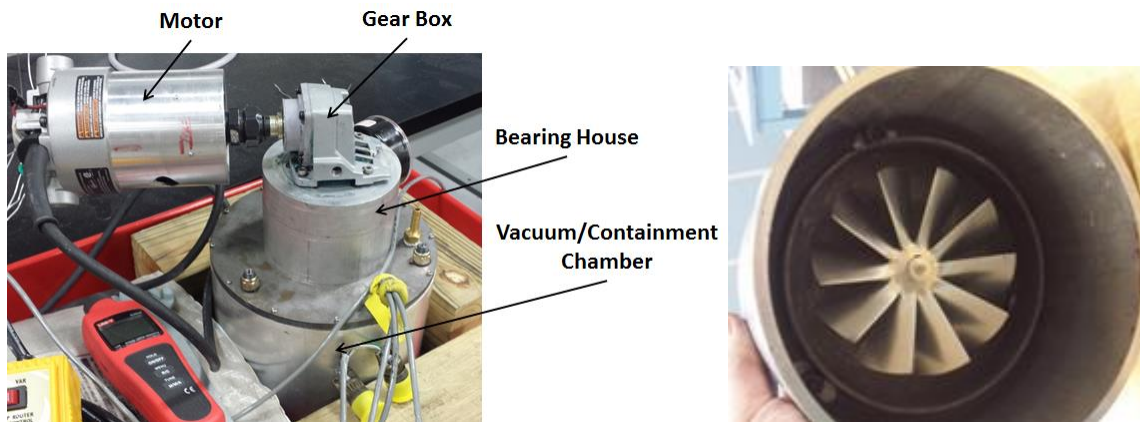


Figure 7 (a) Assembled small spin rig: the setup of motor, gearbox and the vacuum chamber. (b) An aluminum cooling fan is held in with a steel shaft inside a steel fan case. The assembly is installed inside the vacuum chamber.

3.2.1.1 Notched Blade Release Mechanism

In FBO experimentation, one of the blades needs to be released in a controlled manner. The reported blade release methods for FBO experiments include mechanical release system, magnetic blade excitation, pyrotechnic release [40], and notched blade [34], [40]. Pyrotechnic release is the most precise method but it was not permitted at the current lab. The notched blade method was selected because it is relatively reliable and simple to implement. The notch was introduced near the root of the blade with a die grinder.

In rotating components, the centrifugal force results in tensile stress along the radial direction, as illustrated in Figure 8. The notched blade would be released by material rupture when the stress at the notched section reaches its ultimate strength.

For a blade with a cross section area A , a tip radial distances to the rotation axis r_t , a hub radial distances of r_h , the centrifugal force F_c at the root of the blade is given by Eq. 4

4

$$F_c = \omega^2 \rho \int_{r_h}^{r_t} r A(r) dr$$

where r is the radial distance, ρ is the density of the blade material, and ω is the angular velocity.

The blades of the cooling fan used in this study are tapered. For a blade with a width varying linearly with radial distance as shown in Figure 8, the cross section area is given by Eq. 5.

5

$$A(r) = t(b + 2r \tan(\alpha))$$

Where t is the thickness and b is the root axial width of the blade, respectively, and α is the taper angle. The centrifugal force F_c at the root of the blade is given by Eq. 6

$$F_c = \omega^2 \rho t \left\{ \left[\frac{br_t^2}{2} + \frac{2r_t^3}{3} \tan(\alpha) \right] - \left[\frac{br_h^2}{2} + \frac{2r_h^3}{3} \tan(\alpha) \right] \right\}$$

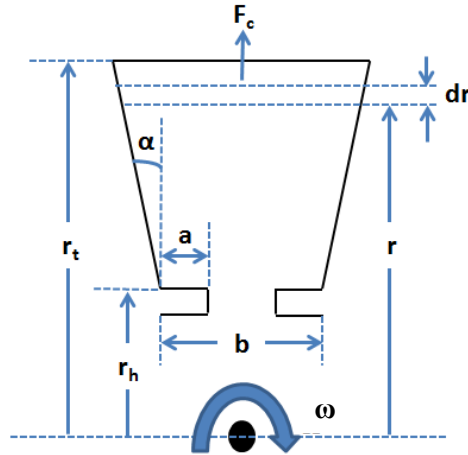


Figure 8 schematic shows that sections of blade dr at radius distance r , under an angular speed of ω resulting in a centrifugal force F_c on the section.

The centrifugal stress σ_c on a notched section with remaining width of $b-2a$ shown in Eq. 7

7

$$\sigma_c = \frac{F_c}{A} = \frac{\omega^2 \rho t}{(b-2a)t} \left\{ \left[\frac{br_t^2}{2} + \frac{2r_t^3}{3} \tan(\alpha) \right] - \left[\frac{br_h^2}{2} + \frac{2r_h^3}{3} \tan(\alpha) \right] \right\}$$

When operating in vacuum, the gas drag on the blade can be neglected. The centrifugal stress is assumed to be the dominant stress component on the blade. As the rotation speed increases, the blade will be stressed until the notched section reaches the ultimate strength of the blade material σ_{UTS} . For structures containing discontinuities such as holes and notches, the stresses at the vicinity of these features are higher [41]. A stress concentration factor should be considered at these locations. Therefore, a stress concentration factor is introduced. The blade release speed is related to the square root of the remaining width $b-2a$ as seen in Eq. 8

$$\omega = \sqrt{\frac{\sigma_{UTS}}{K} \frac{b - 2a}{\rho \left\{ \left[\frac{br_t^2}{2} + \frac{2r_t^3}{3} \tan(\alpha) \right] - \left[\frac{br_h^2}{2} + \frac{2r_h^3}{3} \tan(\alpha) \right] \right\}}} \propto \sqrt{b - 2a}$$

where K is the notch stress concentration factor. Eq. 8 reduces to the relationship reported in [34] when $K=1.0$ and $\alpha=0$.

3.2.1.2 Testing Articles

Low cost aluminum cooling fans of 127 mm (5 in) diameter, as shown in Figure 7b, were used in the FBO experiment. The cooling fan was made from a single aluminum sheet of 0.76 mm thickness. The sheet was cut radially towards its center into ten slices. The blades were formed by twisted slices. The uncut region at the center serves as the hub for the fan. The fans were made of 6061-T4 Aluminum. The material and geometric parameters of the fan is provided in Table 1.

Table 1 material and geometric parameters of Aluminum fan blade

σ_{UTS}	$\rho(\text{kg/m}^3)$	$r_t(\text{mm})$	$r_h(\text{mm})$
207.0	2700.0	63.5	14.0

To create variations, some fans were modified by reducing the blade width. Modification 1 (M-1) reduced the taper of the blade from $\alpha=18^\circ$ to $\alpha=10^\circ$. Modification 2 (M-2) reduced the blade width at its base and keep it as a constant from its base to its tip, i.e. $\alpha=0^\circ$. Table 2 shows the parameters of the fan blade as received and two modifications.

Table 2 geometrical parameters for blades as received and after modification M1 and M2

Blade	b(mm)	α
as received	9.7	18.0
M-1	9.7	10.0
M-2	3.2	0.0

The fan was held in place using a 6.4 mm diameter steel shaft. A steel fan case with a wall thickness of 3.2 mm was used for containment. The inside of the case was painted white before each test to make it easier to locate damage areas. Figure 7b show the fan/steel fan case assembly installation inside the small spin rig.

3.2.1.3 Data Acquisition

The small scale spin rig was used to investigate the blade release mechanism, triggering, high speed video imaging, and data acquisition. A high speed Phantom v7 camera was employed. Dynamic signals were collected with a strain gage positioned centrally on the outer wall of the containment fan case. The gage was oriented along the hoop direction on the steel containment ring. Data was collected using NI Signal Express software paired with an NI 9184 module.

For notched blade release, the exact instant of blade release is not known. To capture the FBO event and to record data at high sampling frequency, a trigger is needed. In this experiment, a simple trigger wire method has been developed to trigger the data acquisition and high speed camera recording. By wrapping a thin wire around the wall of the fan case, a conductive path in the form of parallel lines was formed at the inner surface of the fan case, as shown in Figure 9. The released blade will cut the conductive path when it impacts the fan case. This triggers the data acquisition for the camera and NI Signal Express software. Since both devices allow a pre-start time to record data before the trigger, pre-FBO data can be included. The pre-start time was set at 2ms for all experiments.

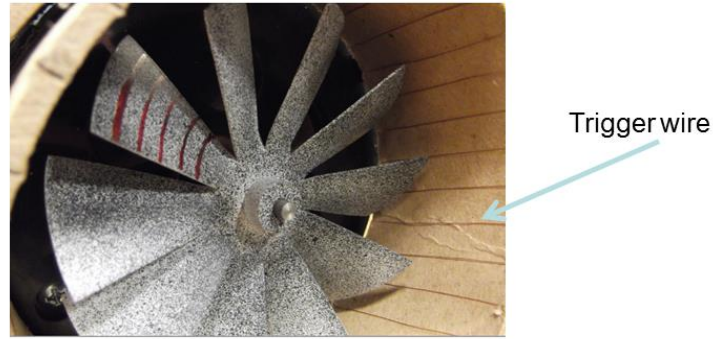


Figure 9 trigger wire mechanism and fan blade system.

Table 3 provides a summary of six FBO experiments. The rotational speed at blade release, the corresponding tip speed, and the observed failure types are reported.

Table 3 experiments conducted with cooling fan

Test	Failure speed(RPM)	Tip speed(m/s)	2a(mm)	Result*
1	16135	107.3	4.6	a
2	17021	113.2	0.5	b
3	17026	113.2	1.0	c
4	31796	211.4	0.6	b
5	34324	228.2	0.6	b
6	35260	234.5	0.6	b

*Result: (a) FBO only, (b) FBO with hub failure, (c) FBO and blade interaction

3.2.2 Blade Release Prediction

The notched blade release speed was predicted using Eq.5 with material and geometrical parameters listed in Table 1 and 2 for all three aspect ratios. Figure 10 compares the predictions with the experimentally measured values in terms of the release speed versus the relative remaining length at the notched cross section, where the lines are the predictions and the symbols are the experimental results. Although slightly scattered, the experimental data in general followed the predicted curves. M-1 results in a relatively small change in the centrifugal force.

The experimental result of M-1 was indistinguishable from that of as received. The results of M-2 clearly fell into a different cluster.

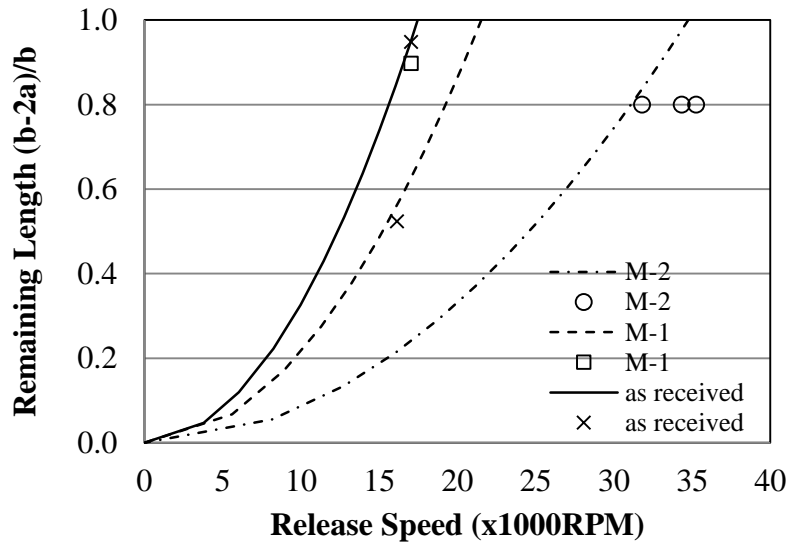


Figure 10 comparison of the predicted release speed (lines) and experimental results (symbols) for cooling fan blades with and without modification.

3.2.3 FBO Response

Figures 11-13 present the typical strain traces measured on the hoop direction of the fan cases. The high speed video images corresponding to each strain trace are also shown. This synchronized data acquisition allows for the cause of a specific strain response to be identified. The three figures here represent three different cases: FBO only, FBO followed by hub failure, and FBO followed by trailing blade interaction.

Figure 11 presents test 1, an FBO only result. The notched blade was released and impacted the fan case at time 1.000ms. The first peak of the strain trace registered this event. After this, the blade debris rode on its tip along the fan case and bounced on the case. The small strain spikes following the first peak corresponded to bouncing. At 1.9249ms, approximately 900 μ s after the initial impact, the blade tip plastically deformed and curled over leading to a second impact on

the case. This resulted in a compressive strain peak with amplitude slightly lower than that caused by the initial impact. Since there was only one strain gage, depending on the location of the impact relative to the location of the strain gage, the strain reading can be positive or negative. After that, the blade turned to face the fan case and scraped along the fan case at low speeds and the strain varied at relatively low amplitudes.

Figure 12 presents a case of FBO followed by failure at the hub region. At 0.200ms, a single blade release can be clearly visualized. The blade tip remained in contact with the fan case wall developing a bouncing strain signal similar to test 1. At 2.800ms a complete hub failure occurred which resulted in much higher strain peaks. It should be noted that hub failure as a result of FBO, although being observed in this study, is not a common phenomenon. So far, it has not been reported for a real aircraft engine test. As described previously, the cooling fan used here was made out of a single sheet of aluminum. Its hub region was not designed to withstand an FBO event. On the other hand, the spin rig must be designed to withstand the impact of hub failure.

Figure 13 show the cases of blade to blade interaction. As seen, the released blade remained in the path of the trailing blade. The trailing blade struck the released blade at the full speed which imparted an additional energy to the released blade. This resulted in a higher impact force when the released blade makes the second impacts. The recorded strain was greater both in magnitude and in duration.

Two factors may have contributed to the increased strain at the second impact. The first is the orientation of the blade during impact. In the initial impact, the blade contacted the fan case with its tip. The impact force caused the blade to bend and the blade tip may have experienced some plastic deformation. This would reduce the amount of energy to be transferred to the fan case.

For the second impact in Figure 13, the blade was oriented such that its front surface was in contact with the fan case. Very little plastic deformation occurred during this impact, resulting in a greater amount of energy transferred to the fan case. The second factor was that the blade may be at a higher velocity at the second impact. The blade overall translational velocity at release depends upon the blade geometry and mass distribution and is less than the blade tip speed. Before making the second impact to the fan case, the released blade had been accelerated through the interaction with the trailing blade and hence had gained additional kinetic energy. A greater impact force resulting in more severe damage by the second impact has been observed in FBO experiment [34], [39]. In Figure 13, the third strain peak is even higher than the second one. This is also attributed to blade to blade interaction.

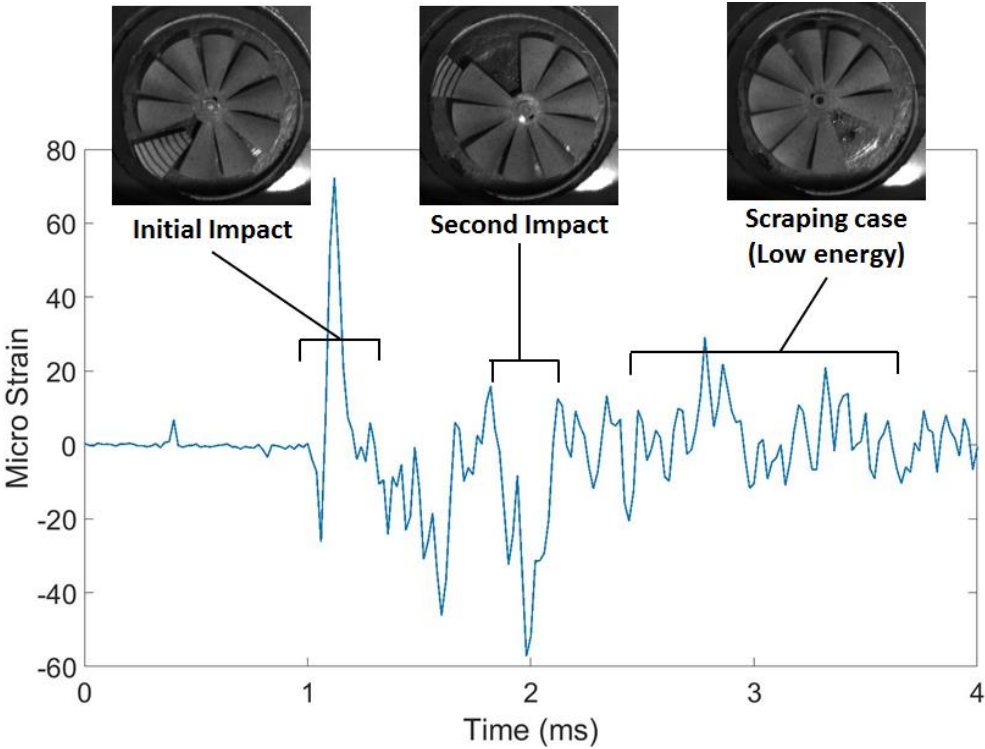


Figure 11 the hoop strain on the fan case in fan blade release (FBO) experiment with a cooling fan. The blade was released at 16,135 RPM. There was no interaction between the release blade and other blades.

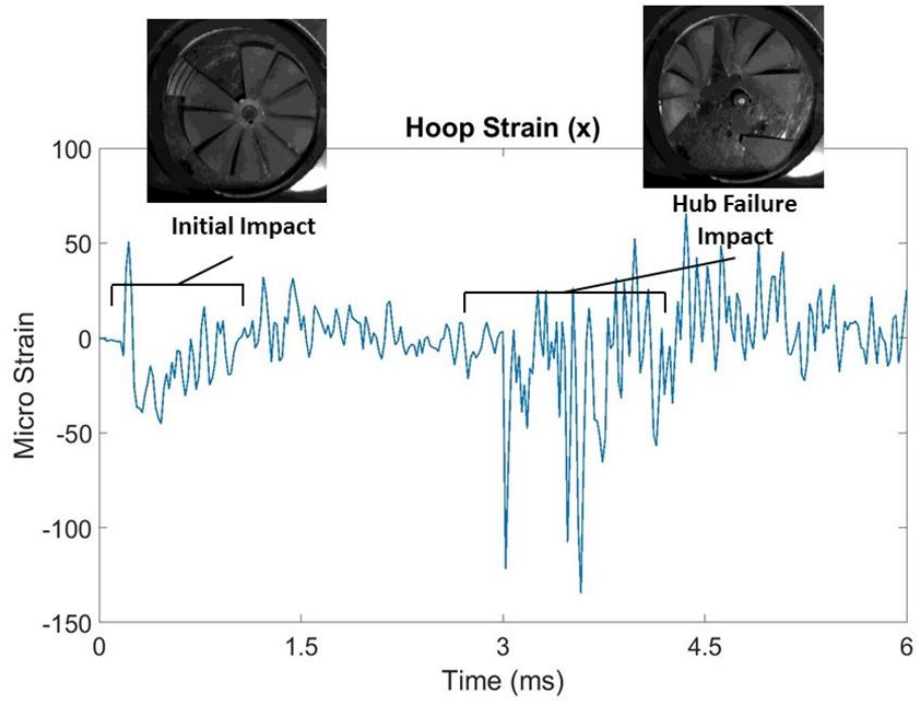


Figure 12 the hoop strain on the fan case in FBO experiment with a cooling fan. The blade was released at 17,021 RPM. The FBO was followed by hub failure.

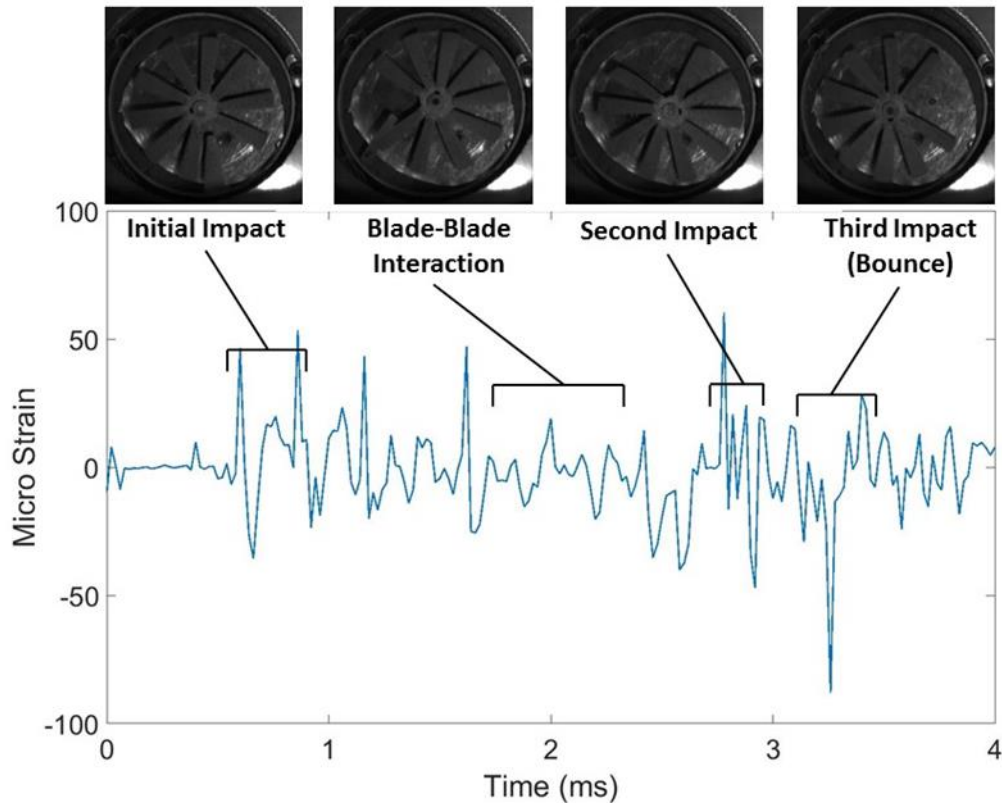


Figure 13 the hoop strain on the fan case in FBO experiment with a modified cooling fan. The blade was released at 17,026 RPM. The blade to blade interaction was observed.

In summary, using the small spin rig, the following phenomena were observed. The released blade made multiple impacts on the fan case. The impact force in the subsequent impacts may be greater than that of the initial impact, particularly when blade to blade interaction and/or hub failure occur.

3.3 Conclusions

A low cost, small scale spin rig has been developed. The rig has been used in fan-blade-out (FBO) investigations and experimental technique development. The notched blade release mechanism was investigated. The relationship between the release speed and notch depth was modified with the consideration of the notch concentration factor K . The predicted release speeds

with $K=3.0$ agreed reasonably well with the experimental results. A simple trigger wire method was developed which synchronizes the data acquisition of sensors with a high speed camera.

Using the small rig, three different FBO events have been observed: FBO only, FBO followed by hub failure, and FBO followed by trailing blade interaction. The strains measured on the fan case in the subsequent impacts can be higher than that of initial impact, particularly when the blade to blade interaction occurs. The blade/fan case contact and blade/blade interaction phenomena observed in small scale testing are similar to those reported in literature using much larger scale spin rigs.

The small rig has the potential in a variety of applications from investigating FBO events, verifying concept designs of rotors, to developing methods and experimental techniques for high speed spin testing.

3.4 Summary

This paper describes a low cost, small scale spin rig. The rig is housed in a steel vacuum chamber of $\Phi 203$ mm (8 in) diameter and powered by a 3HP variable speed DC electric motor. The small rig was developed to test the experimental procedure and data acquisition techniques and to investigate the dynamic characteristics of a high speed rotating system. Using this rig, fan-blade-out (FBO) experiments were carried out. The notched blade releasing mechanism was investigated. The relationship between the notch depth and the release speed was modified with the consideration of the notch concentration factor. The predicted release speed agreed reasonably well with the experimental data. A simple wire trigger method for data acquisition was developed. Synchronized high speed video images and sensor signals during FBO events were obtained. The observed phenomena were similar to those reported using larger spin rigs.

CHAPTER 4 INVESTIGATION OF HIGH VELOCITY IMPACT RESPONSES OF
COMPOSITE PANELS WITH A GAS GUN

4.1 Introduction

Impact with an initial velocity between 250m/s to 1300m/s is classified as high velocity impact [13]. Understanding the material behavior and structure response at this range is important to improve designs against impacts generated by ballistic events, debris from explosion, bird strikes, and failure of high speed rotating machine components [42], [43].

In laboratories, high velocity impact is often generated using gas guns [13], [44]–[46]. The gas gun testing methodology is still under development. There is no established method to predict the required pressure for a targeted velocity. The experiments rely on experience and trial and error. The common outputs of such experiments are the level of damage to the material versus the impact velocity. With advanced 3D displacement measurement techniques, such as 3D digital image correlation (DIC) [47]–[49], moiré and fringe projection [50], the deformation field of the structure under impact can be recorded. The impact pulse measurement has been attempted with strain bars and an instrumented target [51], as well as an instrumented projectile [52]. The quantitative data will be useful in the validation of computational models for the prediction of high velocity impact response of structures.

The objective of this work is to obtain data to assist the development of computational models for the prediction of high velocity impact of composite structures. This includes qualitative observations of the damage and failure modes of the composites, and quantitative measurements of force and displacement at locations which can be verified in computational models.

This paper presents some recent developments in gas gun experimental methodology towards this goal. A method to estimate the required pressures for a targeted velocity using a single stage gas gun was proposed. A projection grating profilometry method was employed to measure the

out-of-plane deformation. Resistance strain gage based load cells were used to measure the force transmitted to the testing frame. A S2-glass plain weave/SC-15 epoxy composite was investigated. Its post-mortem damage and failure modes were evaluated with images obtained with backlighting.

4.2 Experimental Setup

4.2.1 Gas Gun

Figure 14 shows the schematic of the single stage gas gun used in this work. The major components are a gun barrel, a pressure vessel, and a poppet valve. The steel barrel is 4.7m long with an inner diameter of 108mm. The steel pressure vessel has a volume of 0.030m³. Compressed Helium is used in this work. The poppet valve is made of a Mylar diaphragm, which consists of two layers of Mylar sheets of a total thickness 0.50 mm with embedded Nichrome wires, as shown in Figure 15. Another thin Mylar sheet of 0.25 mm is installed at the exit end of the gun barrel which allows the barrel to be vacuumed to 1-5 kPa. The vacuum prevents the formation of a shock wave in front of the projectile, allowing it to travel at a higher velocity [53], as well as reduces air/gas in front of the sabot that must be pushed out of the barrel, resulting in efficiency loss. The pressure is released by rupturing the Mylar diaphragm by resistance heating of the Nichrome wire at the instant of closing the electrical circuit.

In a gas gun experiment, a sabot carrying the projectile is placed in the barrel next to the poppet valve. At the instance of pressure release, the high pressure in the barrel accelerates the sabot down the barrel to reach a high velocity. A sabot arrester at the end of the barrel destructively stops the sabot and allows the projectile to pass to impact the target. The projectile used in this work was a solid aluminum cylinder of 38.1mm diameter and 18.5mm tall, with a mass of 60g.

The sabot design is critical to attain the targeted velocity and to ensure the orientation of the projectile. The sabot should be as light as possible, produce a minimal chatter in the barrel, and maintain its structure integrity during the high speed travel. A sabot with a diameter and length nearly equivalent to the barrel diameter was found to be a good starting point for design. In this work, the sabot was made with polylactic acid (PLA) material through 3D printing on a Solidoodle workbench with 0.30 mm resolution.

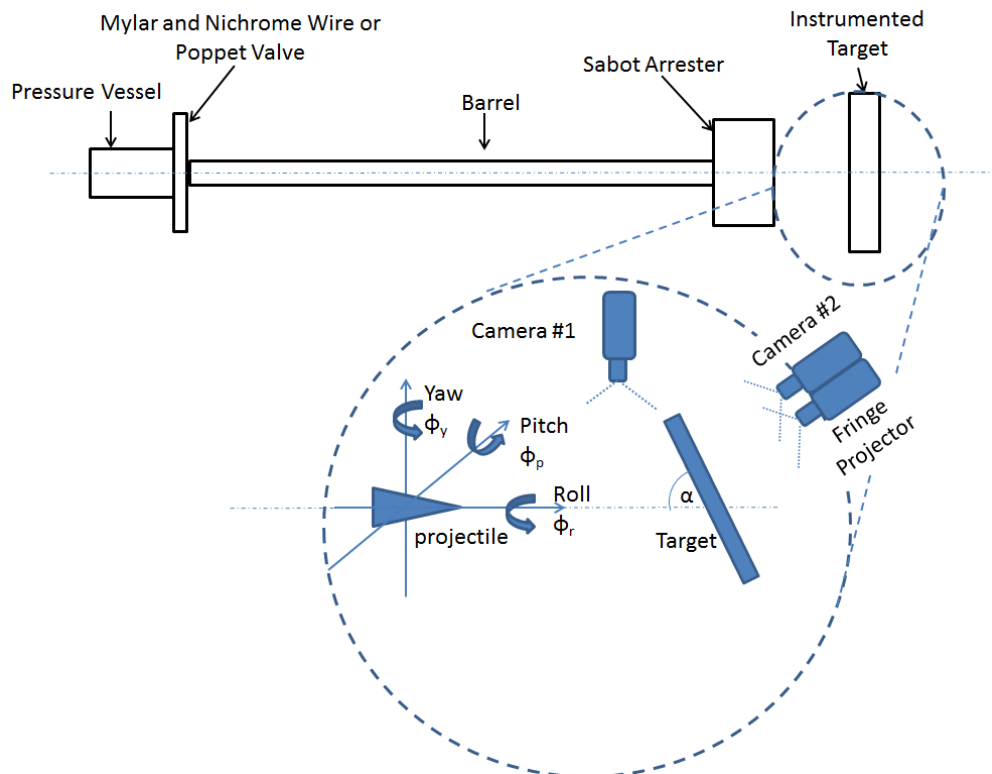


Figure 14 the schematic of a single stage gas gun. Camera #1 phantom V12 for determining the projectile initial velocity and orientation. Camera #2 phantom V7 for determining the projectile residual velocity and the out-of-plane deformation using a projection grating profilometry method.

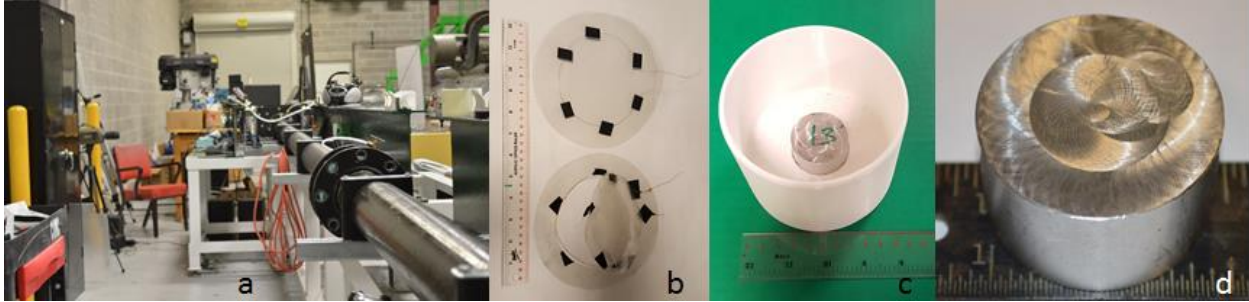


Figure 15 (a) the gas gun used in experiment. The gun barrel length is 4.7m (15.5 ft) long with an inner diameter of 108mm (4.25 in). (b) The poppet valve is made of Mylar with embedded Nichrome wire and a spent valve shown bottom. (c) The sabot is made of polylactic acid (PLA) and features a recess to hold projectile in position by press fit. (d) An aluminum 60g projectile machined to a flat on both ends.

4.2.3 Projectile Velocity Measurement

The projectile velocity at the instance of impact is referred to as the initial velocity. After interacting with and penetrating the testing panel, it is referred to as the residual velocity. A rebounding projectile will have a negative velocity.

As shown in Figure 14, two high speed video cameras were used in the experiment. Camera #1, a Phantom V12.1, was used to determine the velocity and orientation of the projectile before impact and the residual velocity of a rebounding projectile. Camera #2, a Phantom V7 was used to determine the residual velocity of the projectile that had perforated the target [54].

The velocity of the projectile at the instant of impact is determined from the high speed video footage using the PCC 2.7 software from Vision Research, as shown in Figure 16. An image of a scale ruler positioned in the flight path of the projectile is taken before the test. With this image, a calibration constant of distance per pixel can be determined from the software and used to calculate projectile velocity. Camera parameters for this test setup are shown in

Table 4.

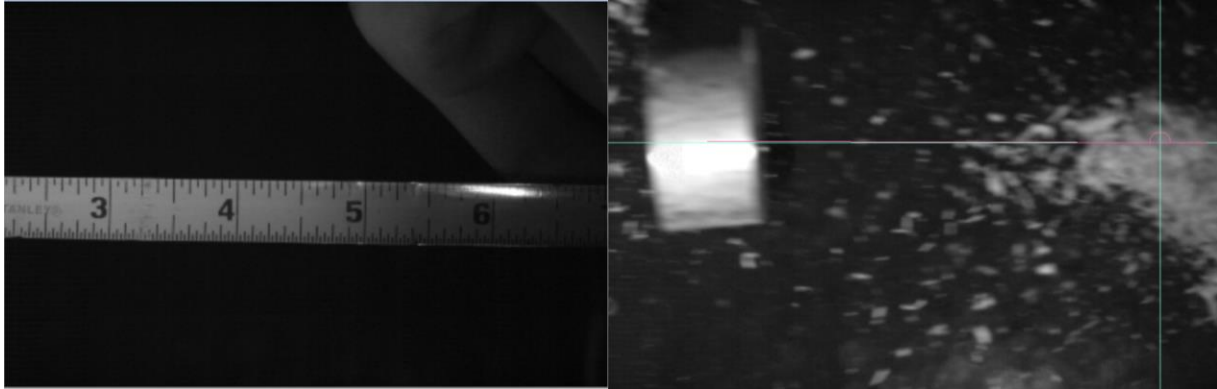


Figure 16 determining projectile velocity using high speed video footage. Shown left is a calibration image taken before testing with scale in direct flight path of projectile. Shown right is the projectile moving right to left towards target.

Table 4 camera specifications

	Camera #1	Camera #2
Make/Model	Phantom/V12	Phantom/V7
Lense	Tamaron (14mm)	Samyang (90mm)
Frame Rate (images/s)	41k	32.5k
Resoulution	400x256	224x224
Calibration Constant ($\mu\text{m}/\text{pixel}$)	287	1875

4.2.4 Gas Pressure and Impact Velocity

The impact velocity of a gas gun experiment is determined by the gas pressure in the pressure vessel, the total mass of the sabot and projectile, and the specific gas gun set-up. A common analysis is based on the equation of motion and thermodynamics. In [55], approximate solutions were provided for both single-stage and two-stage gas gun.

In this work, only single-stage gas gun is considered. In this case, a relationship between the gas pressure in the vessel and the targeted velocity can be derived directly based on an adiabatic thermodynamic analysis by considering only the initial and the end state of the system.

According to the first law of thermodynamics, the change in energy for an adiabatic system is

9

$$\Delta E = -W$$

where W is the work and ΔE includes the kinetic energy and the internal energy such that

10

$$\Delta E_i + \Delta U = -W$$

During a gas gun experiment, the change in the kinetic energy of the system is that of the sabot and the projectile

11

$$\Delta E_i = \frac{1}{2} m_p (v_2^2 - v_1^2)$$

where m_p is the total mass of the sabot and the projectile, v is the velocity of the projectile, the subscript 1 denotes before triggering of the gun, 2 denotes the instance before the projectile fully exits the barrel. Since the sabot is at rest before triggering of the gun, $v_1=0$. The kinetic energy of the gas is neglected because of its low mass.

The work for the process is done by the released gas. It is similar to that of a compressor upon discharge. With an ideal gas assumption for a polytropic process, the work is

12

$$W = \int_1^2 p dV = m_{gas} R \frac{T_2 - T_1}{1 - n}$$

Where m_{gas} is the total mass of the gas in the pressure vessel, T_1 is the ambient temperature in Kelvin, n is the polytropic efficiency, and R is a gas constant. The change in the internal energy is that of the gas

13

$$\Delta U = m_{gas}c_v(T_2 - T_1)$$

where c_v is the specific heat at constant volume [56]. In a polytropic process

14

$$T_2 = T_1 \left(\frac{p_2}{p_1} \right)^{(n-1)/n} = T_1 \left(\frac{V_1}{V_2} \right)^{n-1}$$

Where p_1 is the initial pressure, p_2 is pressure just before the projectile exits the barrel, V_1 is the inner volume of pressure vessel, V_2 is the total inner volume of the pressure vessel and barrel.

The ideal gas equation of the state is

15

$$m_{gas} = \frac{p_1 V_1}{RT_1}$$

In this process, m_{gas} is constant. Substitute m_{gas} and T_2 in Equation 12 and Equation 13 with Equations 14 and 15, and introduce Equations 11, 12, and 13 into Equation 10. A single expression relating v_2 with p_1 is derived, where p_1 is the absolute pressure. To find the gage pressure needed after vacuuming the gun barrel, subtract the vacuum pressure from p_1 . A flowchart is presented in Figure 17 that illustrates this process.

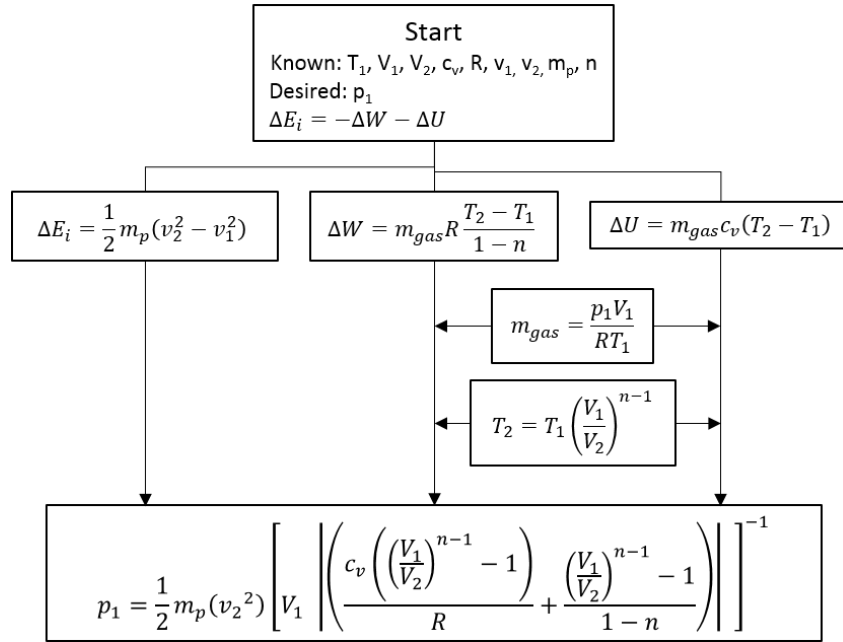


Figure 17 flowchart describing the solution process to get vessel pressure. The final equation can be solved for the absolute pressure, p_1 . To find the gage pressure needed after vacuuming the gun barrel, subtract the vacuum pressure from p_1 .

The polytropic efficiency for the gas gun set-up in this work was found to be $n=1.26$ for velocities in the range of 330m/s to 467m/s. This value was determined by curve fitting of the data generated in the calibration runs. The established relationship was used in later experiments. Table 5 provides the values of the parameters in the equation at the bottom of Figure 17 for the current gas gun system and the gas constant for Helium [57].

Helium was selected over other gases because it can accelerate the projectile to a higher velocity using less pressure. Table 6 compares the velocity that Helium, air, and Nitrogen could propel the projectile assuming $m_p=183.5g$, $p_I=1.02MPa$. As shown, the projectile was able to move 24% faster using Helium than air or Nitrogen at the same pressure.

Table 7 and Figure 18 compare the predicted and the measured impact velocity versus the gas pressure. It shows that, in the majority of tests, the velocity generated with this estimate was

within $\pm 5\%$ of the targeted velocity. The recorded maximum error was 7.53%. Overall, this method provided a good estimation for the required gas pressure for a targeted velocity.

Table 5 initial and calculated parameters of the gas gun system. Items on the left are known, and items on the right are calculated through the solution process. For IT_6 through IT_10, use V_1^* and V_2^* from earlier gas gun setup.

Variables	Description	Value
R	Gas constant for He (kJ/kgK)	2.07
c_v	Specific heat constant volume (kJ/kgK)	3.12
n	Polytropic efficiency	1.26
V_1	Volume of pressure vessel (m^3)	0.03
V_2	Volume of pressure vessel and barrel (m^3)	0.073
V_1^*	Volume of pressure vessel (m^3)	0.014
V_2^*	Volume of pressure vessel and barrel (m^3)	0.057
T_1	Room temperature of gas in pressure vessel (K)	295
v_1	Initial Velocity	0
v_2	Velocity at end of barrel (just before impact)	Chosen
m_p	Mass of projectile/sabot	Measured


 Solve equations

Variable	Description
T_2	Final temperature
m_{gas}	Mass of gas
p_1	Initial vessel pressure
p_2	Final pressure of system

Table 6 predicted velocity of projectiles at different gases for $m_p=183.5g$, $p_1=1.02MPa$

Gas	Gas Constant (kJ/kgK)	Specific Heat at Const. Vol. (kJ/kgK)	Velocity (m/s)	Ratio to Helium
Helium	2.077	3.12	397	1
Air	0.287	0.718	301	0.758
Nitrogen	0.297	0.743	303	0.764

Table 7 predicted (n=1.26) and measured impact velocity versus the gas pressure

Test #	Mass (g)	Pressure (kPa)	Predicted Velocity (m/s)	Measured Velocity (m/s)	Error (%)
IT_6	187.6	1241.1	376	360	4.47
IT_7	188.0	1241.1	376	372	1.02
IT_8	185.0	827.4	315	330	-4.55
IT_10	183.0	1241.1	381	364	4.62
IT_11	182.6	1241.1	462	455	1.58
IT_12	179.9	1241.1	466	467	-0.32
IT_13	181.0	758.4	371	350	6.11
IT_14	179.8	1137.6	448	455	-1.65
IT_15	178.5	1206.6	461	429	7.53
IT_16	183.5	896.3	397	385	3.22
IT_18	183.0	827.4	384	387	-0.78

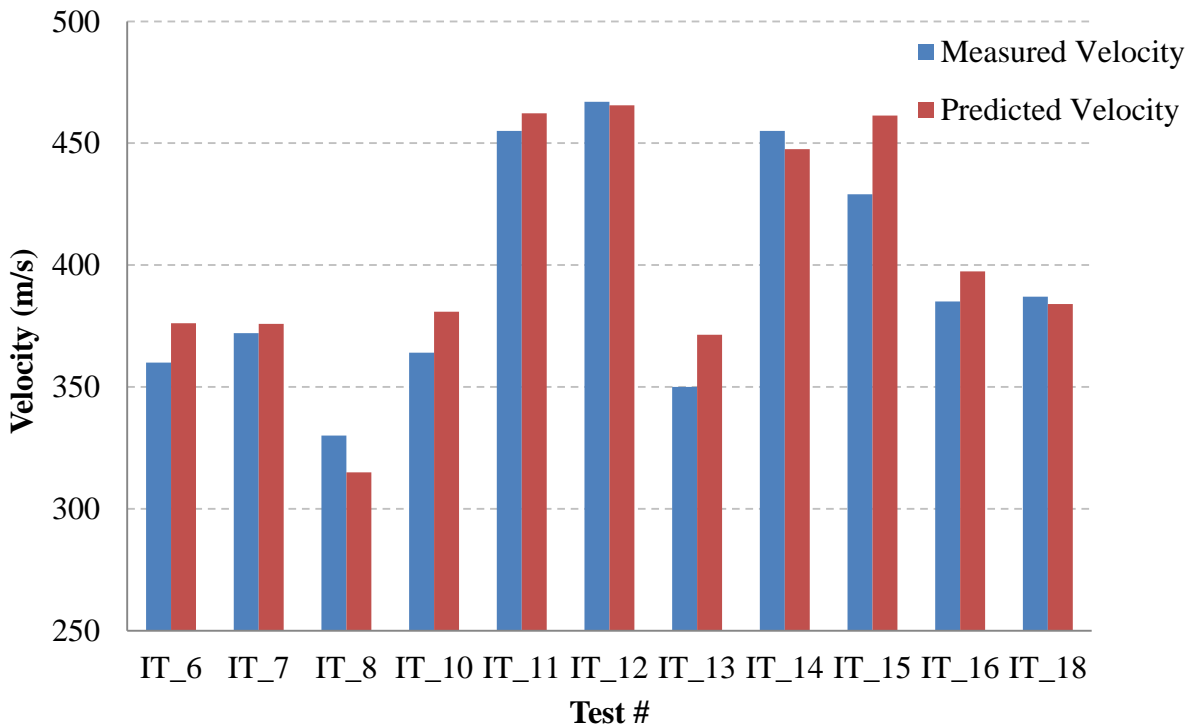


Figure 18 predicted and measured impact velocity

4.2.5 Transmitted Impact Force Measurement

So far, there are few established methods to measure the transmitted impact force in a high velocity gas gun experiment, unlike medium velocity instrumented drop tests. The instrumented projectile [52] is relatively expensive. The instrumented target was made of a load cell attached to a deflector plate [51]. It was used to measure the transmitted impact force (TIF) of a soft projectile made of gel or rubber.

In this work, the measurement of TIF on the target was attempted with resistance strain gage based load cells mounted behind the testing frame which holds the target. The load cells were manufactured from 6061 aluminum rods in house. The finished load cell has a tubular configuration with an outer diameter of 38.1mm, an inner diameter of 19.1mm and a length of 50.8mm. The diameter of the load cells was selected to give appropriate sensitivities for the estimated expected load. The length of the load cells was kept short to allow for maximum development of wave reflections within the load cell and reduce the inertia effects seen in [51]. Each load cell is instrumented with four strain gages in a full bridge configuration as shown schematically in Figure 19. The load cells were calibrated using an MTS loading frame with an MTS load cell of 10kN. The strain gage signals were amplified with 100 kHz Vishay amplification cards, acquired by an NI 9223 module and recorded with NI LabView Signal Express.

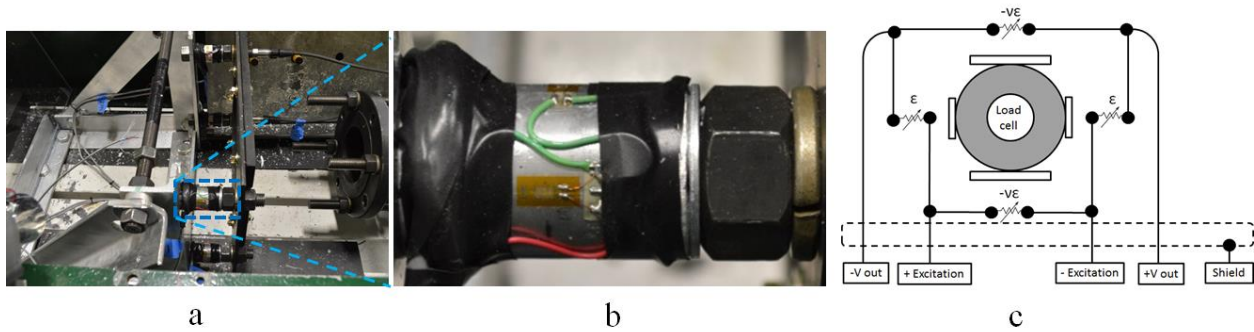


Figure 19 (a) the four resistance strain gage load cells and their mounting in the target retainer system. (b) Close up view of a load cell. (c) Load cell schematic for full bridge configuration where two diametrically opposing gages are mounted off axial direction as denoted by $-ve$ where ν is Poisson's Ratio.

Four load cells were used to measure the TIF in the gas gun experiment. The load cells were located at the four corners of a steel testing frame, as shown in Figure 20. They are carefully fixed between the testing frame and a rigid fixture and pre-loaded by a center mounted bolt and nut. Then the composite testing panel is fixed to the testing frame with 24 $\frac{1}{4}$ -20 equally spaced bolts on a 136.7mm (5.37in) radius and annular shaped ring to evenly distribute the bolt pre-load on the composite. Clearly the testing frame has a circular opening 254mm (10in) for the projectile to pass through. During impact, the force was transmitted from the composite panel to the load cell through the testing frame. The TIF was calculated as the summation of the four load cells.

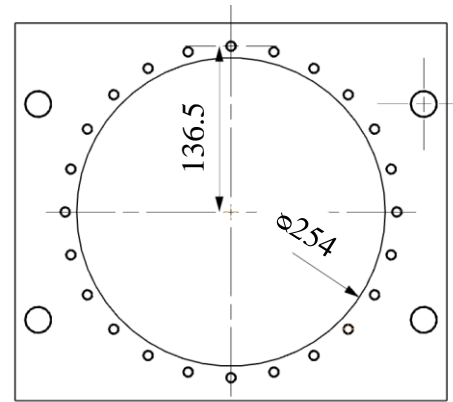
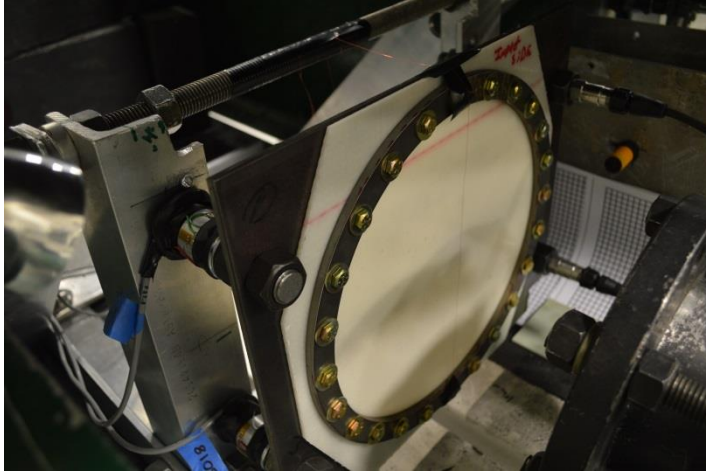


Figure 20 isometric view of testing frame with panel installed. The thin wire in center of panel provides a switch for triggering and synchronizing of data acquisition equipment. On the right is a schematic of the circular frame with a 24 count hole pattern on a radius of 136.5mm (5.375in), specimen test radius of 127.0mm (5in), and test area of 0.05067m².

4.2.6 Out-of-Plane Deformation Measurement

The out-of-plane deformation was measured with a projection grating profilometry method. The experimental set-up includes a camera, a digital projector, and a computer, as shown schematically in Figure 21. By using the digital projector, only one frame of parallel fringe pattern with cosine function modulated intensity is projected onto the object with an incidence angle. The camera is placed normal to the reference plane, thus the deformed fringe patterns modulated by the surface profile of the object can be captured. After a calibration test, the surface profile can be extracted by calculating the fringe deformation between the reference and the detected surface. The details of the analysis are omitted here. The interested readers can refer to [58]–[60].

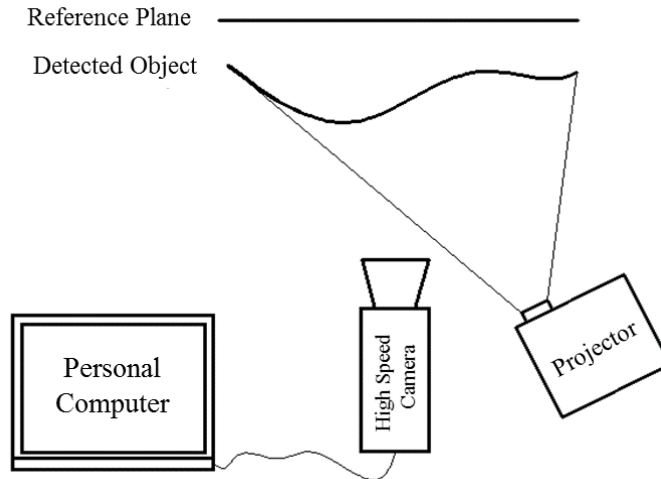


Figure 21 the schematic of the projection grating profilometry experimental setup for the out-of-plane deformation measurement.

4.2.7 Composite Panel Manufacturing

The composite panels were made of S2-glass plain weave (5x5) fabric with areal weight of 0.81 kg/m² and API SC-15 toughened epoxy resin. The vacuum assisted resin transfer molding method (VARTM) is used to manufacture the panels. VARTM is a cost effective way to manufacture higher volume fraction composites [61]. The schematic of VARTM is shown in Figure 22. The glass fabric layers were laid onto a flat tool plate to form a laminate with fibers in 0 and 90 orientations. The resin was introduced under vacuum. The composite was vitrified at 60°C for 2 hours, then post-cured at 94°C for 4 hours with a ramp rate of 1-2°C per minute. The manufactured composite plates had a nominal thickness of 0.62 mm/ply. The thickness of the 6-ply and 10-ply composite plates used in this study was 3.85±0.31mm and 6.19±0.05mm, respectively.

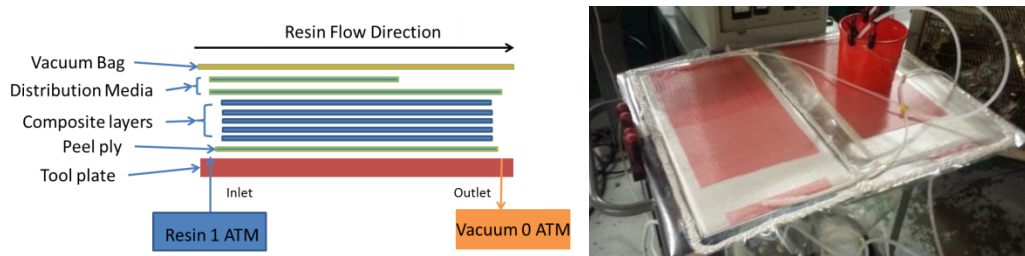


Figure 22 manufacturing composite panels using VARTM Process.

The manufactured composite plates were cut to 300mm x 300mm square panels for testing with an abrasive diamond face saw. Additionally, a 51mm x 102mm triangle was cut from each corner to allow the panel to fit in the testing fixture as seen in Figure 20. Each panel was drilled to have 24 equally spaced 6.4mm (0.25 in) holes and bolted to the testing frame shown in 6. The bolts were carefully fastened with a torque wrench to a torque of 16.3 N-m (12.0 lbf-ft).

4.2.8 Post-mortem Inspection

The tested composite panels were inspected visually and with a backlighting photography method. The experiment set-up consists of a Cree CXA 1520 high density LED array with a Carclo 45° mirror reflector positioned 0.31m away from the backside of the panel. The photos were taken with a Nikon D3200 camera with a variable 18-55mm lens from a distance of 1.22m. The photos were post processed in MATLAB where images were converted to gray scale using function *rgb2gray* and the contrast was enhanced with function *imadjust*. This method allows for easy observation of delamination damage in glass fiber composites.

4.3 Results and Discussion

Table 8 provides a summary of the gas gun experimental results. A total of twelve panels were tested; four of them were 10-ply and the other eight were 6-ply. The measured initial projectile velocity v_i ranged from 300m/s to 449m/s. From the initial velocity and the mass of the projectile, the initial kinetic energy of the projectile E_i was determined.

In nine experiments, the projectile perforated the panel where the residual velocity of the projectile v_r had a positive value. The projectile rebounded in tests IT_8, IT_10, and IT_17. For these three cases, the maximum deflection was determined from the out-of-plane deformation measurement. The values are reported in Table 8. From v_r , the residual kinetic energy of the projectile E_r can be determined. The absorbed energy E_a is determined from the change in the kinetic energy of the projectile as

16

$$E_a = E_i - E_r$$

Since very little damage had occurred to the tested projectiles, E_a can be attributed to the energy absorbed by the panel. The values are listed in Table 8. The specific energy absorption of the target panel was calculated by dividing E_a with the mass of the panel in unsupported area, i.e. the circular opening area shown in Figure 20. The values are listed in Table 8. The average specific energy absorption was 7.69kJ/kg and 6.89kJ/kg for the 6-ply and 10-ply panels, respectively. The 6-ply panel was 12% more efficient than the 10-ply panel in this regard.

Table 8 gas gun experimental results

Test (#)	Areal Weight (kg/m ²)	Target	v _i (m/s)	v _r (m/s)	E _i (kJ)	E _a (kJ)	Target Specific Energy (kJ/kg)	Result/Max Deflection (mm)
IT_6	6.53	6ply	360	94	3.89	3.62	10.95	Perforation
IT_7	6.53	6ply	374	211	4.20	2.86	8.63	Perforation
IT_8	6.53	6ply	321	-23	3.09	3.08	9.30	28.3
IT_10	10.66	10ply	375	-23	4.22	4.20	7.78	23.0
IT_11	10.66	10ply	458	346	6.29	2.70	5.00	Perforation
IT_12	6.53	6ply	449	370	6.05	1.94	5.87	Perforation
IT_13	6.53	6ply	359	199	3.87	2.67	8.08	Perforation
IT_14	10.66	10ply	443	270	5.89	3.71	6.86	Perforation
IT_15	10.66	10ply	438	206	5.76	4.48	8.30	Perforation
IT_16	6.53	6ply	383	268	4.40	2.25	6.79	Perforation

**v_r-initial projectile velocity, E_{ki}-initial projectile kinetic energy, v_r-residual velocity of projectile, (-) implies rebound. The target specific energy absorption was calculated by E_{ki}/mass of the test area. The test area =506.7cm². The mass of the test area is 331g for the 6-ply and 540g for the 10-ply panels.*

***IT_17 Max Deflection unavailable*

4.3.1 Ballistic Limit

The ballistic limit is the velocity required for a particular projectile to penetrate a particular target. In this work, the ballistic limit was defined as the velocity that results in a residual velocity of zero. The residual velocities were plotted against the initial velocities for the twelve experiments in Figure 23. The point with the fastest velocity that caused rebound and the point with the slowest velocity that had no rebound were fitted by a linear trend line. The interception of the fitted line with the x-axis yielded the ballistic limit. The value was 329 m/s and 381 m/s for the 6-ply and 10-ply composites, respectively. It is interesting to note that the ballistic limit did not increase proportionally with the panel thickness. The ballistic limit of the 10-ply panel is only 16% higher than that of 6-ply. The lower efficiency in energy absorption of the 10-ply panel may be caused by the change in damage mechanisms and dominate failure modes at higher speeds and increased structural rigidity of the panel.

Error estimation of approximately $\pm 3\%$ was predicted [6] for testing of various heat treated metals. Ballistic limits of the composite targets manufactured here could have higher error due to manufacturing variability of the composite panels.

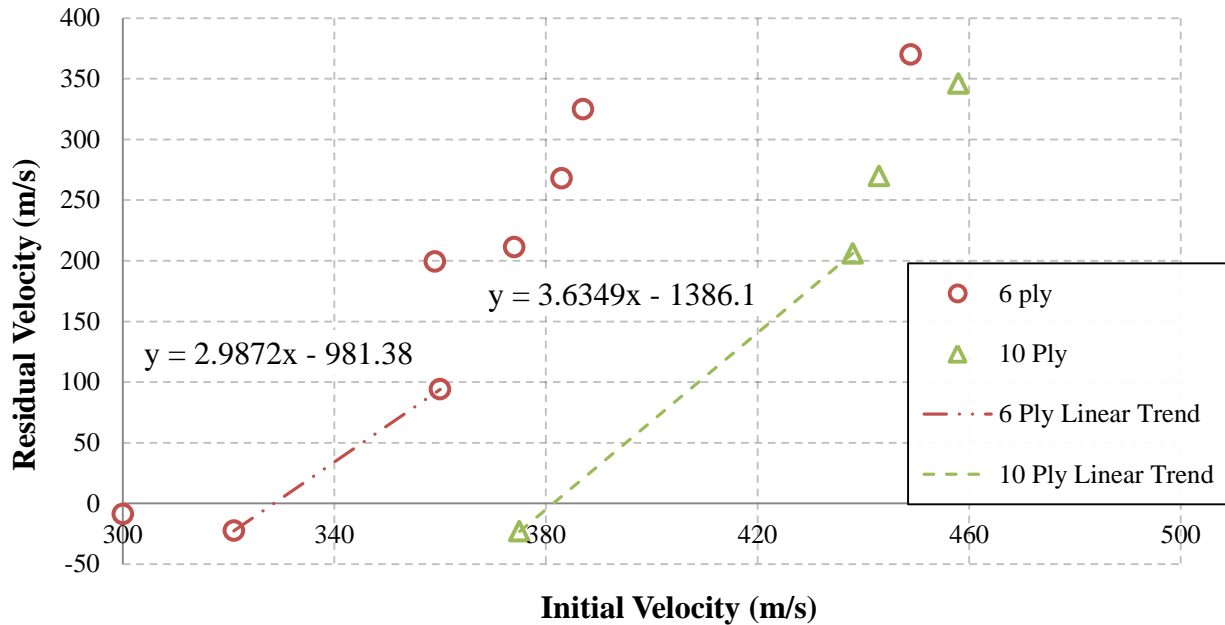


Figure 23 material ballistic limit is determined at the x-axis intercept of a linear trend line from residual vs. initial velocities

4.3.2 Force and Deformation Histories

Figure 24 plots the force history curves from the load cell measurement. Figure 25 presents the value of the peak force versus the impact velocity of the projectile. As seen, the highest forces were recorded for the two panels tested under the ballistic limit, with a maximum value of 38kN and 30kN for the 10-ply and 6-ply, respectively. For the tests above the ballistic limit, the force registered by the load cell decreased with the velocity of the projectile. At 449 m/s, the recorded maximum force on the 6-ply was only 454 N, merely 1.5% of the force recorded from IT_6 (v_i below the ballistic limit). The lower recorded force values at higher projectile speeds indicate that the failure on the panel became more localized and independent of the boundary condition. As suggested by Roberts et al [7], in a high velocity impact scenario, the failure modes observed

from panels of simple geometries may closely match the failure modes seen on a complex structure.

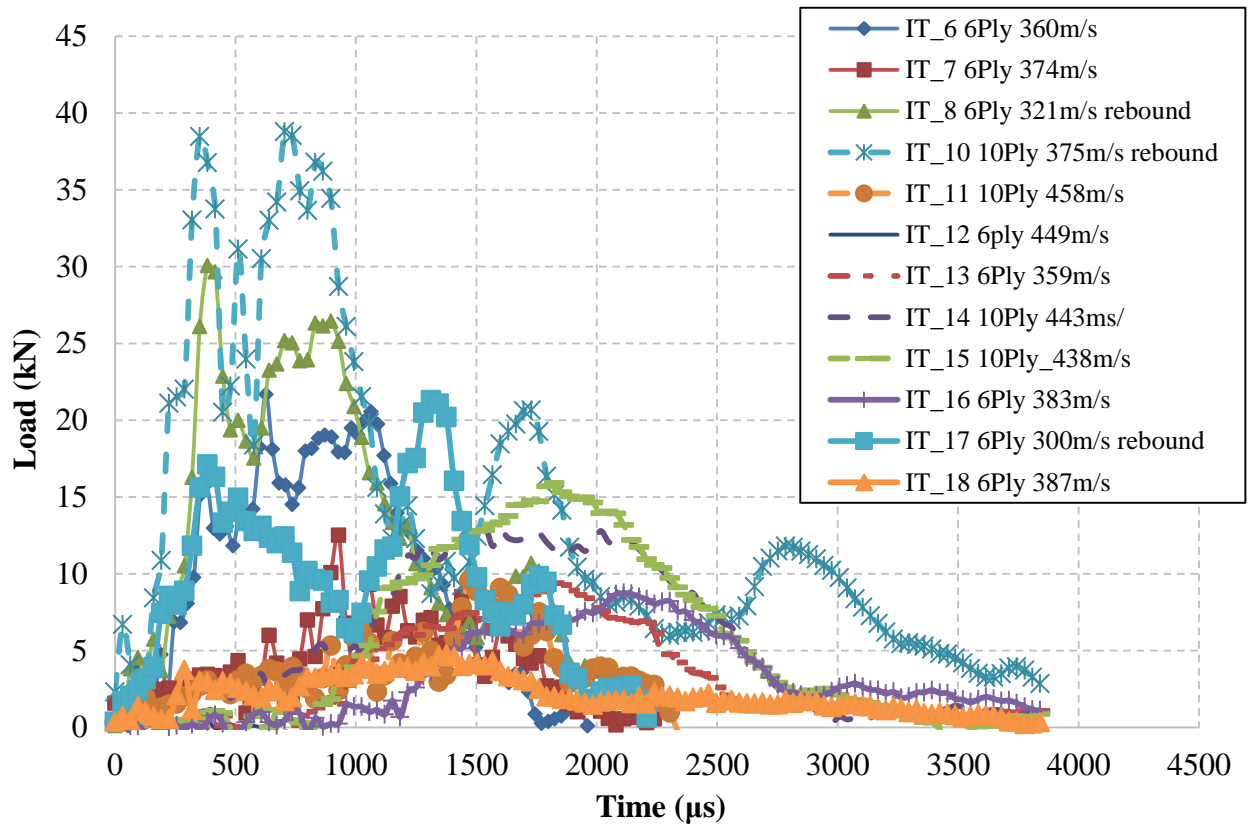


Figure 24 the force history traces recorded by the load cell. The force is the summation of four load cells.

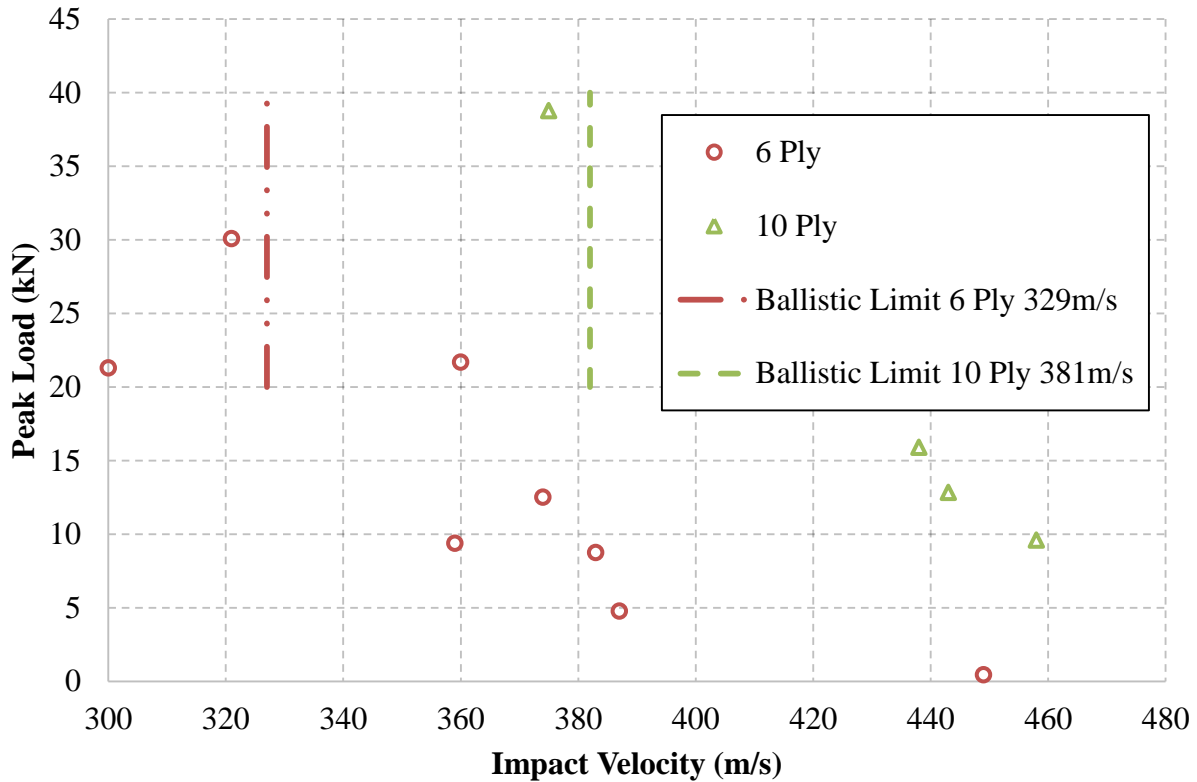


Figure 25 the recorded peak force versus the impact velocity of the projectile.

The out-of-plane deformation measurement using the projection grating profilometry was successful with the two panels tested under the ballistic limit (no perforation). The results are shown in Figure 26. Under the impact of a cylindrical projectile, the panel displayed a cone shaped deformation. The cone expanded in size and then retreated.

A comparison between the force and deformation measurements helps to identify the origin of the peak forces registered by the load cells. Figure 27 plots the out-of-plane displacement history at the center of the two panels. For IT_10, the panel reached the maximum deflection at 216 μ s and then reflected back, passing zero at 1134 μ s and then reached the maximum in the opposite direction at 1458 μ s. In Figure 24, the first peak force for IT_10 occurred at 352 μ s, corresponding to the maximum deflection of the plate. The delay of the load cell signal is therefore estimated to be about 136 μ s. The peak force at 1700 μ s may be related to the maximum deflection in the

opposite direction. On the other hand, the peak force for IT_10 at 760 μ s is not associated to a particular deformation event and therefore it was likely caused by the reflected wave within the load cell.

In the tests above the ballistic limit, failure occurred through the thickness of the composite panels. In the experiment, upon initial impact, a bright lighting phenomenon was observed. This degraded the initial fringe pattern to be used in the analysis. Soon after, matrix resin disintegrated into dust which obstructed the view of the video camera and fringe projector, causing the out-of-plane deformation measurement to be unsuccessful for the panels that were perforated.

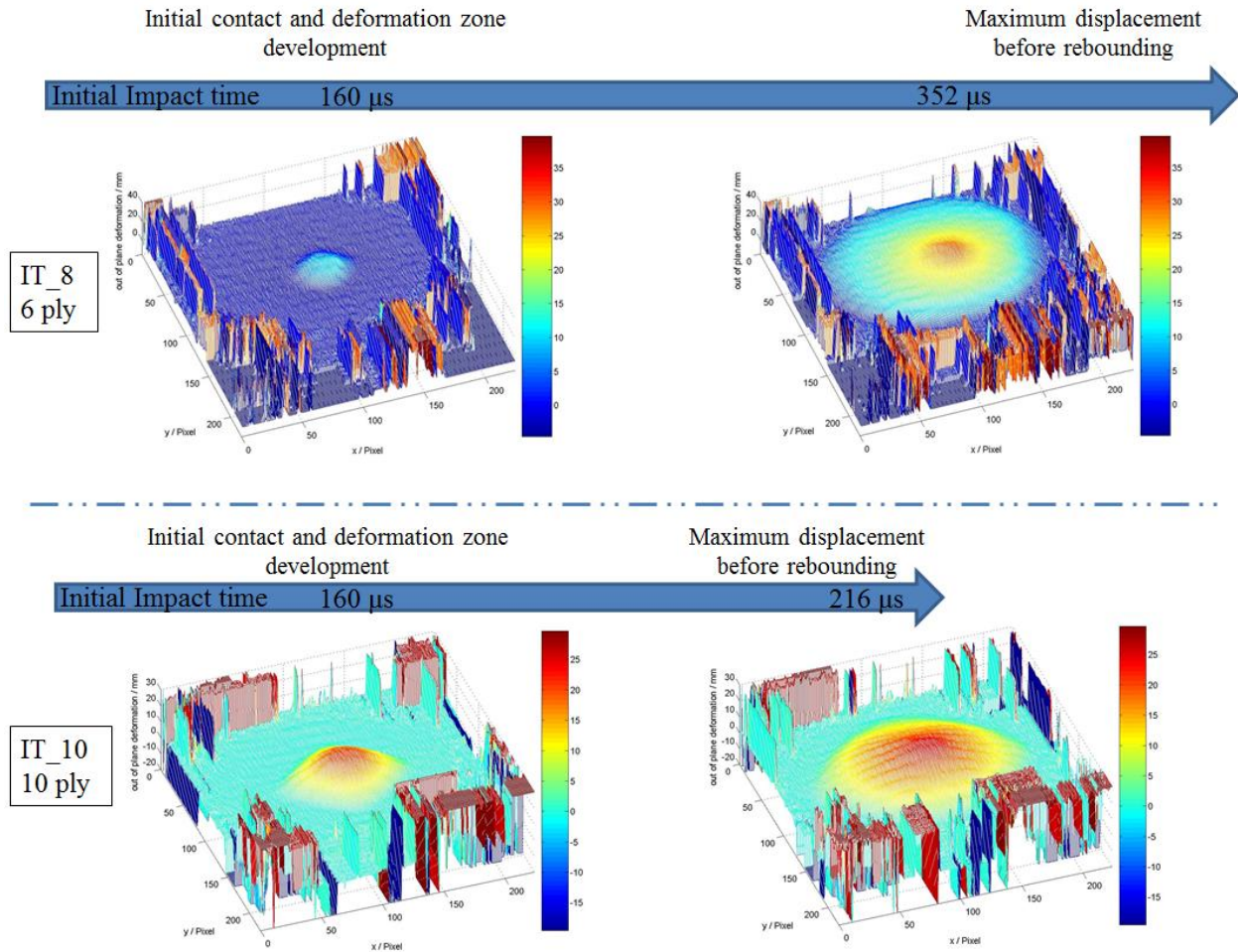


Figure 26 3D profile of the back side of the panel during impact testing under the ballistic limit. The 10 ply panel (IT_10) reached the maximum displacement 136 μs before the 6 ply panel (IT_8).

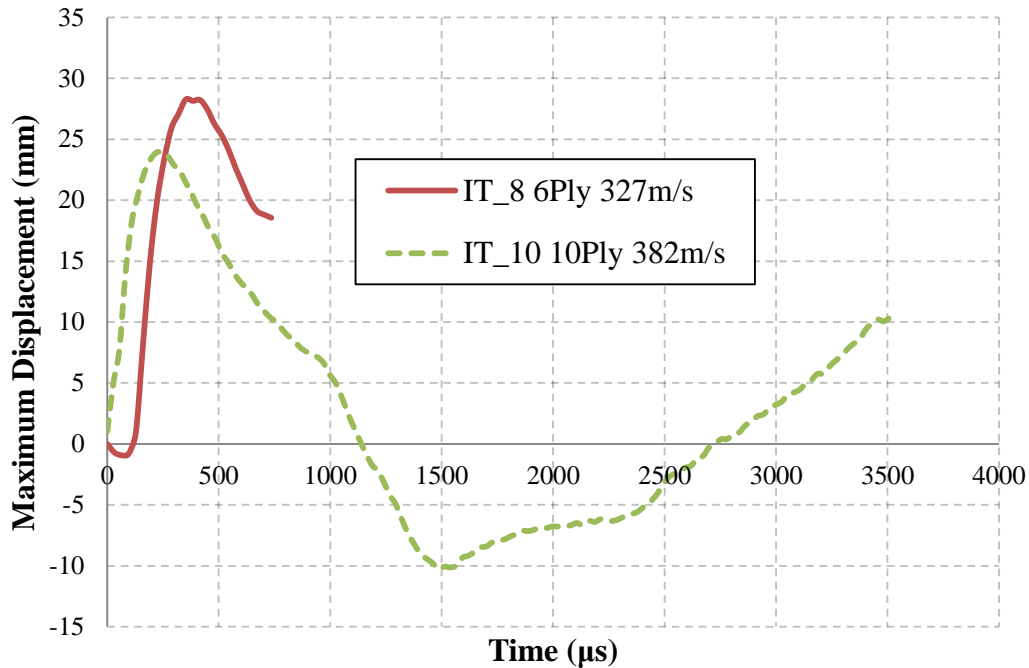


Figure 27 the maximum displacement on non-perforated 6 and 10-ply panels

4.3.3 Energy Absorption

Figure 28 plots the energy absorption versus the initial velocity for the 6-ply and 10-ply panels, respectively. It shows that above the ballistic limit, a panel can absorb the same or even a slightly greater amount of energy with increasing velocity. Literature data indicates that this region would end at a critical velocity [62], [63] where the energy absorption reaches a peak value.

Accordingly, the energy absorption behavior can be divided into three regions: Region I - below the ballistic limit; Region II - from the ballistic limit to the critical velocity; and Region III – above the critical velocity, as indicated in Figure 28. Judging from the energy absorption, the impact test at 449m/s for the 6-ply panel might have exceeded the critical velocity.

4.3.4 Damage and Failure Mode Analysis

The damage and failure in a glass fiber composite was inspected visually and with the backlighting photography technique. It reveals that the failure modes change depending on the

impact velocity. Figure 29 presents the backlighting images of tested panels and a summary of the visually observed failure modes. In all images, the fiber tows in the composite panel were oriented in the vertical and perpendicular directions.

In Region I, the dominating failure modes were matrix crushing. For the 6-ply panel, five major cracks, each with minor fiber pull out, were observed on the top surface. Delamination occurred but was limited to the top layer only. On the backlighted panels, delamination regions are seen visibly as fringes. A single fringe indicates that delamination occurred at one interface. There was no visible damage at the backside of the panel. The 10-ply panel had a few more short cracks and a similar delamination area.

In Region II, the projectile perforated the panel. The dominate failure mode was shear failure. A shear plug or circular cutout was observed on the top layers. At the back side, fiber tows were protruded out of the panel and formed a hut, as shown in Figure 30. These fiber tows had little resin on them. As mentioned above, in the impact tests above the ballistic limit, the matrix resin disintegrated into dust at the back side of the panel. The post-mortem confirmed this observation. The second characteristic failure mode is delamination at multiple interfaces. Multiple fringes are visible in the backlight images. The outermost fringes corresponded to the back side of the panel where the projectile exits. The images at different impact velocities show that delamination increased with velocity. Furthermore, the number of the major cracks increased with impact velocity.

Test IT_12 might mark the beginning of Region III. The dominate failure mode was still shear but the failure was rather localized. The shear failure went all the way through the panel. At the

back side, the protruded fiber tows formed a taller hut, as shown in Figure 30. The major cracks were shorter and the delamination areas were smaller.

The impact tested panels were no longer flat but slightly warped. The depth of the deformed shape was largest at the center of the panel. This depth was designated as d_p . Its value for each test was measured and reported in Figure 29. All panels except IT_8 bulged towards the back side and the measured d_p ranged from 3.3mm to 8.8mm. IT_8 bulged towards the impact side with a d_p =-9.2mm.

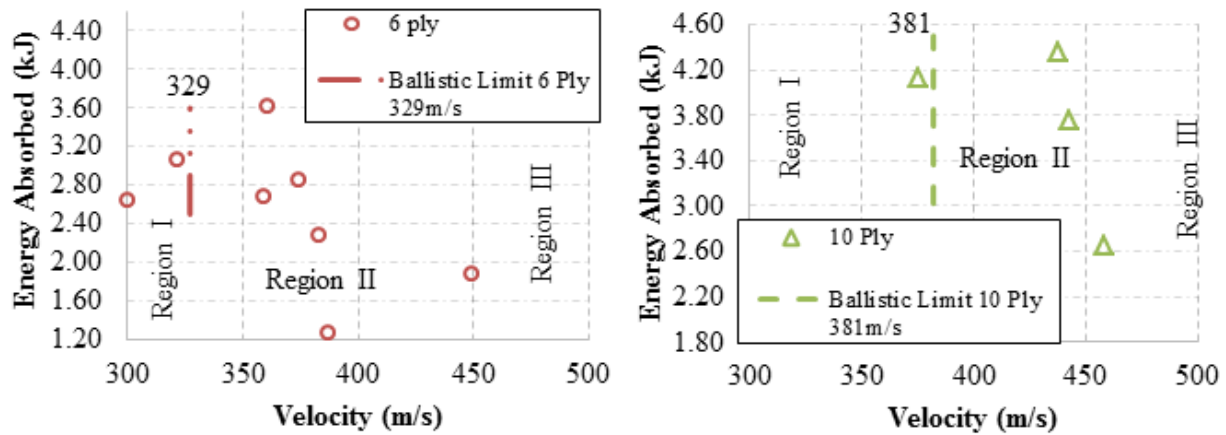


Figure 28 energy absorption vs initial projectile velocity.

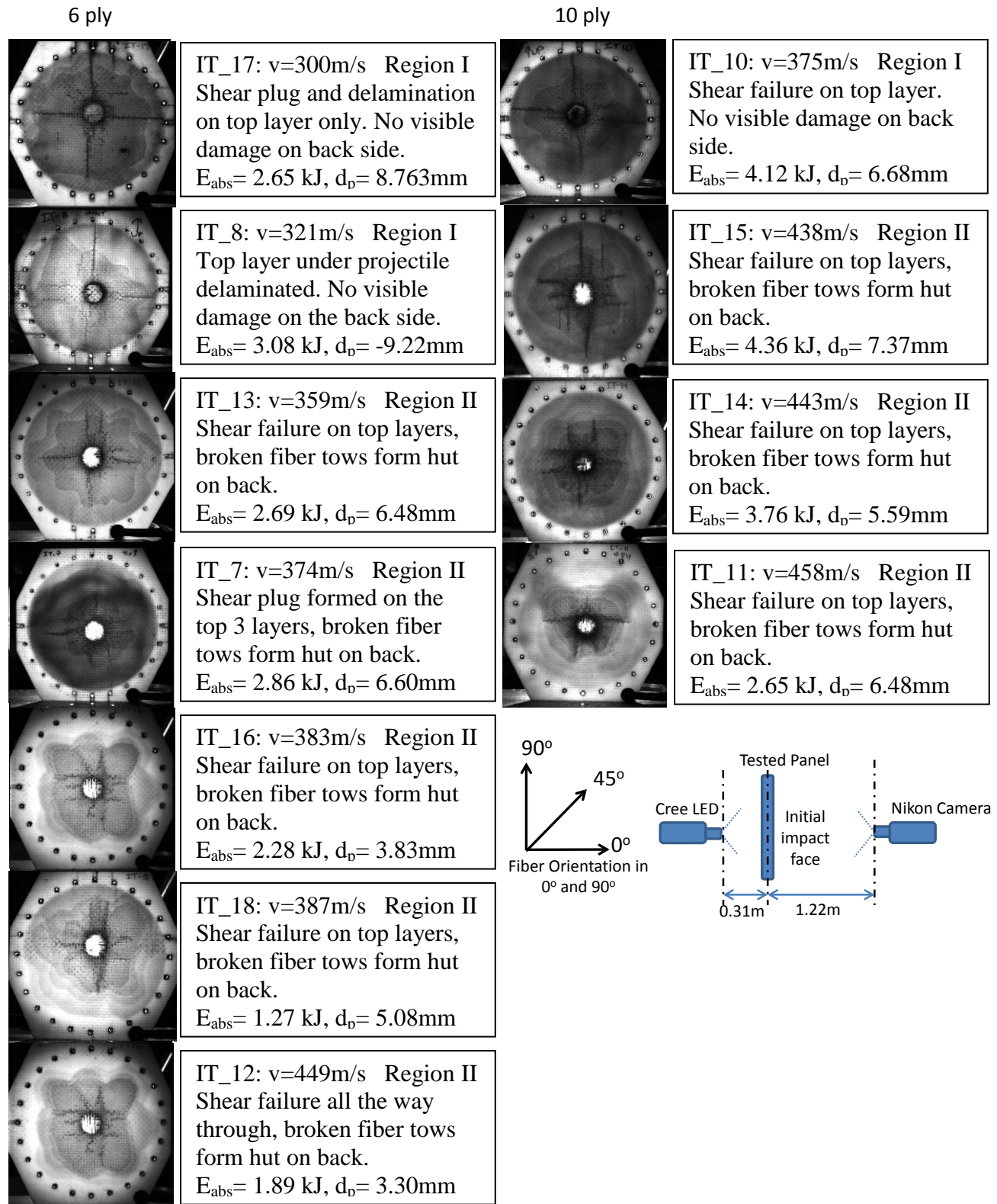


Figure 29 the inspection of tested panels with LED backlight. The surface shown is the impact face.



Figure 30 the back side of the composite panel from IT_12, 6-ply panel tested at 458m/s: dry fiber tows are protruded and form a hut shaped sub-structure.

4.3.5 Comparison of Energy Absorption at Ballistic Limit

The ballistic limit depends on the shape and mass of the projectile and the configuration of the target. Although ballistic limit data are available for a variation of materials in literature, it is difficult to compare the ballistic protection capability of different materials. In this work, different materials are compared by E_{BL} , the projectile kinetic energy at the target ballistic limit normalized by the contact area of the projectile with the target, versus the areal weight of the target, as shown in Figure 31. The data compared here are for projectiles with a blunt head, such as a flat face or a semispherical shape. The contact area is defined as the maximum cross section of the projectile. The sources of these data are provided in Table 9. This plot allows one to determine the required areal weight for a specific material to stop a blunt projectile of certain mass and velocity.

Figure 31 shows that the S2-glass plain weave/SC-15 epoxy composite has excellent ballistic protection capability compared to other materials. Other high efficiency materials are Inconel 718 heat treatment (HT) B and HTA.

Table 9 data sources for Figure 31

Material	Areal Weight (kg/m ²)	E _{BL} (J/cm ²)	Source
S2-glass	6.5	283.1	This Study
	10.7	356.4	This Study
	3.2	95.1	[64]
Inconel 718 HTA-D	8.35-16.7	155.6-438.3	[6]
AS4	3.1	16.0	[65]
	6.2	40.8	
E-glass	7.5	153.5	[27]
	3.5	160.4	
	3.7	97.0	[66]
T300 Carbon	2.8	50.5	[27]
	3.0	66.3	[66]
Mild Steel	All points	All points	[67]
2014A TB Aluminum	All points	All points	
1200 Aluminum	All points	All points	

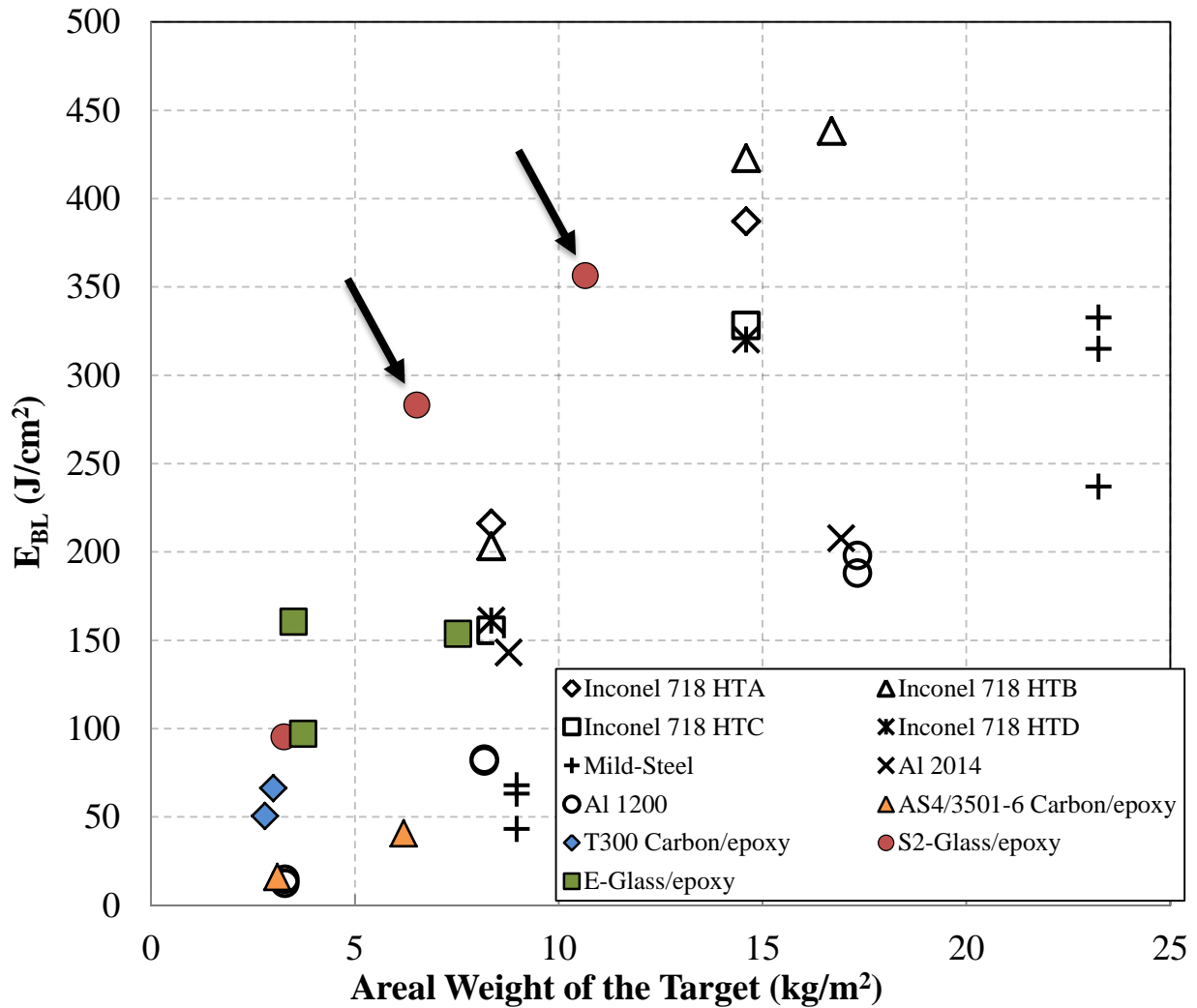


Figure 31 comparison of E_{BL} , the energy absorbed by the target material at the ballistic limit normalized by the contact area, versus the areal weight of the target. Material tested in this work is identified by arrows.

4.4 Conclusions

To improve the gas gun experiment, several new technologies were experimented. The measurement of the TIF was attempted with four load cells attached to the testing frame. The out-of-plane deformation of the target panel was measured using a projection grating profilometry method with a high speed camera. This deformation measurement was successful

for tests ran with velocities below the ballistic limit (rebound) and failed at velocities above the ballistic limit (perforation).

To calculate the required gas pressure for a targeted velocity, a thermodynamic analysis based method is derived. The results showed that, for the majority of tests, the velocity generated with this estimate was within $\pm 5\%$ of the targeted velocity. The recorded maximum error was 13.3%.

The high velocity impact behavior of S2-glass plain weave/SC15 epoxy composite panels was investigated. With a cylindrical aluminum projectile of 60g, the ballistic limit was 329 m/s and 381 m/s for the 6-ply and 10-ply, respectively. In terms of specific energy absorption, the 6-ply panel was 12% more efficient than that of 10-ply.

In the range of impact velocity from 300m/s to 458m/s, the energy absorption of the composite panels maintained and even increased with velocity. The failure modes of the panels evolved with the velocity. The damage and failure first increased in size with velocity and then became more localized. In 458m/s impact, the force registered by the load cells is only 1.5% of that at 321m/s, indicating that failure is localized and independent of the boundary condition.

By plotting E_{BL} , the projectile kinetic energy at the target ballistic limit normalized by the contact area of the projectile, versus the areal weight of the target, the ballistic protection capability of different materials can be compared. S2-glass/epoxy composite is ranked high in ballistic capability.

4.5 Summary

The single-stage gas gun testing methodology was investigated. The transmitted impact force (TIF) was measured with four load cells installed behind the target. The out-of-plane deformation was measured with a projection grating profilometry method using a high speed

camera. The velocity of the projectile was determined using images from the high speed footage. The force and deflection measurements were successful for tests conducted below the ballistic limit. To estimate the required gas pressure for a targeted velocity, a thermodynamic based relationship was proposed. The improved gas gun experiment was used to investigate the high velocity impact behavior of a S2-glass/SC15 epoxy composite. With an aluminum cylindrical projectile of 60g, the ballistic limit was found to be 329 and 381 m/s for the 6-ply and 10-ply composite panels tested, respectively. Beyond the ballistic limit, the panels can still absorb the same or even a slightly higher amount of energy until a critical velocity. The failure modes of the composite panels evolved with velocity. The area of damage and failure first increased with velocity and then became localized. Finally, a new method to compare the ballistic protection capability of different materials is proposed.

CHAPTER 5 COMPARISON OF IMPACT DAMAGE FROM SPIN PIT AND FLAT PANEL
GAS GUN TESTING

5.1 Introduction

In aircraft engine certification, one of the requirements is to demonstrate the engine's ability to withstand a fan blade-out (FBO) event per 33.94 FAA regulation [2]. Traditionally, fan cases for blade containment are made of metallic materials [5]. The analysis and design procedures for metallic containment cases against FBO are relatively mature. In comparison, much less information is available for the design of a composite containment system [68].

NASA Glenn Research Center (GRC) has pioneered the research into the development of methods for the design of jet engine containment cases [5]–[8]. The method relies on simulating the damage on containment cases in FBO event through ballistic impact experiments. This approach is much more cost effective as compared to engine blade-out testing. It was found that the laboratory scale ballistic testing can generate damage modes on targets similar to that of the initial impact on a fan case in engine FBO tests. However, such experiments must be carefully designed. A number of parameters may influence the damage modes, such as (a) the design of the projectile; (b) the orientation and shape of the projectile; and (c) the configuration and orientation of the target. The relationships between the ballistic testing and FBO tests have not been thoroughly examined.

A spin testing facility and a single-stage gas gun have been developed at Michigan State University (Figure 32). The spin apparatus allows one to perform the FBO test under conditions similar to an engine blade-out test in a controlled manner and to acquire data to improve our understandings of this process. The gas gun is used to perform ballistic impact simulated experiments. These experimental facilities enable a systematical investigation of the relationship between ballistic experiments and FBO tests.

This paper is to focus on projectile design in the development of a flat panel gas gun testing methodology as an accurate substitution for FBO in spin testing. In spin testing, the released blade has two velocity components: the rotational and translational. In gas gun testing, the projectile has only the translational velocity. To account for the influence of the rotational velocity, three projectile designs were investigated: (I) a blade segment the same as that in spin FBO tests, i.e. neglecting the rotational energy; (II) a projectile with a modified geometry such that it has the same energy profile across its span as the released blade in FBO; and (III) a pre-bent blade segment similar to the deformed shape of a released blade after FBO tests.

5.2 Experimental Setup

5.2.1 Spin Pit Set-up and FBO Experiment

Figure 32 shows the spin testing facility at Michigan State University. This set-up is conceptually similar to that in [69]. The three major components are a vacuum testing chamber, a drive motor, and a testing rig.

The cylindrical vacuum chamber has dimensions of $\Phi 1829 \times 1016$ mm. The top plate has a 720mm diameter removable bulkhead for easy installation of small testing articles. Larger articles can also be tested by removing the entire top cover of the chamber. For FBO testing, two layers of ballistic liners, a steel ring of 63mm thickness, and layer of ballistic rubber bricks 200mm thick, have been installed. For imaging, the chamber is furnished with nine 305mm diameter view ports; eight located on top and one on the bottom. The view ports at the top are positioned to have 360° coverage of the testing article and allow for 3D digital imaging correlation (DIC) measurement and high speed cameras.

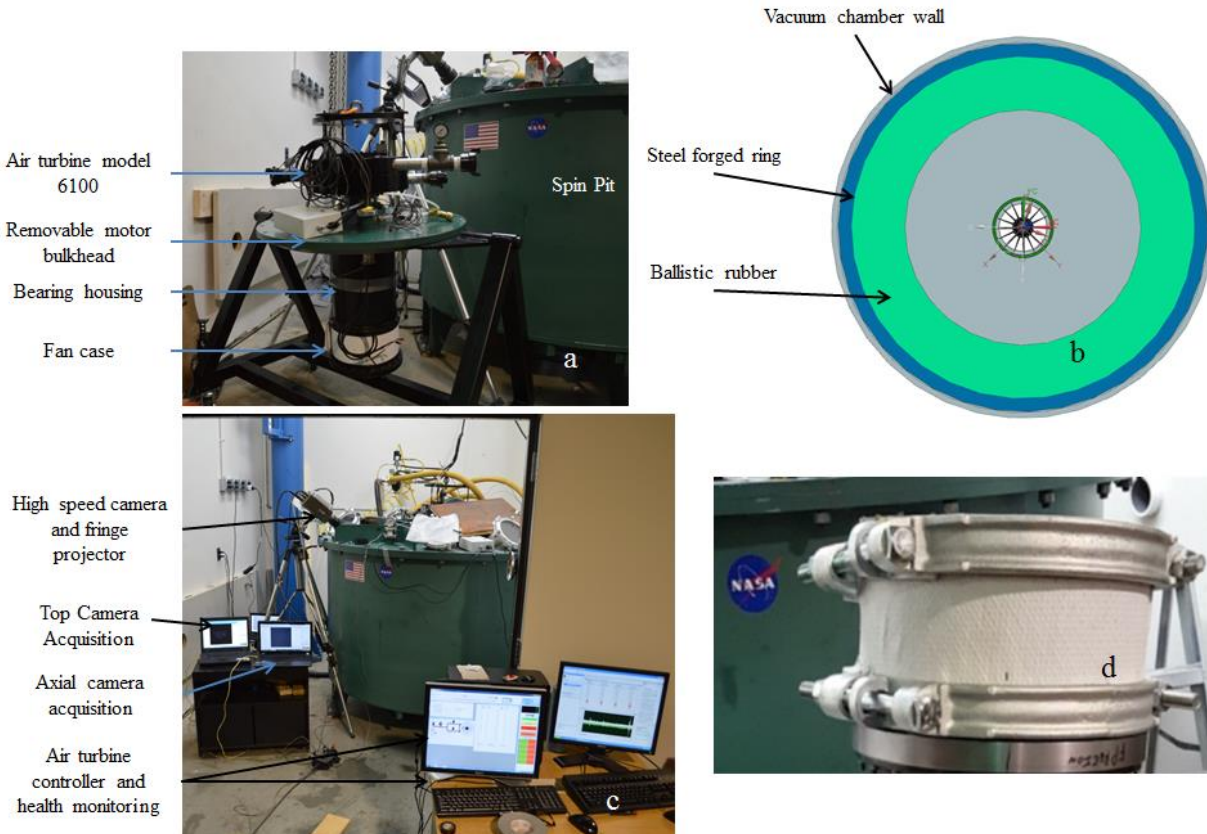


Figure 32 spin pit test facility: (a) vacuum chamber and testing rig; (b) schematic of the armored layers; and (c) data acquisition for fringe projection and axial high speed camera, air turbine controller, temperature and accelerometer health monitoring of rotating assembly. (d) A composite fan case is attached by clamps.

The drive motor is a BSI Model 6100 air-turbine from Barbour Stockwell, Woburn MA. It has a 40HP Pelton bucket-wheel design with a max speed of 40,000 RPM. The air turbine is integrated with oil lubrication and cooling for bearings as well as squeeze film dampers on front and aft bearings. The air turbine was carefully married to the top of the spin pit motor bulkhead with O-ring and stud attachment to a precision ground flat surface. In the work reported here, the compressed air was supplied to the turbine from a Doosan diesel air compressor model P600/XP535WCU-T4i.

The turbine is equipped with servo valves and a controller with précising controlling of clockwise or counter-clockwise/brake rotation of the drive. With transducers installed in the spin pit, the controller can monitor the bearing temperature, oil temperature, vibratory loads, and the speed, from which an abort or coast fault could be initiated which prevent the testing rig to be damaged from unexpected events. The turbine drive shaft quill is coupled to the shaft of the rotor through an aluminum coupler which is designed to fail after the FBO. This simple mechanical coupler effectively protects the air turbine from the dynamic unbalance load after FBO.

The vacuum is necessary to allow the 29.8kW (40hp) air turbine to attain the maximum operating speed. An Alpak model DA90LA-C vacuum pump was used in the current work. The 1.84m³ chamber was maintained with an absolute pressure of 600Pa (0.087psi) or less during the spin test.

The last component is the testing rig. It includes a shaft, a bearing house and a rotor assembly, as shown in Figure 33. The bearing housing has a modular design with inner and outer housings for easy replacement of components. Inexpensive low ABEC rated bearings were successfully used in the current work. The typical testing time was approximately 35s and the G2.5 balance tolerances required for a fan assembly were maintained [70]. The bearings were replaced after each test.

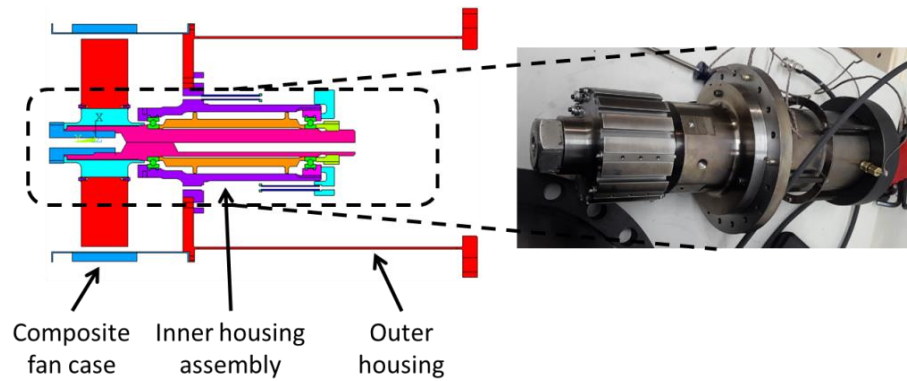


Figure 33 cross-sectional view of the rotating assembly including bearing house back structure and fan case (left). Assembled inner housing structure (right)

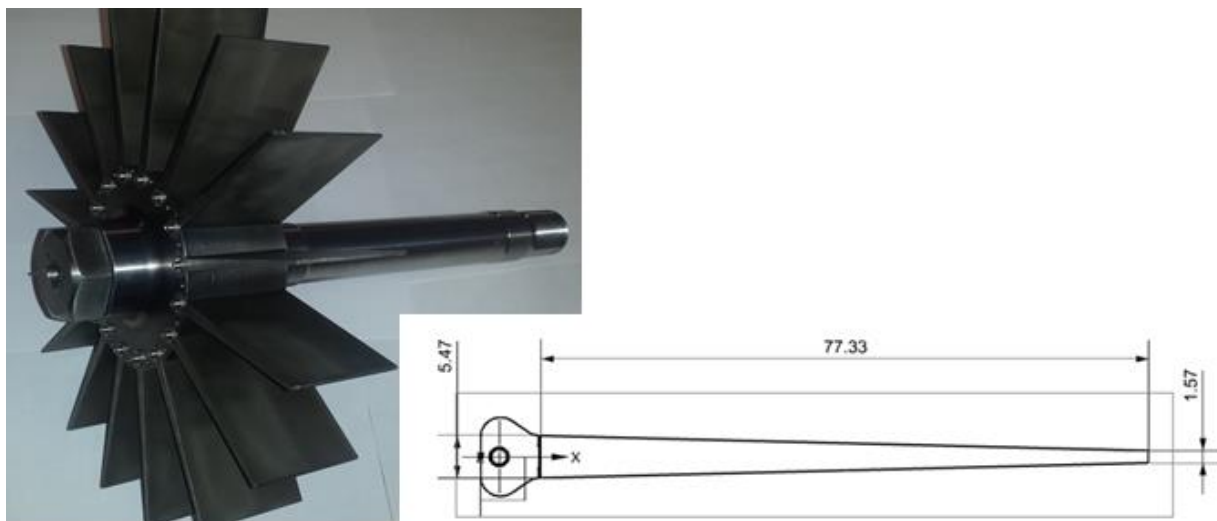


Figure 34 rotor and shaft assembly with a full set of blades, and the cross-sectional dimensions (in mm) of the blade.

Figure 34 shows the shaft and rotor assembly with a full set of blades and the cross-sectional dimensions of the blade. The blades slide into the hub via the dove tail feature and are bolted to the hub. The shaft, rotor and the blades were all made of Ti-6Al-4V.

In FBO testing, one of the blades needs to be released in a controlled manner. The reported blade release methods for FBO experiments include mechanical release system, magnetic blade

excitation, pyrotechnic release and notched blade [40]. Pyrotechnic release is the most precise method but it was not permitted at the current lab. The notched blade method was selected because it is relatively reliable and simple to implement. The notch was introduced near the root of the blade via die grinder. The release speed was predicted using a relationship between the notch depth and the release speed with the consideration of the notch concentration factor presented in [71].

In this work, the FBO testing was conducted with either one releasing blade and one balancing blade or one releasing blade and three short balancing blade segments.

5.2.2 Gas Gun Set-up

Figure 35 and Figure 36 show the schematic and photo of the single stage gas gun used in this work. The major components are a gun barrel, a pressure vessel, and a poppet valve. The steel barrel is 4.7m long with an inner diameter of 108mm. Compressed Helium is used in this work. More details about this gas gun can be found in [72].

As illustrated in Figure 35, the target may be placed either 90° or at an oblique angle α to the gun barrel. The projectile may be oriented parallel or at an angle β to the gun barrel. In the current work, the projectile is delivered by a lightweight sabot. A sabot arrester at the end of the barrel destructively stops the sabot and allows the projectile to pass to impact the target. The projectiles used in this work were made of Ti-6Al-4V.

Two high speed video cameras were used in the gas gun experiment. Camera #1, a Phantom V12.1, was used to determine the velocity and orientation of the projectile before impact and the residual velocity of a rebounding projectile. Camera #2, a Phantom V7 was used to determine the residual velocity of the projectile that had perforated the target [54] and for out-of-plane

deformation using a projection grating profilometry method to be discussed. The positions of the cameras are shown schematically in Figure 35.

The impact velocity of the projectile is determined by the gas pressure, the mass of the projectile and the gas gun set-up. A thermodynamic based relationship has been proposed [72], which can control the impact velocity within $\pm 7\%$ of the targeted value.

For the gas gun testing, the manufactured composite plates were cut to approximately 171.45mm x 444mm with an abrasive diamond face saw. The plate was bolted to a rigid testing fixture through two steel bars, as shown in Figure 36c and d to replicate the clamped boundary condition for the fan case in spin testing shown in Figure 32d. The dimensions of the exposed area at impact side of the panel are 279mm x 76.2mm.

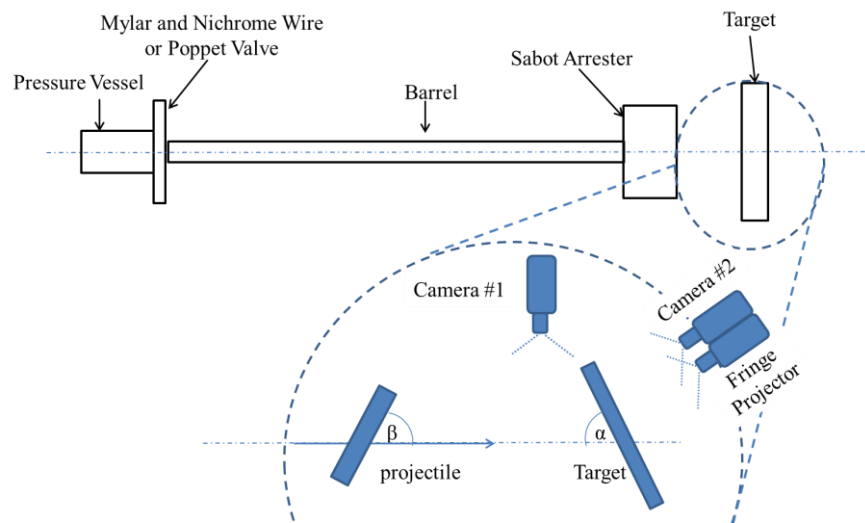


Figure 35 the schematic of a single stage gas gun. Camera #1 phantom V12 for determining the projectile initial velocity and orientation. Camera #2 phantom V7 for determining the projectile residual velocity and the out-of-plane deformation using a projection grating profilometry method.

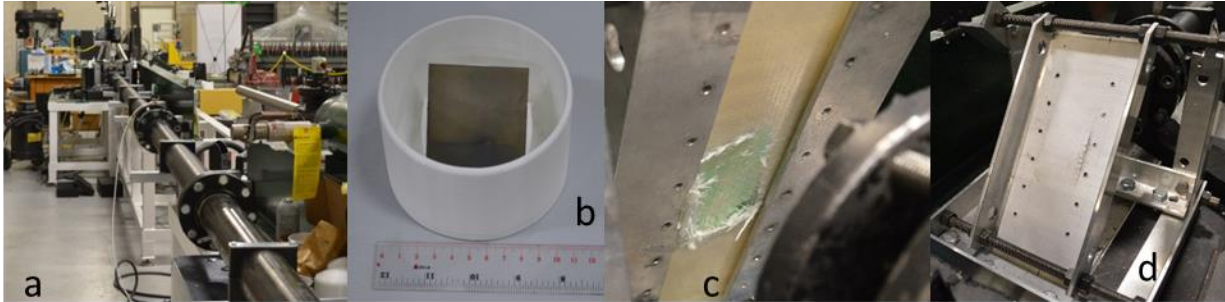


Figure 36 (a) the single stage gas gun. The gun barrel length is 4.7m (15.5 ft) long with an inner diameter of 108mm (4.25 in). (b) The sabot with a titanium blade secured at a 45° orientation. (c) The back side of the composite plate with fringe projection. (d) The impact side of the panel where a 76.2mm (3 in.) wide strip of composite is exposed. The plate is bolted to a testing fixture through two steel bars to replicate the clamped boundary condition for the fan case in Figure 32d.

5.2.3 Manufacturing Composite Panels and Fan Cases

Cylindrical composite cases and flat composite panels were made of S2-glass plain weave fabrics with API SC-15 toughened epoxy resin using the vacuum assisted resin transfer molding (VARTM) method [61], as shown in Figure 37. The glass fabric layers were laid onto a flat tool plate or a cylindrical mandrel to form a laminate with fibers in 0° and 90° orientations. Resin is distributed through the composite layers while under vacuum. It is then vitrified at 60°C for two hours, followed by a post cure at 94°C for four hours with a ramp rate of 1-2°C per minute. The manufactured composite plates had a nominal thickness of 0.62 mm/ply. The thickness of the 6-ply composite plates used in this study is 3.84 ± 0.09 mm, with an average fiber volume fraction using calculation from [73] averaging 53%.

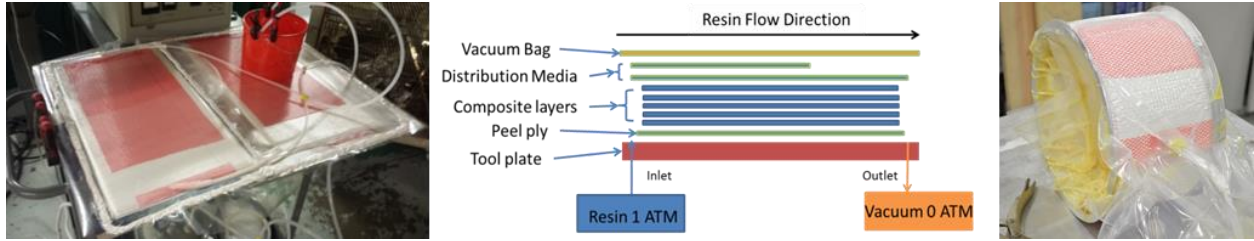


Figure 37 Manufacturing composite articles using VARTM Process. For composite fan cases, Al liner was used as the tool plate.

5.2.4 Out-of-Plane Deformation Measurement

The out-of-plane deformation during spin FBO and gas gun testing was measured with a projection grating profilometry method. The experimental set-up includes a camera, a digital projector, and a computer, as shown schematically in Figure 38. By using the digital projector, only one frame of parallel fringe pattern with cosine function modulated intensity is projected onto the object with an incidence angle. The camera is placed normal to the reference plane, thus the deformed fringe patterns modulated by the surface profile of the object could be captured. After a calibration test, the surface profile can be extracted by calculating the fringe deformation between the reference and the detected surface. The details of the analysis are omitted here.

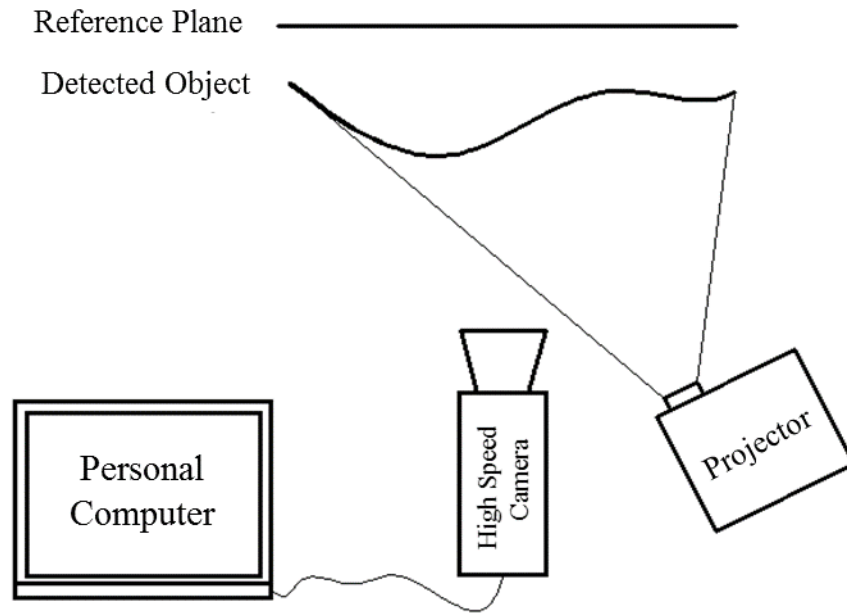


Figure 38 schematic of the projection grating profilometry experimental setup for the out-of-plane deformation measurement.

5.2.5 Damage evaluation by frequency measurements

The natural frequencies of a structure are related to its structural rigidity such that [74]

17

$$f_n \propto \lambda_n \sqrt{\frac{EI}{m}}$$

where λ is a parameter determined by the geometry and boundary condition of the structure, E is the elastic modulus of the material, I is the second moment of inertia, and m is mass.

As a structure becomes damaged, its rigidity decreases, which in turn results in a decrease in the modal natural frequencies. The frequency shift (i.e. the difference in modal frequencies before- and post-damage) is directly proportional to the severity of the damage. This method of damage detection has been investigated by number of researchers [75], [76], [77]. Although the method

cannot differentiate the type and exact location of the damage without a sophisticated model, it can provide a quantitative measure to compare the extent of the damage between tested panels.

The frequency measurement set-up used in this work is shown in The panel was hung using a thin wire to approximate a free boundary condition. The pulse excitation was induced by a tap using a hammer. The modal frequencies were measured with a national instrument (NI) accelerometer SN7890985-01, which was attached to the lower left corner of the panel. The data acquisition was made using an NI DAQ module 9234 and Labview Signal Express. The frequency measurement was performed before and after the test for each panel. Fast Fourier Transform (FFT) analysis of the signal was carried out with MATLAB. The 1st mode (M1) and 2nd mode (M2) frequencies were analyzed, and the damage severity of the panel was assessed according to the shift in modal frequencies.

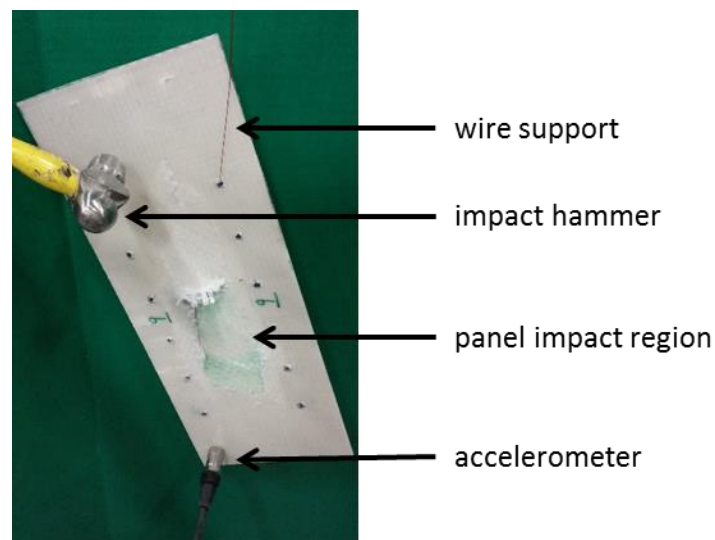


Figure 39 experimental set-up for frequency response measurement.

5.3 Projectile Design for Gas Gun Experiments

5.3.1 Spin pit and gas gun projectile velocity characterization

A fan blade rotating about a fixed axis at a constant angular speed ω has a velocity tangential to its path. At the instance of a FBO event, the conservation of angular momentum dictates that the released blade will rotate about its center of gravity (cg) at ω [78]. At the same time, the blade possesses a translational velocity along the tangential direction. The translational velocity varies in the blade with the radial distance in respect to the fixed axis, as shown in Figure 41. For example, the velocity at its cg is determined by

18

$$v_t = \omega r_g$$

where r_g is the radial distance from the cg of the blade to the fixed axis, and ω is rotational speed in rad/s. Therefore, the kinetic energy of the blade has both the translational component and rotational component

19

$$KE_{tot} = KE_{rot} + KE_{trans}$$

and

20

$$KE_{trans} = \frac{1}{2} m_{blade} v_t^2$$

21

$$KE_{rot} = \frac{1}{2} I \omega^2$$

where I is the moment of inertia of the released blade about its cg. The ratio of the translational energy to the rotational energy depends only on the blade geometry. For the blade used in this study, the KE_{rot} accounts for about 6.5% of the total kinetic energy.

In gas gun testing, the projectile has the translational velocity that is uniform across the blade span. A released blade from spin pit testing will have an additional angular velocity component. If a projectile of similar mass and geometry is fired at a target with a velocity equaling either of that at the cg or at the tip of the released blade in spin test, the impact energies of the two tests will not match, as illustrated in Figure 40.

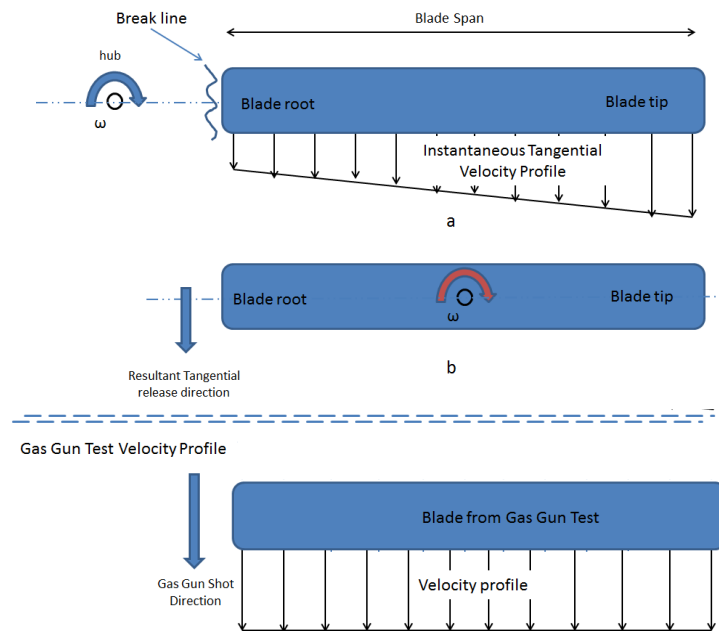


Figure 40 comparison of the velocity profile of a released blade in spin test to that of a projectile in gas gun test.

5.3.2 Projectile/target interactions

The velocity profile also affects the angle at initial impact and subsequent projectile/target interactions. The differential tangential velocity from tip to end in the released blade causes it to

rotate, in addition to that caused by the initial rotational kinetic energy. In comparison, the projectile in gas gun testing tends to travel along a straight path.

The curvature of a fan case may affect the path of the released blade differently from a flat target. To generate similar damage in gas gun experiment, curved panels or inclined flat panels have been used [8]. The current work uses a flat target. The target oblique angle is a parameter in this investigation.

5.3.3 Projectile Design for Flat Panel Gas Gun Testing

To replicate the observed damage on fan cases from FBO testing using flat panel gas gun testing, three projectile designs have been investigated.

5.3.3.1 Method I: blade segment

Method I use a blade segment identical to the released blade in spin testing as the projectile. The impact velocity of the projectile was set to equal to the cg velocity of the fan blade in spin testing. This method provides the baseline for comparison with alternative designs.

5.3.3.2 Method II: energy-based similitude design

Similitude theory allows to scale tests or experiments to a more manageable or simple scenario. It has been explored in impact testing. Ref. [79] reviewed the efforts in scaling projectiles to simulate high velocity impact on plates with low velocity testing. It was concluded that there is no absolute substitute for scaling projectile velocity to match all damages and responses with generic scaling geometry factors. Nevertheless, some other parameters may be scaled. A military standard MIL-P-46593A [80] has been developed for the design and fabrication of fragment simulating projectiles (FSP) in order to simulate the ballistic response of commonly used firearm

ammunitions. Below is a list of parameters required by MIL 46593A to successfully design a FSP:

1. Same material composition
2. Similar hardness
3. Similar weight
4. Similar finish
5. Similar dimensions especially leading edges/nose shape

Following the methodology set by this standard, a projectile design with energy-based similitude is proposed here. This is the Method II. It satisfies MIL 46593A requirements 1, 2, 4 and 5. However, instead of matching the weight, Method II will match the energy profile of the blade span by changing the distributed mass of the projectile along its span.

The principle of energy-based similitude design is illustrated in Figure 42. As discussed previously, the kinetic energy of a released blade is dominated by the translational component, hence only the translational kinetic energy is considered for this method. The wedge shaped blade used in this work, the mass profile decreases while the tangential velocity increases linearly with its span from root to tip. For a small blade segment Δr at a radial distance r with a mass $m_{\delta r}$, its kinetic energy is

22

$$KE_{\delta r} = \frac{1}{2} m_{\delta r} v_r^2$$

Discretizing the blade along its span, the kinetic energy profile is obtained as shown in Figure 41. The resulted energy profile with a unit of J/δ_r is a nonlinear function over the blade span. The total blade kinetic energy would be the area under the curve. It is interesting to note that the

maximum of the kinetic energy is not located at the blade tip, but roughly a third of the blade span away from the tip.

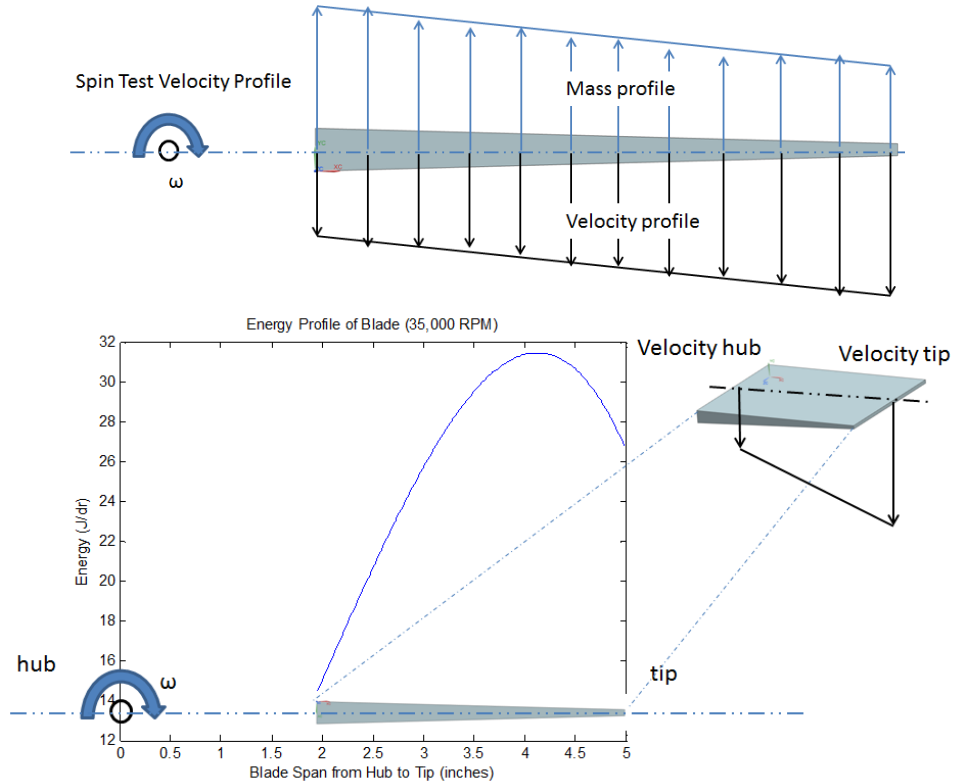


Figure 41 mass, velocity and energy profiles of a wedge shaped blade in spin testing. Longer arrow length corresponds to a larger magnitude.

The energy profile of the blade segment in Figure 41 can be reproduced with a projectile of a constant velocity but a specially designed mass profile. For example, if the projectile will be fired at the tip speed of a released blade, $m_{p\delta_r}$ will be

23

$$m_{p\delta_r} = \frac{(2 * KE_{\delta_r})}{v_{tip}^2}$$

Keeping the width of the projectile b as a constant, the above mass profile can be generated by varying the thickness h_r

$$h_r = \frac{m_p \delta_r}{\delta_r b}$$

The thickness profile of the projectile for energy-based similitude design is shown in Figure 42. This design allows matching the energy profile over the span of a release blade segment using a projectile with a constant velocity. The total mass of the projectile designed this way is approximately 43% of that of the blade segment.

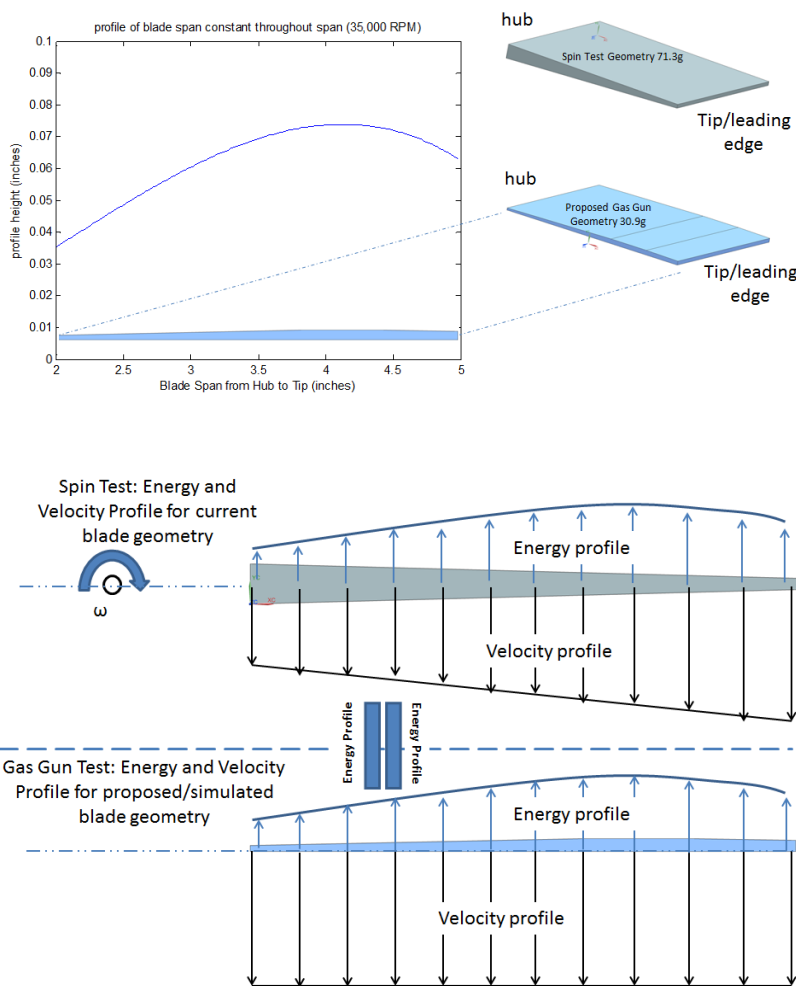


Figure 42 the thickness profile of the projectile for energy-based similitude design

5.3.3.3 Method III: pre-bent projectile

It has been observed that, in FBO testing, the released blade tends to make multiple impacts on the fan case. The initial impact is made by the tip of the released blade. After that, the blade tip plastically deforms and curls over. The blade often lands on the case at its root at the second impact. The damage caused by the second impact can be greater than the first impact. To simulate the damage by the deformed blade, a cylindrical shaped projectile has been used in a previous investigation [8].

In this work, a pre-bent blade segment was used as the projectile. The blade segment was bent into the desired shape using a 3-point bending fixture on a servo-hydraulic Instron testing frame 1321. The amount of bent is calculated by a procedure described below.

After the blade being released, at an instantaneous point in time, the tip of the blade will touch the fan case. At this instance, an inertial reaction force will develop at the root of the blade forcing the blade to rotate about its cg. This scenario can be simplified to a problem as a beam being subjected to 3-point bending shown in Figure 43. The beam has a length equaling the span of the blade segment. Its left and right ends correspond to the root and the tip of the blade. It is subjected to a concentrated load at its cg, which is at a distance of l_a to the root.

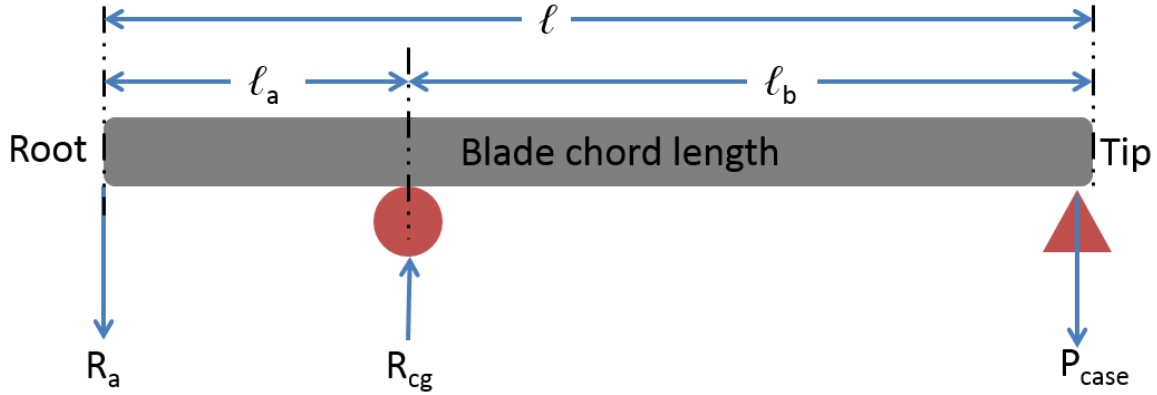


Figure 43 bending of the blade in spin testing can be simplified as a beam being subjected to 3-point bend. The free body diagram is for the instance when the blade tip becomes in contact with the fan case wall. Here, R_{cg} is a reaction force developed at the blade center of gravity cg. ℓ_a is the distance from the blade root or failure point to the blade cg and ℓ_b is the distance from cg to the blade tip.

The free body diagram of the problem is given in Figure 43 and Figure 44. For equilibrium, the sum of the reaction forces R_a , R_{cg} and the force exerted by the fan case P_{case} and their moments must be zero, i.e.

25

$$\sum F = 0 = -R_a + R_{cg} - P_{case}$$

26

$$\sum M_a = 0 = R_{cg}\ell_a - P_{case}(\ell_a + \ell_b) \text{ where } \ell = \ell_a + \ell_b$$

Eqs. 25 and 26 contain three unknown forces. To solve the required force for the pre-bent for a blade released at given rotation speed, an additional condition is needed. In this work, this condition is set through the consideration of energy conservation. It is assumed that the strain energy resulted from bending equals to the rotational energy KE_{rot} of the blade given in Eq.21.

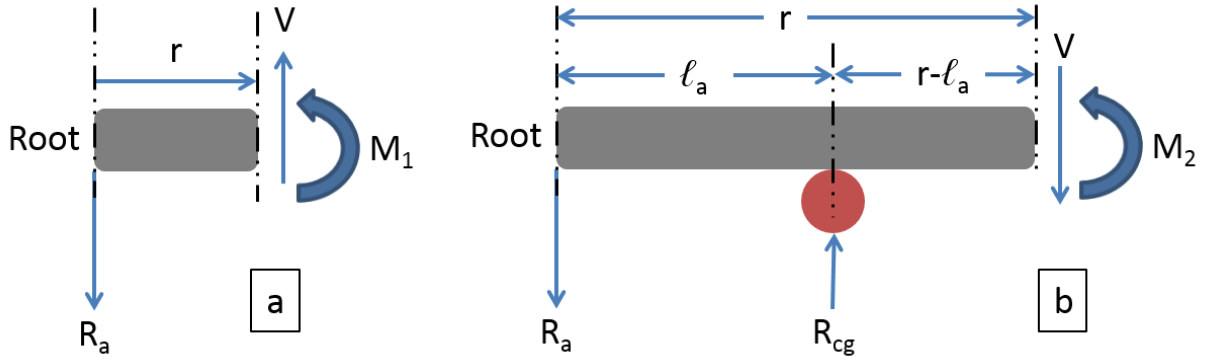


Figure 44 free body diagram of blade geometry along chord length to determine moment equations M_1 from left (a) and M_2 right (b)

For the 3-point bend problem in Figure 44, the strain energy is

27

$$U_{bend} = \int_0^{\ell_a} \frac{M_1^2}{2E_e I_A(r)} dr + \int_{\ell_a}^{\ell} \frac{M_2^2}{2E_e I_A(r)} dr$$

Where,

$$M_1 = P \left(1 - \frac{\ell}{\ell_a}\right) \text{ and } M_2 = P(r - \ell)$$

Therefore,

28

$$U_{bend} = KE_{rot} = \frac{P^2}{2E_e} \left(\int_0^{\ell_a} \frac{\left(1 - \frac{\ell}{\ell_a}\right)^2}{I_A(r)} dr + \int_{\ell_a}^{\ell} \frac{(r - \ell)^2}{I_A(r)} dr \right)$$

Substitute Eq.26 and Eq.28 into Eq.25, P is obtained as

29

$$P = \sqrt{2 E_e KE_{rot} \left(\int_0^{\ell_a} \frac{\left(1 - \frac{\ell}{\ell_a}\right)^2}{I_A(r)} dr + \int_{\ell_a}^{\ell} \frac{(r-\ell)^2}{I_A(r)} dr \right)^{-1}}$$

Table 10 provides an example for the parameters required in this procedure and the obtained reaction forces P , R_{cg} , and R_a . Using the 3pt bending fixture and digital loading head readout on the Instron 1321 shown in Figure 45. The load value of R_{cg} can be monitored during the pre-bending process. For the rotational velocity investigated, only 15% of the bending strain will be utilized for two reasons: (1) to ensure the blade will not fracture during the pre-bending process and (2) accounting for kinetic energy absorbed from damage to the composite panel. Shown in Figure 45 the loading head is reading 15% of R_{cg} which is approximately 12kN. Post loading of the blade there is a 25mm permanent bend in the blade as shown to the right of Figure 45.

Table 10 method III list of variables.

Variables	Description	Value
ℓ_a	root tip to cg of blade (mm)	31.6
ℓ_b	cg of blade to blade tip (mm)	46.1
ℓ	total blade chord length a+b (mm)	77.7
b	axial width of blade (mm)	57.2
t_t	tip blade thickness (mm)	1.6
t_r	root blade thickness (mm)	5.5
$I_A(r)$	area moment of inertia at specified radial distance r (mm ⁴)	$\frac{bt(r)^3}{12}$
ρ	density of Ti blade	4430.0
E_e	Ti modulus of elasticity (Gpa)	113.8
ω	angular velocity (rad/s)	2970.3
KE_{trans}	translational blade energy (J)	2066.6
KE_{rot}	rotational energy of blade at instant of impact (J)	132.0
P_{case}	reaction load from fan case to blade tip kN	32.4
R_a	Reaction load at the root of the fan blade (kN)	47.4
R_{cg}^*	Reaction load at blade cg (kN)*	79.8*

* R_{cg} is the load recorded from the Instron loading head. To avoid blade failure as seen in spin pit test 4 where the blade breaks in two pieces; only 15% of this total load is utilized in pre-bending the blade.

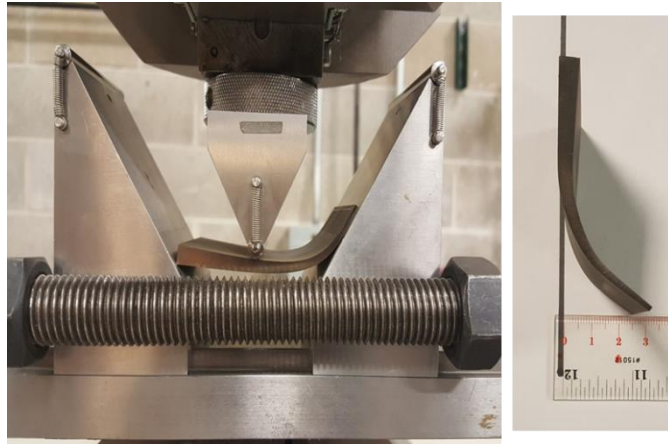


Figure 45 pre-bending a blade using a 3 point fixture on the Instron 1321 testing frame (left) and the finished pre-bent blade (right).

5.4 Results and Discussions

5.4.1 Spin pit testing

FBO tests were performed with five composite fan cases. Table 11 provides a summary for the testing parameters and key characteristics of these tests. In sp_1 and sp_2, the fan cases were tested with the Al liner. In sp_3, the composite was exposed at the impact zone by removing a strip of Al of 3 inch wide from the liner circumference. In these three tests, the fan case was attached to the bearing house by bolting the liner flange. However, cracks were found at the corner of the flange after the tests. In sp_4 and sp_5, the Al liner was removed completely and the composite fan case was clamped directly to the bearing house, as shown in Figure 32d. In the five FBO tests, the blade release occurred in the range of 18,350 to 28,364rpm, corresponding to a tip speed 244 to 377m/s. The blade was contained successfully in all tests.

Figure 46 shows the high speed video footages for sp_2 and sp_4. As seen, the blade makes the first contact with the fan case at its tip, which is followed by bending of the blade. The damage on the fan case begins as a local event. As the blade bent, the area of contact with the fan case increases, delamination and scraping/sliding damages happen next. As the blade scraping the fan

case, it starts to pitch, leading to the second impact on the fan case with its root. This process is more evident in the video footages of sp_2. The schematic of this process is presented in Figure 47. Separated by the blade pitching point, the damage area can be divided into two regions. In Region i, the blade tip impacts and scraps the fan case. In Region ii, the second impact by the blade root takes place. Post-mortem backlighting inspections revealed that the damage on the fan case occurs approximately 40% in Region i and 60% in Region ii.

Table 11 results of spin tests; highlighted is test being matched with gas gun testing

Test #	Fan Case Type	Design Velocity (RPM)	Failure Velocity (RPM)	Tip Velocity (m/s)	cg Velocity (m/s)	Post Impact Notes
sp_1	Aluminum Lined	25000	18350	244	158	Contained with minor initial damage from blade tip. Broken Aluminum liner exposing composite from blade root interaction. Blade bent back to nearly 90°
sp_2	Aluminum Lined	25000	23284	310	200	Contained with minor initial damage from blade tip. Broken Aluminum liner exposing composite from blade root interaction. Blade bent back to nearly 90°
sp_3	Composite exposed and bolted boundary	25000	23643	314	203	Contained with majority damage from blade tip local delamination of at least one layer is visible on the inner side of case. Outer layers are bulged but intact
sp_4	Composite exposed and clamped boundary	30000	28364	377	244	Contained with initial contact layer completely delaminated and sheared along the edges of the blade. Fibers remain attached to the fan case. Blade fractured at 1/3 distance away from the blade tip.
sp_5	Composite exposed and clamped boundary	32500	25254	336	217	Contained. Inner housing bolt failure resulting in bolt fragmentation damage on entire fan case circumference. Scraping and initial layer delamination from blade tip and indentation with fiber cutting from blade root

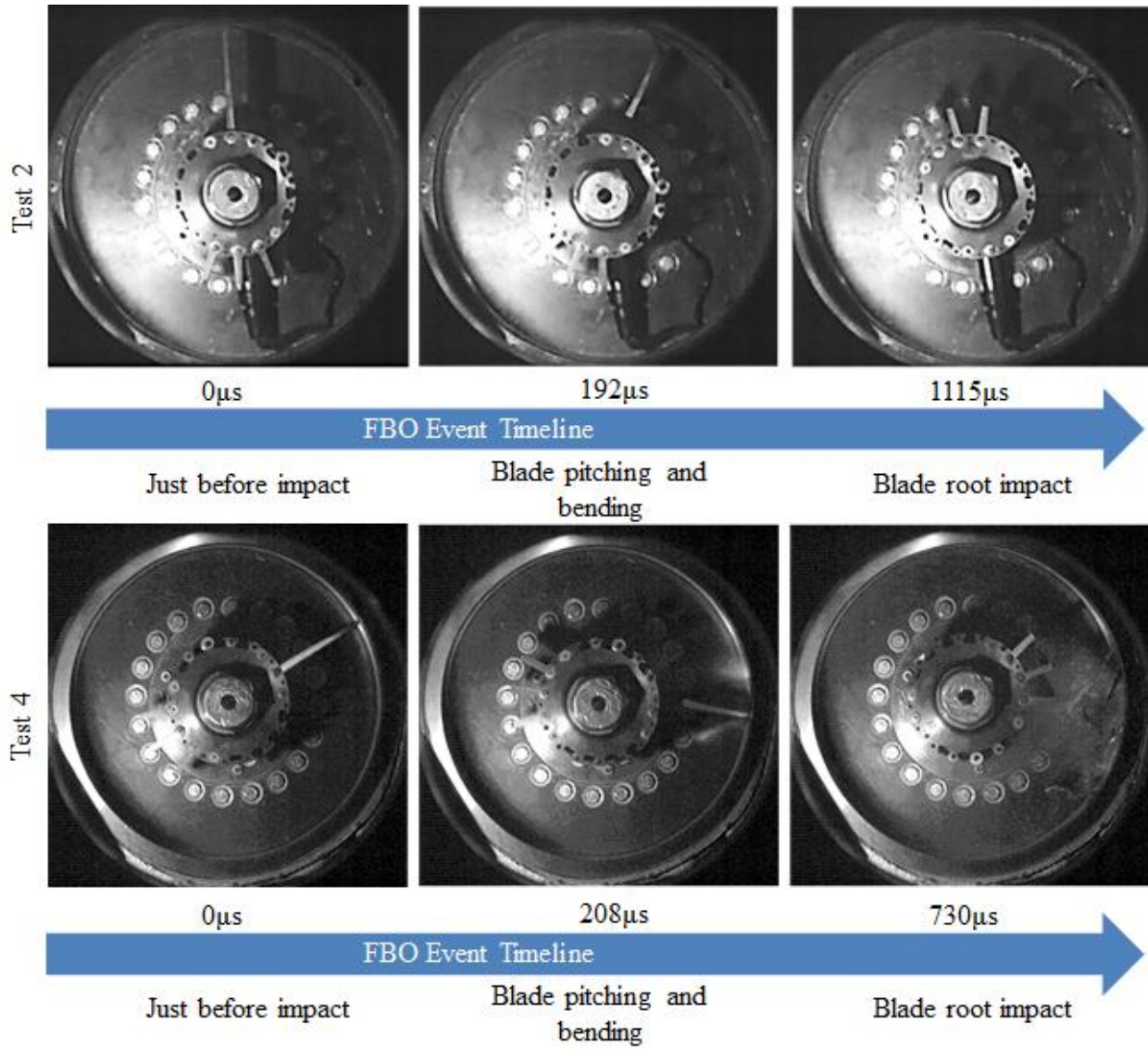


Figure 46 high speed images of FBO spin test of sp_2 and sp_4. The rotor rotates clockwise.

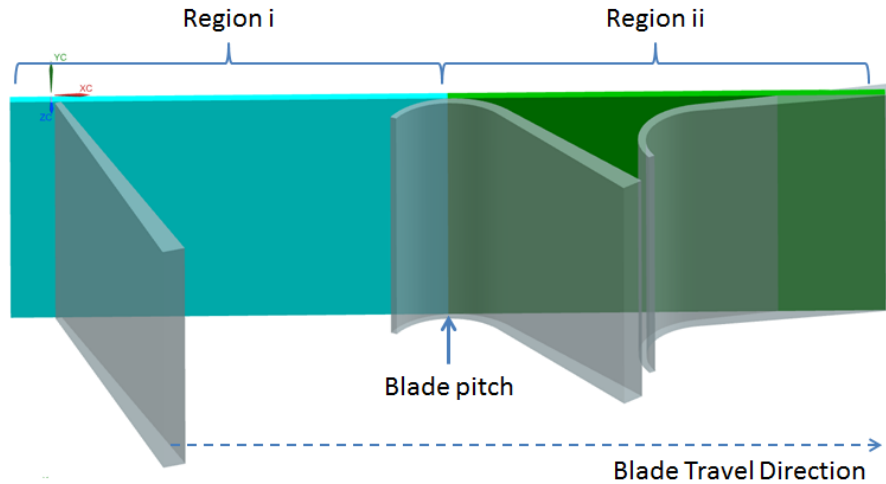


Figure 47 the schematic shows the initial contact of the blade with the fan case and the subsequent deformation and motion of the blade observed in FBO spin test. This results in two damage regions on the fan case separated by the pitching point of the blade.

5.4.2 Gas Gun experiments

Table 12 summarizes all conducted gas gun experiments. A total of ten experiments were performed with the three methods described in projectile design for flat panel gas gun testing. The oblique angle of the target α was also investigated. The flat panels were tested at $\alpha=34^\circ$, 45° and 55° . With the exception of test 5, the projectile was placed at $\beta=45^\circ$ in all tests. As a result, the angle between the tip of the projectile and the panel was at 79° , 90° and 100° , respectively. The other parameters listed are the mass and velocity of the projectile and mass of the sabot. In three experiments, the projectile perforated the panel and the measured residual velocity is reported. Table 12 also provides the frequency shifts for the 1st and 2nd modes obtained by the frequency measurement described in the damage evaluation section.

Table 12 Summary of the gas gun testing with flat panel

Test	Method	Pressure (psi)	Target Orient.	Proj Orient.	Mass Proj (g)	Mass Sabot (g)	V _i (m/s)	V _r (m/s)	FFT node evaluation		damage severity
									M1 Diff (Hz)	M2 Diff (Hz)	
1	I	40	45	45	72.1	107.9	247	48	9.37	12.5	8
2	II	70	45	45	28.09	104.3	377	99	7.03	14	7
3	I	39	45	45	71	104.8	220	-	2.35	25.8	4
4	II	71	34	45	29.6	105.2	290	116	1.57	11	3
5	II	70	34	30	28.75	105.15	329	-	9.37	18	8
6	I	45	34	45	71.5	105.5	260	-	3.12		5
7	III	45	34	45	71.5	117.5	233	-	5.47	10.9	6
8	III	45	45	45	71	105.7	240	-	0	37.5	1
9	III	45	45	45	71	104.23	232	-	2.35	14.8	4
10	III	50	55	45	72.4	106.2	238	-	0.79		2

The frequency shift in the 1st mode, M1, appears to correlate better with the damage severity determined by visual inspection with backlighting. Hence the damage severity was quantified with a numerical value of 1 to 8 for each tested panel according to its M1 value. The averaged damage severity number was 5.66, 6.00, and 3.25 for panels tested with Method I, II and III, respectively. Judging from the damage severity number, Method I & II cause more severe damage than Method III.

Good quality high speed images of the gas gun experiments are available for Method I test 3 and Method II test 4, shown in Figure 48 and Figure 49, respectively. In other experiments, the debris from the disintegrated sabot partially blocked the camera views and good quality high speed images are not available for Method III.

The four images in Figure 48 (Method I test 3) present a complete process of projectile/panel interaction from the moment of the projectile tip striking the panel, bending of the projectile, to sliding on its back along the target plate. The process is somewhat similar to that seen in FBO in spin testing. Method II, however, produced a different effect. As shown in Figure 49, the projectile pierces through the target panel with little bending.

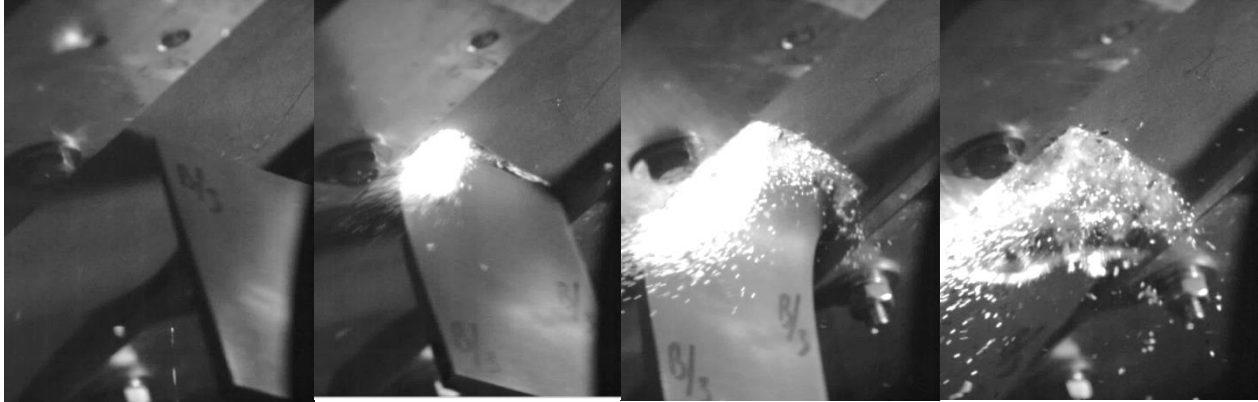


Figure 48 high speed images of the gas gun experiment with Method I, Test 3. From left to right: blade before impact ($0\mu\text{s}$), tip impact ($115\mu\text{s}$), blade bending ($346\mu\text{s}$), and scraping ($653\mu\text{s}$). As seen, the blade tip strikes the panel, bends, and slides

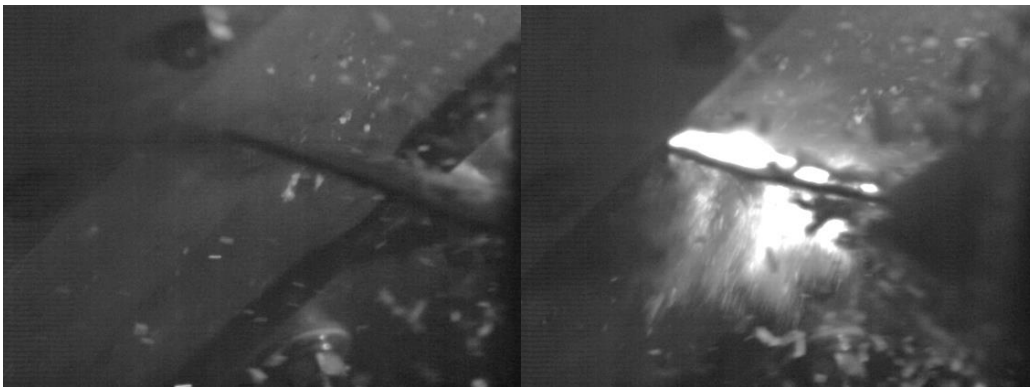


Figure 49 high speed images of the gas gun experiment, Method II, Test 4. The blade tip strikes the panel and goes straight through ($154\mu\text{s}$ after the left image).

5.4.3 Comparison of gas gun and spin tests

The efficacy of the flat panel gas gun experiment is evaluated by comparing deformed projectiles and damages on the composite with those from spin test. The tested projectiles are compared with the released blades in Figure 50. The images of flat panels under backlighting are compared with that of the fan case tested in sp_4 in Figure 51.

In Method II projectiles were deformed in a manner that was not observed in spin pit testing. The damages on the composite panels are much localized than that on the fan case. The results indicate that a projectile with a modified cross sectional shape, although having a similar energy

profile as the released blade, may not lead to a similar deformation mode. A correct deformation mode of the projectile appears to be more critical in producing similar damage modes on the target.

For Method I, the results were inconsistent. The projectile from test 3 had a bent shape similar to a FBO blade. However, the projectiles from tests 1 and 6 only bent slightly. In test 1, the panel was perforated although the experiment was designed to simulate spin test sp_4 in which the blade was contained. A close inspection reveals that the failure was initiated by the interaction of the sharp edge of the projectile with the target panel. To reduce this effect, the panel inclination angle α was reduced to 34° in test 6. This change reduced the amount of tip damage to the panel. However, the projectile speed in test 6 was slightly over the target speed. The tip perforated the panel causing the projectile to pitch such that its root impacted the panel. There was no scraping or interaction by the mid-section of the projectile, leaving an un-damaged area between the tip and projectile root sections. These results suggest, when the projectile and the target are properly inclined and oriented, a blade segment projectile fired by a gas gun may produce damage modes on a flat panel somewhat close to that on a fan case in FBO. However, it is difficult to control the exact orientation of the projectile at the time of impact in a gas gun experiment. A small variation can lead to different interactions between the projectile and composite panel and inconstant results.

Method III uses a pre-bent blade as the projectile. This eliminates the possibility of perforation by the sharp tip. Compared with two other methods, the damage severity in Table 12 caused by Method III in general is lower, and the damage revealed by backlighting in Figure 51 spreads over a longer area. The result resembles the damages on the fan case.

The Method III was investigated further by varying the oblique angle α . It was observed that a low angle of $\alpha=34^\circ$ (test 7) resulted in a very long scraping damage in Region i and a sudden impact at Region ii. The second impact caused the formation of a small hole, as very little kinetic energy was absorbed by the panel in Region i. The energy absorbed by Region i and Region ii can be regulated by varying α . Increasing α from 34° to 45° in tests 8 and 9 eliminated the penetration by the projectile root, however, it resulted in a very long delamination in Region ii. The backlighting image indicates that the damages by the tip and mid-section of the blade in Region i count for about 30% of the total damage whereas the rest of 70% occurred in Region ii. With $\alpha=55^\circ$, test 10 resulted in a damage distribution of 40% in Region i and 60% in Region ii. In Region I, the main damages observed on the tested panel were broken fibers at the top layer at the initial contact point by the blade tip and delamination throughout the region. In Region ii, the layers were sheared through by the impact from the blade root. At the back side of the panel, minor tensile failures occurred along a boundary corresponding to the shape of a blade segment. These failure modes were similar to the damages observed on the fan case in sp_4.

Figure 52 compares the out-of-plane displacement history during impact at Region I for the four Method III experiments. This measurement was made at the back side of the panel with the projection grating profilometry described in 2.4. The results are only available for the first $500\mu\text{s}$ before the debris from the panel blocked the camera view. It is interesting to note that the displacement for the panel with $\alpha=55^\circ$ is almost two times of the panels with $\alpha=34^\circ$ and 45° over the time span, indicating a much larger amount of kinetic energy have been transferred to the panel. Judging from the damage distribution and displacement response, the experiment with $\alpha=55^\circ$ provides the best replica to the spin test.

In summary, the flat panel gas gun experiments may be used to investigate the design of fan case against FBO. To generate similar damage modes, it is critical to ensure the deformation of the projectile used in gas gun is similar to that of a released blade.

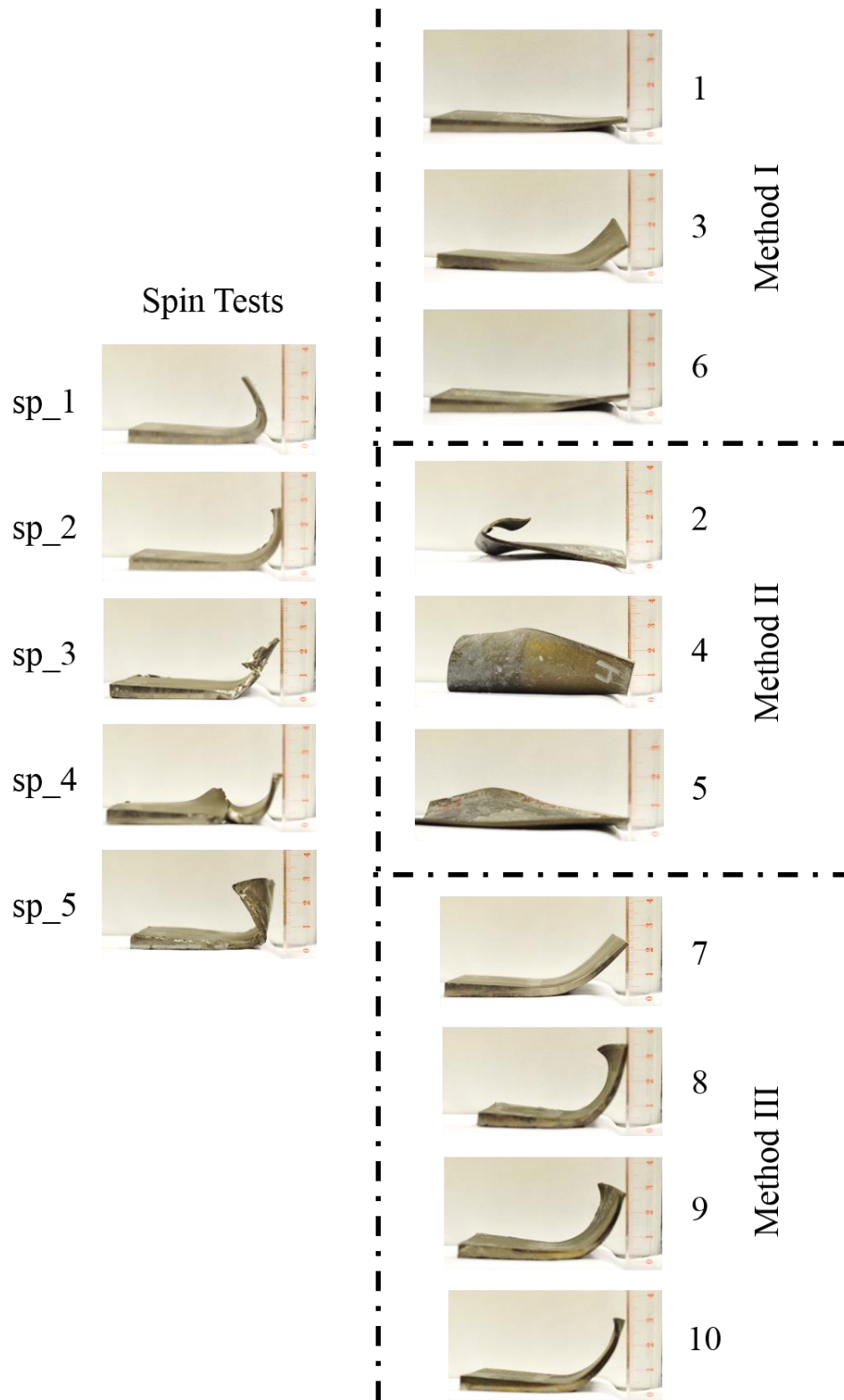


Figure 50 comparison of deformed projectiles. Left: released blades from spin tests. Right: projectiles tested in gas gun experiments. The scale shown is in centimeter.

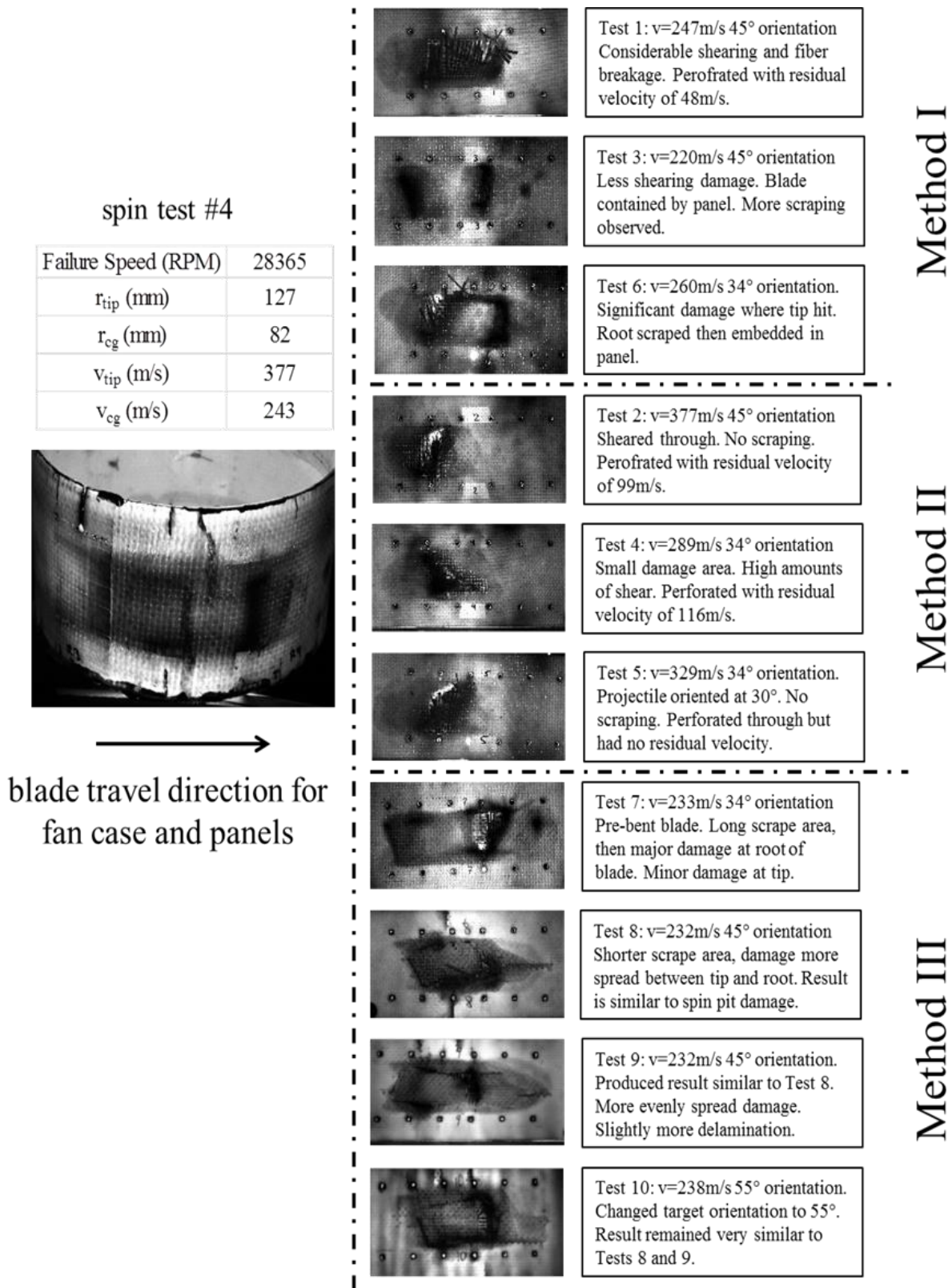


Figure 51 comparison of damage. Left: spin testing sp_4. Right: panels after gas gun experiments. Darker regions represent more severe damage.

Blade Tip Panel Displacement Comparison

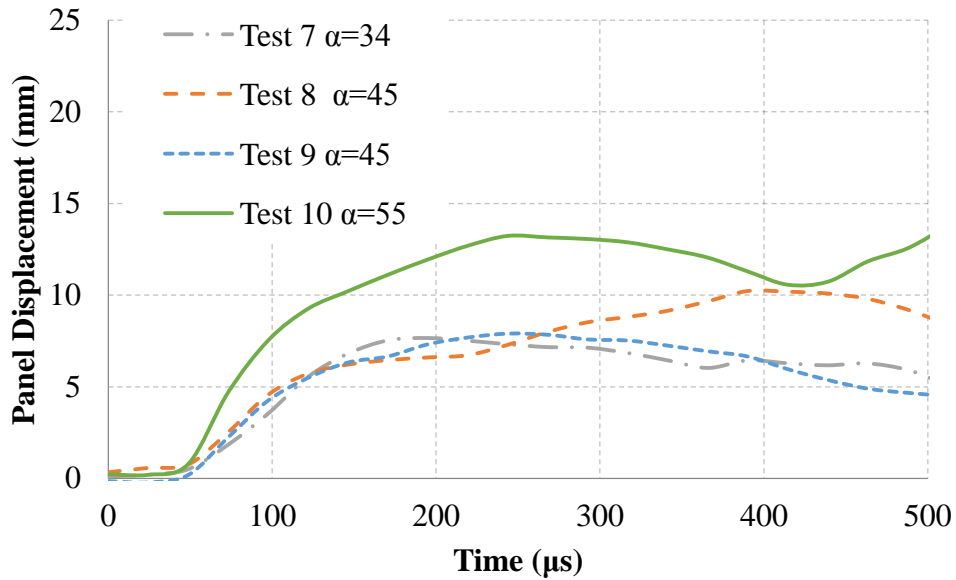


Figure 52 the out of plane deformation of the panels tested with Method III.

5.5 Conclusion

The hypothesis that flat panel gas gun experiments may produce similar results to substitute spin pit FBO testing have been investigated. Three different projectile design methods were developed and evaluated. The results show that, to produce similar damages on flat panels in gas gun experiments, it is critical to ensure the deformation of the projectile is similar to that of a released blade in a FBO test.

Among the three projectile designs, Method III results show damages similar to that of FBO testing. Method III uses a pre-bent projectile. Along with projectile design, the flat panel oblique angle α and projectile orientation also affected the results. The gas gun testing methods presented here provide a cost effective means for accurate pre-screening of composite fan case materials and designs.

CHAPTER 6 CONCLUSION

6.1 Concluding Remarks

The major developments during the course of this work are summarized in Chapter 3, 4, and 5.

Chapter 3 presents a unique, smaller scale fan-blade-out testing method. This method provides a cost effective way to test data acquisition systems and develop/prove an experimental setup before major investments are dedicated to a full scale rig setup. The small scale test can provide insight on how actual full scale size systems may respond during a FBO. This work is published and can be found in reference [71].

Chapter 4 presents the development of a single stage gas gun and the testing methodology. For data acquisition, quantitative measurements of force and displacement were attempted. The force and deflection measurements were successful for tests conducted below the ballistic limit. To estimate the required gas pressure for a targeted velocity, a thermodynamic based relationship was proposed. The predicted velocity with this relation was within 7%. Gas gun impact experiment was performed on S2/SC15 epoxy composite panels following a test method under development for ASTM. The method is aimed at determining the major failure modes and evaluating the overall impact performance of the target materials. With fixed boundary conditions and a simple projectile shape, this experimental setup is also ideal to be used for validating numerical models.

In Chapter 4, a new parameter E_{BL} , the projectile kinetic energy at the target ballistic limit normalized by the contact area of the projectile, is proposed to compare the ballistic impact resistance for a wide range of materials tested with blunt projectiles of different shapes. By plotting E_{BL} versus the areal weight of the target, the ballistic protection capability of different materials can be compared in a specific sense. Surprisingly, S2 glass composite is highly

efficient in weight in terms of ballistic protection. It shows promise as an excellent candidate for aero-engines containment.

Chapter 5, the heart of the dissertation, provides experimental evidences on the feasibility of replicating the initial FBO damage on fan case with a gas gun flat panel impact testing. Compared with the actual FBO test data from a spin pit, it was proven that, by using a pre-bending fan blade as the projectile, a gas gun can replicate the initial damages observed on a fan case with flat panel testing.

6.2 Contributions

This thesis made the following contributions in the following three aspects

1. Testing facility and method development
 - i. A high speed spin pit testing facility and its data acquisition system have been developed
 - ii. A testing procedure for FBO has been established.
 - iii. A gas gun testing facility and its data acquisition system have been developed.
2. Analysis
 - i. A new, energy based design for the projectile and critical testing parameters in the gas gun based testing for FBO investigation has been proposed.
 - ii. A thermodynamic based relationship between the required gas pressure and the targeted velocity has been proposed and validated.
 - iii. A new parameter E_{BL} , the projectile kinetic energy at the target ballistic limit normalized by the contact area of the projectile, is proposed.

3. Fan case design methodology

- i. An experimental method to investigate the initial damage on a fan case in FBO using gas gun test has been developed. The results show that with pre-bent blade as projectile, the gas gun flat panel impact test can be used in the design of fan case.

6.3 Future work

6.3.1 Testing of additional material systems

The developed gas gun testing methods based on fan case spin pit testing can be used in other material systems such as carbon fiber composites and metal fan cases. The method should be tested for additional material systems.

6.3.2 Blade-to-blade interaction investigation

Constructing aero-engine fan cases out of composite materials is vital for the light-weighting of this heavy engine component. Directly leading to fuel cost savings and increased aircraft range and payload. This provides a high demand for the advancement and familiarity of using composite materials. To help increase the familiarity and feasibility of using composites, other FBO testing focusing on the blade to blade interactions related to the effect of blade aspect ratio should be investigated. As seen from small scale testing in Chapter 3, a secondary kick from a trailing blade can yield significant damage to a fan case. The aero-dynamic gas load on the blade could have an effect on the dynamics of the fan blade out event and should be investigated.

6.3.3 Optimizing thickness for maximum energy absorption with strain energy assumptions

Additionally, further refinement of a fan case design by the optimization of composite thickness with respect to the ballistic limit could result in further weight reduction. The hypothesis to be

tested is that an optimum thickness exist were maximum amount of energy is absorbed by a composite material by the activation of multiple failure modes. As shown by work completed by [81], for lower velocity impacting, a thickness of 2mm damage was produced on both the front and back of the composite materials. With higher impact velocities, a thin composite layer with small space between each layer would more efficiently absorb impact energy per unit areal weight allowing for lighter weight fan case designs. Preliminary feasibility work could start with looking at strain energy bending and shear equations.

APPENDICES

Appendix A: Gas gun operation manual

A.1 Limits

Considering utilizing 3 layers of Mylar (0.010" thickness max pressure and velocity are listed below. Further pressure increase is possible with greater Mylar thickness, however it may prove to be more efficient to increase the volume of the pressure vessel and increase barrel length. This will allow for faster velocity speeds and decreasing of pressure vessel pressure. For this pressure vessel the max pressure used should not exceed 210 psig where max velocity produced with a 180g projectile would be approximately 1400ft/s.

A.2 The gas gun setup

i. instrumented target

Instrumented Target: Transient loading conditions during test are recorded with the target shown in Figure 53 and Figure 56

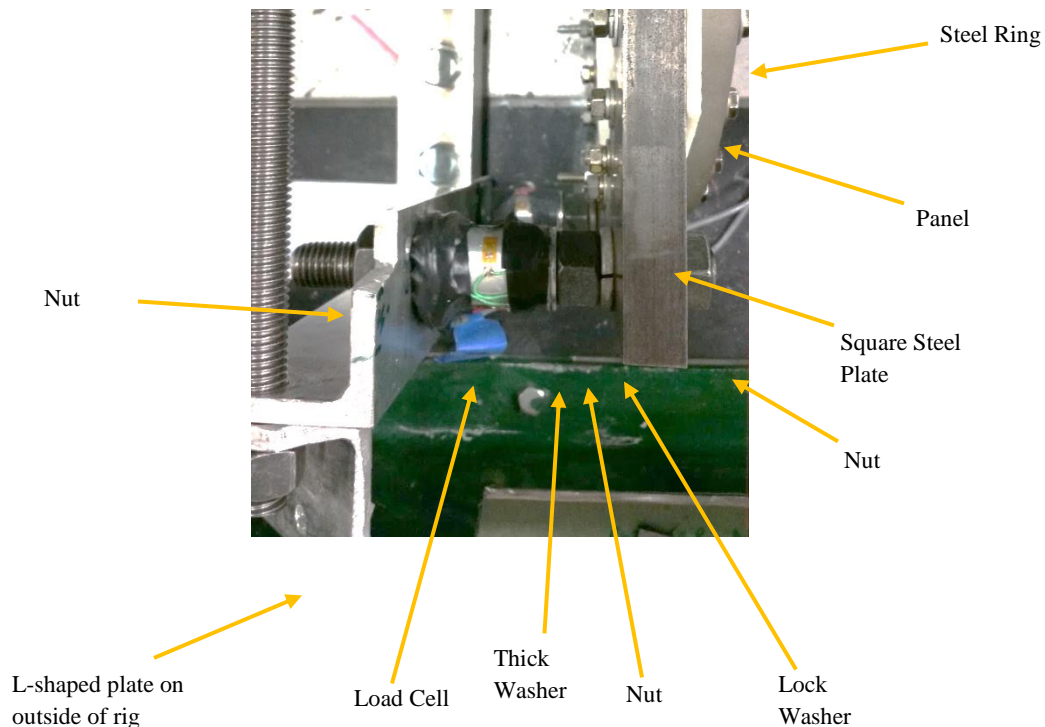


Figure 53 instrumented target loadcell callout

ii. fan blade out replication via gas gun testing

- Installed angle-bars to rig base
- Fit the panel over the holes on the angle-bars
- *Ensure that the panel is centered with the gun barrel, then tighten L-bar nuts*
- Place metal support bars on back of panel, and screw in Figure 54

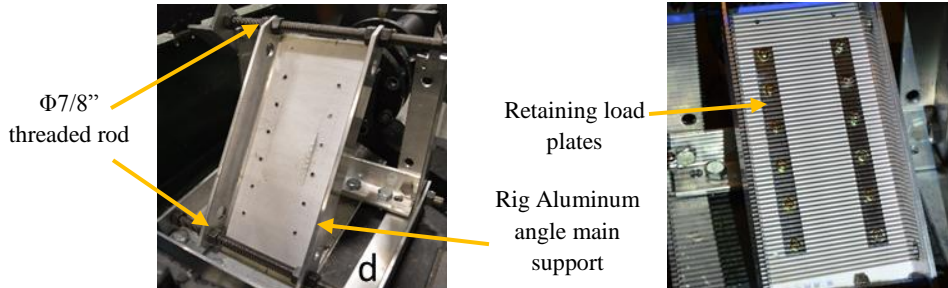
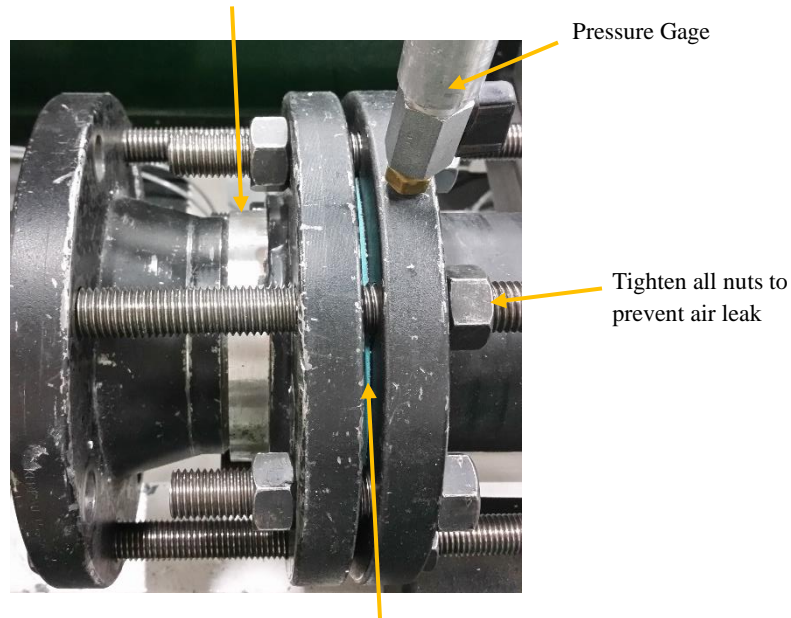


Figure 54 flat panel rig setup where threaded rod allows for adjustment of exposed composite area to blade on front face (shown in figure is back face).

2. Insert one piece of the thin Mylar in the front of the gun exit by the pressure gage Figure 55
 - *Mylar must not have any major scratches or damage
 - Tighten all nuts at the tip of the gun to ensure no leaking and retain sabot arrester

Use aluminum sabot arrester for $\Phi 38.1$ mm projectiles only



Insert thin Mylar between blue foam pads

Figure 55 sabot arrester and positioning of 0.005" thick Mylar sheet to retain vacuum in barrel. This Mylar sheet is shot through.

3. Install the panel with the smooth side facing the gun (Or stay consistent with testing group conducted) torque to 1/4-20 bolts to 11ft-lbs
 - Take note of panel position with labeling

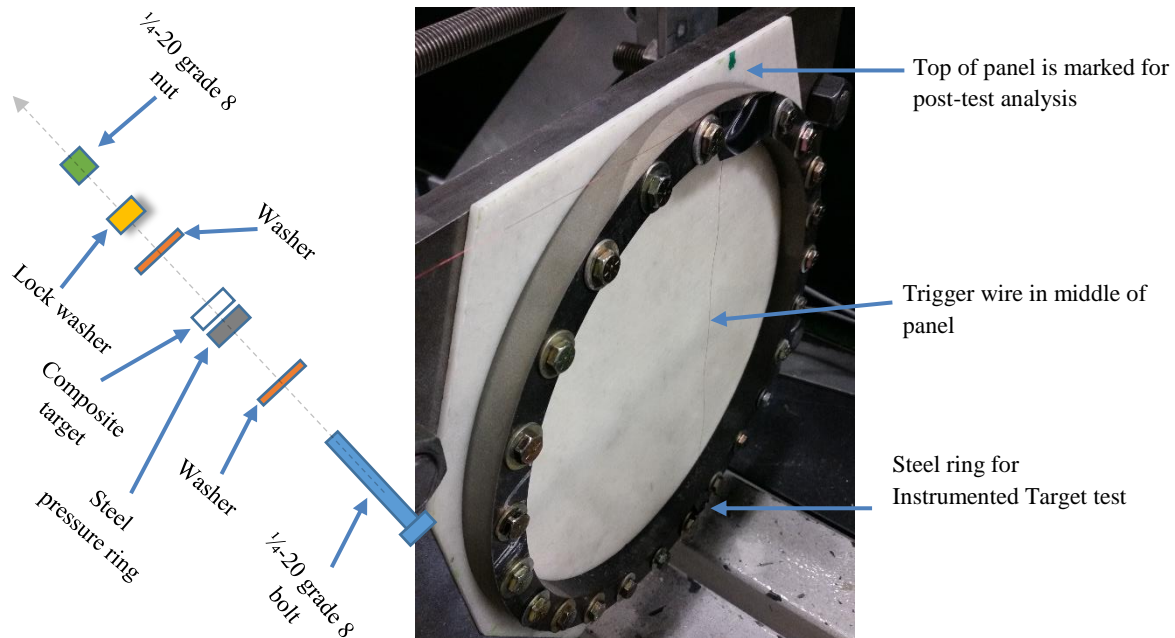


Figure 56 bolting hardware sequence shown to the left torqued to 11 ft-lbf. Target installation and trigger wire setup (right). The trigger wire starts data acquisition and synchronizes high speed cameras.

4. Set up the trigger wire to run from the top of the panel to the bottom of the support
 - Ensure that the wire is taut. Use electrical tape or other means to keep it in place
 - Solder the ends to the trigger box wires
5. Place a light source on the front side of the panel to illuminate the projectile path for velocity measuring with the high speed camera Figure 57

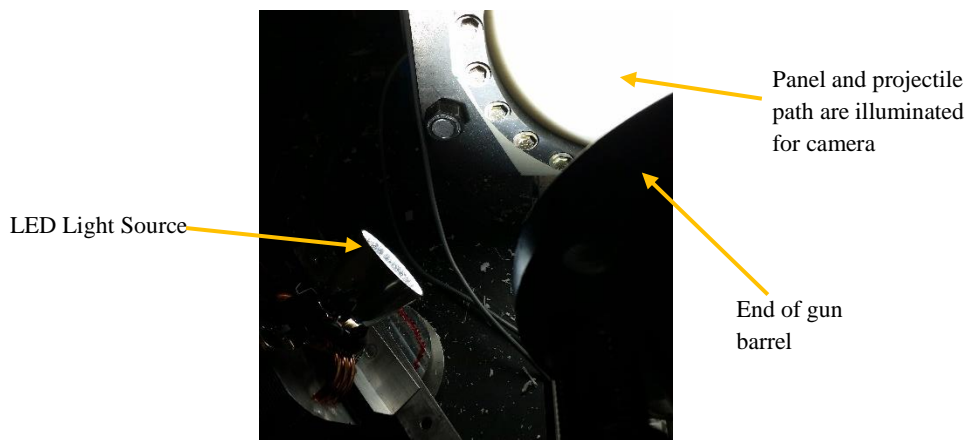


Figure 57 LED light source placement for initial projectile velocity measurement

6. Camera Setup

a) Initial velocity measuring:

*Recommended: use a tape measure coming out the barrel of the gun in the path of the projectile and take a photo using the camera. This ensures the correct resolution and focus is utilized, as well as providing a means of accurate measurement for post-test analysis using the PCC 2.7 camera software shown in Figure 58. The software will create a calibration factor of distance/pixel based on Figure 58 left. Together with the camera frame rate and the calibration factor the projectile velocity can easily be determined as shown in the below Eq.

$$\frac{\text{pixels} \times \text{calibration factor}}{\text{Total frames} \times \left(\frac{1}{\text{camera frame rate}} \right)} = \text{projectile velocity}$$

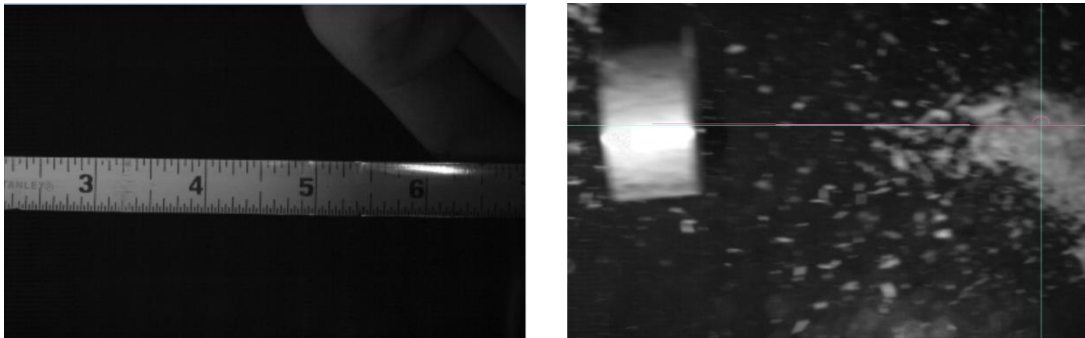


Figure 58 calibration image (left) and projectile image processing example image (right)

7. Determine total mass of sabot and blade

- With the total mass to calculate pressure required to get to target velocity using Eq. at bottom of Figure 17

8. Label the projectile with the test number, the leading edge and trailing faces

- Place the projectile in the sabot, using glue if needed to ensure a tight fit (Figure 59)



Figure 59 sabot with Ti blade shaped projectile (left) and another sabot with Al cylindrical projectile for instrumented target testing (right)

9. For pressures 30-150 psig use 2-0.010" thick Mylar and for 150-210 psig 3-0.010" thick Mylar sheets and position $\Phi 0.013$ " Nichrome wire Figure 60 to make the poppet valve. It is activated with 110V AC.



Figure 60 in-house manufactured poppet valve with Nichrome wire taped with same diameter as ID of barrel

10. Test the trigger on both cameras to make sure the wire is connected correctly before the test
11. Activate the vacuum until gun is cleared
12. Fill pressure vessel to desired pressure

Always ensure that the area is clear before firing. Everyone in the lab should be notified before a test. Doors should be locked. Earplugs and Safety Goggles should be worn

8. Connect the Nichrome wires to the open circuit 110V AC cables Figure 61
- Ensure that the Nichrome does not touch the rig
 - Close circuit to fire test

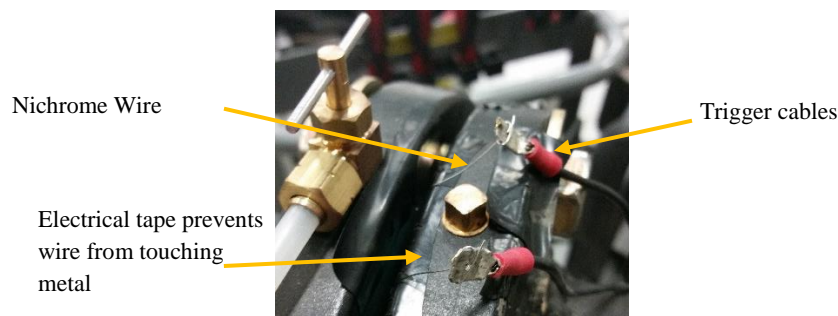


Figure 61 trigger wire connection

iii. GAS GUN PRE-FIRE CHECKLIST

- Sabot barrel contact surface oiled and oriented in barrel
- Pressure vessel and barrel flange bolts (x8) torqued to ≥ 90
- All nuts are fastened securely (gun barrel, poppet valve, panel)
- Trigger wire is taut, soldered, and works correctly for both cameras
- Both cameras have a calibration image for projectile's flight path

- Gun barrel has been vacuumed
- Poppet valve and pressure gage have been closed before turning off vacuum
- Trigger cables have been attached to Nichrome wire at poppet valve

iv. GAS GUN POST-FIRE CHECKLIST

- Unplug gun trigger power
- Allow some time for dust to settle
- Turn off any high intensity light sources (LED or Projectors)
- Save and document data for high speed cameras
- Save and document transducer data (strain gages, loadcells, accelerometers, etc.)

Appendix B: Spin pit user manual and technical notes

B.1 Overview:

The Rotational Impacting Projectile (RIP) test cell provides the ability to test objects at high rotational speed inside of a ballistic vacuum chamber. The test cell is designed to simulate fan blade out events on a 15 to 28 inch fan case. The air turbine powering the rotational motion has a maximum speed of 40,000 RPM through a 0.5627" shaft. The vacuum chamber is outfitted with 9 view ports, 8 of which were incorporated for 360 degree Digital Image Correlation, and the last provides an aft looking forward view from the bottom of the vacuum chamber. The major equipment required to perform a test includes, a 375 CFM air compressor, 20 PSIG oil pump, 18 CFM vacuum pump, and dry shop air at 90 PSI.

The air turbine is controlled by a TC4 controller from Barbour Stockwell Incorporated and has associated software SpinIV from Barbour Stockwell Inc. The SpinIV software and TC4 controller are capable of a variety of testing applications, in this synopsis only constant speed testing will be discussed, please refer to the TC4/SpinIV manuals for reference. The Digital Inputs, used for Faults, allow the entire blade off event testing to run with the click of one button.

The fan blade out test is a destructive test. It is key to maintain a strong understanding of all the components incorporated into the testing procedure to ensure only the engineered failure components fail to protect expensive assembly components. A successful test results in a large unbalance load at a high speed. It is important to isolate the turbine from this unbalance so that no damage is incurred. The damage from the unbalance load requires the operator to replace the Lower Bearing House bearings, and then balance lower bearing house shaft before every test. This adds time and complexity to the testing, but is unavoidable.

B.2 Lower bearing house:

The Lower bearing house (LBH), sits underneath the turbine and is designed to spin fan blades. The LBH shaft can support up to 16 fan blades, although only 1 is used for the fan blade off testing. The LBH is rebuilt between every test. This section will provide a brief walk through of the rebuild along with lessons learned that may be useful for a new design. The current LBH was outfitted for thermocouple and vibration measurement at the two bearings. It was determined for this particular test that thermocouple data was not required because the bearings did not heat up during the short span of time that a test runs, and a test would not be stopped if the bearings did heat up. Figure 62 below shows the inner bearing housing.



Figure 62 assembled inner bearing housing mocked up for temperature monitoring of forward and aft bearing

i. Lower bearing housing re-build instructions

The rebuild instruction will begin with the bare shaft, Figure 63.



Figure 63 lower bearing housing main shaft

Place the forward bearing onto the shaft followed by the compression tube. It is helpful to use the bearing spacer to push the first bearing into place. Do not press the spacer down with much force after the bearing has met its shoulder, Figure 64.



Figure 64 compression tube and forward bearing installation

Next insert O-rings into the bearing retainer and install the aft bearing carrier and align the woodruff key slot, Figure 77. The Viton O-rings are positioned (forward and aft bearing landings) to allow for approximately 0.007" inch of radial clearance. This is considered a soft bearing mount and helps to reduce the load on the shaft and bearing housing structure during a released blade when unbalance load is at a maximum.



Figure 65 aft bearing carrier installation

Install O-rings into the forward bearing landing in the LBH housing, Figure 66.

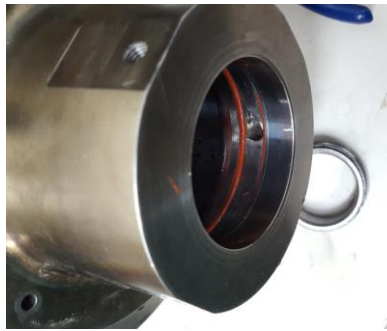


Figure 66 forward bearing carrier O-ring installation

Insert the shaft assembly into the inner housing and install the woodruff key. A custom table inside the test cell is used for this installation process, it is not a necessity, but it provides ease. Next press the shaft into the lower housing, Figure 67 a&b.

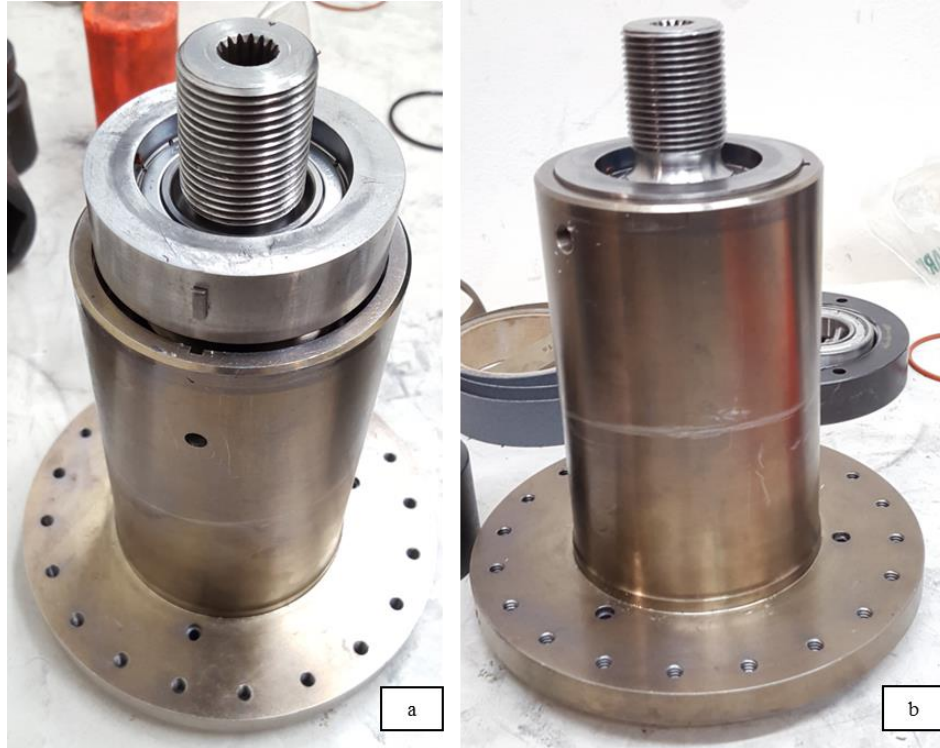


Figure 67 rotating assembly installation into the inner bearing housing. Before pressing in the aft bearing carrier (a) and after seating the aft bearing carrier with woodruff key lined up with slot (b)

Finally install and torque the aft nut to hold the inner raceway of the forward and aft bearings from slipping. Then install the hub assembly, it has dovetail features for easy insertion of fan blades, they are retained axially by #4 bolts and washers. The hub is secured in place with a center bolt. It is drilled in the center to lower the torque required get an acceptable amount of bolt pre-stretch. Here the target torque is approximately 250 ft-lbf. This can be accomplished with an impact gun. A finished rotating assembly is shown in Figure 68.

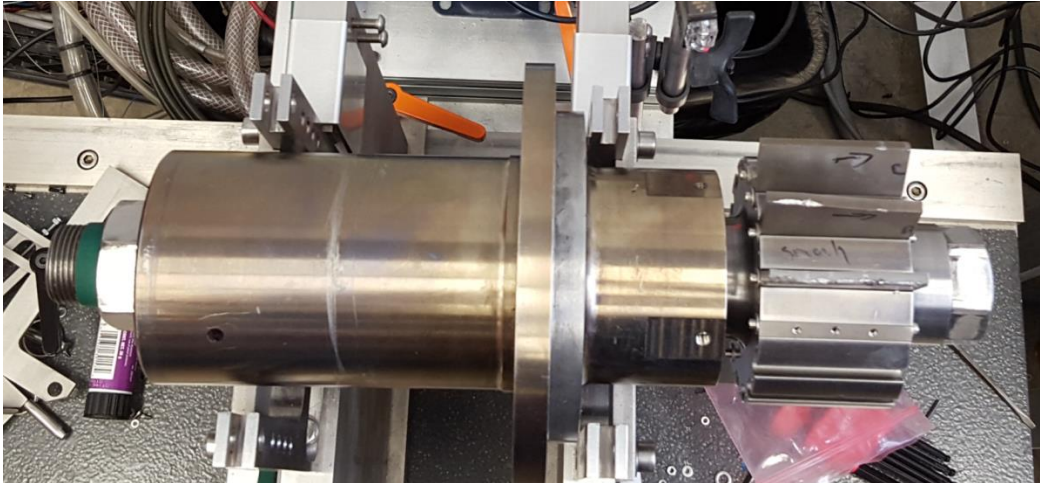


Figure 68 finished rotating assembly with forward bolt and aft retaining bolt
At this point the LBH shaft is ready to be balanced. EasyBalance 2.2 is used for balancing located in the Turbomachinery Lab at the Engineering Building.

ii. Balancing

After balancing the inner bearing house, the remaining assembly includes installing the bearing spring to apply constant pressure on the upper bearing, and bolting the inner housing to the outer housing. The spring puts a cross load across the bearings to reduce ball slip and keep the bearings cool during operation. It was determined that minor adjustments are made to the preload and a check and feel method by hand gives best results. The rotating shaft should seem to rotate with a minor resistance. It should take approximately 5 in-lbf of torque to turn the shaft when a proper amount of preload is applied to the spring.

Balancing the LBH rotor allows it to reach higher speeds before the fan blade separates. Balancing ensures low vibration and helps to maintain machine health. The EasyBalance is used for the LBH shaft. EasyBalance is a very simple to use software. It takes less than an hour to balance the shaft, and the shaft is balanced according to Eq. 30 , with G value of 2.5 from tables in [70].

$$Unbalance = \frac{9.54 * G * Mass}{RPM}$$

The rotor is balanced to around 5 g·mm at each plane, which is well below the required value, but it does not take much more time to accomplish. A laser pickup registers the speed of the shaft as it is spinning; a black piece of electrical tape is placed axially along the shaft as a contrast mark. Setting up the laser so that it reads each revolution correctly is difficult on the LBH shaft because it lacks large rotating surfaces; however it has worked successfully with the set-up seen in Figure 69 left.



Figure 69 balance hardware laser speed pickup setup left and operating balance rig (right) The aft end of the shaft is driven by belt from the balance machine motor. The motor speed is adjusted so that the shaft spins approximately 1/30th of testing speed or 1000 RPM. Figure 69 right shows the operating balancing rig.

The two balance planes on either side of the fan blade are cantilevered on the balance rig. It is important to correct the corresponding model in the software and update balancing dimensions, Figure 70.

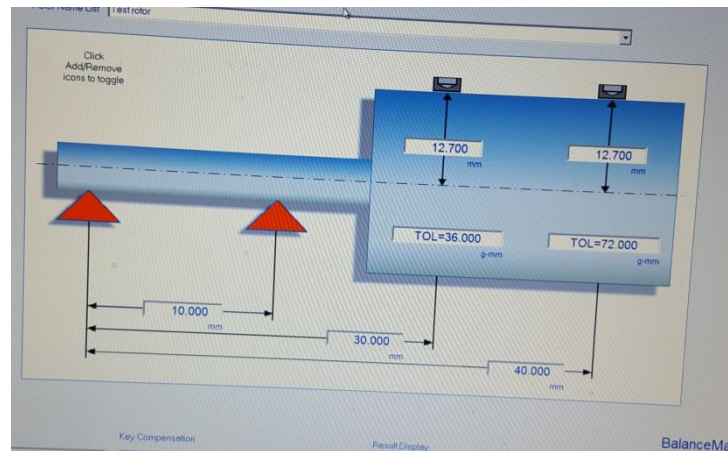


Figure 70 EeasyBalance rotor configuration

The balancing process is iterative; the operator will run the EasyBalance and add a weight lowering the unbalance with each iteration until the rotor is within an acceptable range. A subtractive balancing procedure can be accommodated as well however is not used for the balancing procedure.

The software will divide the balance plane into 16 segments for adding mass. This is necessary with the current rotor. There is also an offset angle option which allows for correction of the angle between the tape for the true center of the balance screw hole. To begin balancing the operator must correlate the balance holes to the segments on the computer and determine the offset angle. To do this first run the rotor with no weights on it. Zero the software using this unbalance, add a weight to one of the balance holes on the rotor and run the motor again. Using the results the operator can now determine the offset angle and correlate the balance screw holes to the segments in the software, Figure 71.



Figure 71 EasyBalance software results showing acceptable balance for both right and left planes

Not more than 2.5 grams is to be placed on any balance screw and every balance screw is to be discarded after a test run within the spin pit. The balance screw weights become fatigued with the large shear loads placed on them and if a screw fails and impacts the fan blade it will cause the fan blade to pre-maturely fail.

B.3 SpinIV Software and TC4 Controller:

The software and controller to the air turbine allow the operator to begin running a test, and will automatically brake or coast the turbine in the event of a fault. The controller operates the solenoid valves to the turbine by opening and closing the two secondary solenoid valves, and changing the flow rate of air through the turbine. A successful run is when the Constant Speed Testing button in the software is clicked and the turbine ramps up to speed and then automatically Brakes as the blade separates. This section will not detail how to operate the software, consult the manual; the section is intended on demonstrating how the software was used.

Open the software right click on the icon located on the desktop, and run as administrator. In the upper right hand corner of the application change the user to Administrator, the password is “spintest”. Next under the configure dropdown, select communication and input the IP address located on the back of the controller. This will change the user back to operator, log back in as Administrator.

First, the software must be calibrated to associate a rotational speed with a percentage the valve is open. To do this the operator will need to enter Manual Testing Mode and simply open the valve a specific percentage and input the resulting speed into the *Valve Offset Configuration*, Figure 72.

	Speed RPM	Valve %		Speed RPM	Valve %
1	8000	9.39	16	0	0.00
2	10001	11.82	17	0	0.00
3	11998	14.32	18	0	0.00
4	15000	18.28	19	0	0.00
5	18999	23.62	20	0	0.00
6	0	0.00	21	0	0.00
7	0	0.00	22	0	0.00
8	0	0.00	23	0	0.00
9	0	0.00	24	0	0.00
10	0	0.00	25	0	0.00
11	0	0.00	26	0	0.00
12	0	0.00	27	0	0.00
13	0	0.00	28	0	0.00
14	0	0.00	29	0	0.00
15	0	0.00	30	0	0.00

Read Download Clear

Figure 72 drive air control valve offset calibration

All 30 available offsets should be filled in with focus on the higher speeds. From the experience of testing the controller will ramp quickly and hunt for the set speed if *RPM Valve Offset Configuration* data is missing, this would not be ideal at higher speeds and shows low reliability in attaining a target speed.

For the constant speed testing set-up the Speed Request was constantly set to 40,000 RPM and the Ramp Request set to 1000 RPM/s. This worked well for non-controlled failure due to stress on the fan blades. The requested speed should be higher than the expected separation speed so that the rpm is increasing up until the time of separation.

In the General Test Parameters window set the Minimum valve offset. For the air compressor used in the testing it was set to -20%. This value controls how quickly the air turbine decelerates when it is first Braked. Leaving the value at -100% Brakes the air turbine so quickly that it can reach up to 10,000 RPM in the opposite direction. During normal testing the valve offset is not likely to exceed 40% open, so adjust the maximum and minimum values accordingly, with respect to the air compressor being used.

For the FBO testing four faults are used, categorized as Brake Faults. The first three come from the oil pump which is used to cool and lubricate the air turbine bearings. The faults are *oil level*, *oil pressure*, and *oil flow rate*. The fourth *brake fault* is tied to the trip wire in the fan case. The wire is tripped as the fan blade breaks off and opens the circuit by cutting the wire.

B.4 Fan Blade out Testing:

The fan blade out test requires events to happen in sequence as outlined by this section. This section will not discuss, fringe projection or setting up and calibrating high speed cameras. That

can be found in Chapter 5. This section should be referenced to after the lower bearing house is attached to the air turbine bulkhead shown in Figure 73.

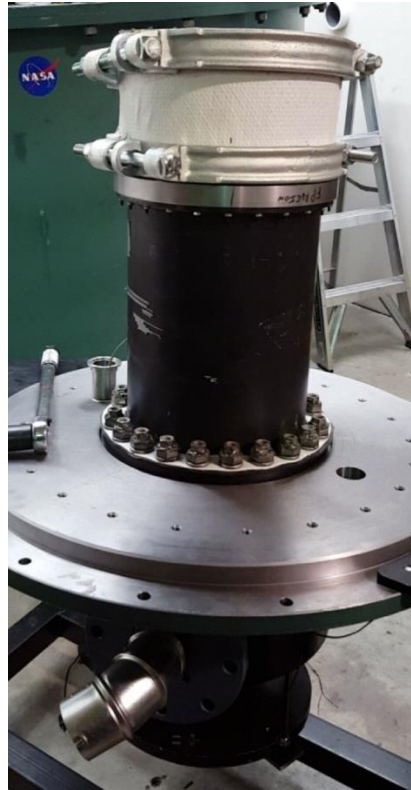


Figure 73 bearing housing assembly and test article installation on air turbine bulkhead
Begin by installing the fan case and then lifting the air turbine assembly on to the vacuum chamber. Connect the air hoses to the turbine. The hose coming straight out of the wall connects to the upper inlet on the air turbine. Connect the oil and air lines to the turbine, Figure 74.

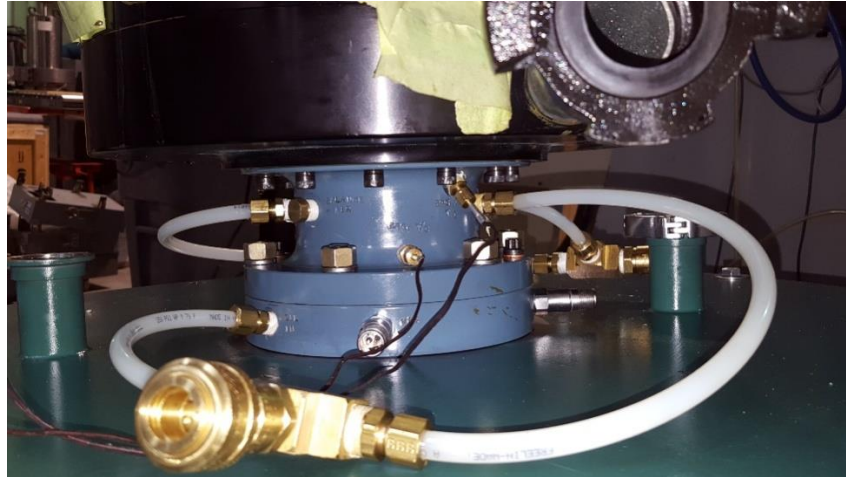


Figure 74 oil and airline quick connectors are labeled on the mounting base plate of the air turbine

In Figure 74, above the oil inlet and outlet hoses, the seal air, the thermocouples, and the accelerometers associated with the air turbine can be seen. The seal air is connected to an air pressure regulator which supplies are at 25 PSI. There is also an inlet for balance air, this test does not require as the test article does not exert any downward force on the driving quill shaft.

After the air turbine connections are made turn on the controller and the auxiliary controller power box. The auxiliary power box supplies the electrical power for the solenoid valves. Log into the SpinIV software and enable communication. Ensure that the constant speed testing has the correct values, and that all the other pertinent information is correct in the software, such as valve offset configuration and faults.

The accessory spin pit equipment (vacuum pump and oil pump) may now be powered up. Begin with the vacuum pump connected to the vacuum chamber as it will take about 15 minutes to fully vacuum down the chamber shown in Figure 75. Typically the vacuum reaches 2 kPa absolute for testing; however more accurate gaging equipment should be used for this determination.



Figure 75 vacuum pump accessory

Next, the seal air can be turned and then turn on and regulated to 30psi and the oil pump, Figure 76. Oil used is ISO grade 32 turbine oil, and can be purchased from Northern Tool and Equipment.



Figure 76 oil pump accessory

If the controller is set up so that it faults based on oil pressure or flow rate, it will now be able to clear those faults, since the oil pump is running. Ensure that the valves on the oil lines are opened prior to turning the pump on. The oil inlet hose has black tape on either end as an indicator.

Start up the 375 CFM diesel air compressor and allow it warm up. At this point all of the auxiliary equipment is running or ready to run. Ensure that the data acquisition software and any cameras are in the correct state. For the FBO testing a single trip wire was used to trip the cameras and the controller after the fan blade separates. Note that for the 375CFM air compressor the turbine is only running at about half capacity. To attain 100% torque and speed rating as listed from Barbour Stockwell Inc. (BSI) at least a 700CFM compressor must be used.

To begin the test, turn on the light inside the vacuum chamber for high speed viewing. Perform a safety check that all the correct equipment is running, that everyone is outside of the test cell and wearing hearing protection. Finally click on the *constant speed test* button to begin the test.

i. Posttest shut-down procedure

After the test has concluded turn off the equipment in the following order:

1. High intensity light inside vacuum chamber
2. Oil Pump
3. Air Compressor
4. Vacuum Pump
5. Seal Air

Before taking off the air hose ensure that there is no residual air pressure inside the hose. Allow the vacuum chamber dust and debris to settle before letting air back into it by slightly opening the valve on the vacuum pump.

If high heats are used for testing or other flammable test articles that could potentially cause a fire hazard post testing; the pit should be allowed to cool before air is reintroduced into the pit. To quicken the cooling process or to suppress fire hazard in case of a vacuum breach with article failure, an inert gas such as Helium or Nitrogen can be flooded into the pit.

Appendix C: Flat plate VARTM manufacturing

1. Ensure that aluminum plate is extremely clean
 - Use scraper and acetone to thoroughly clean the plate
 - Occasionally sand the plate (if scraper and acetone no longer effective)
2. Ensure that resin holes at ends are clean
 - Use drill with drill bit that fits perfectly in the nozzle to clean
 - Replace nozzles if they break or cannot be cleaned thoroughly
3. Cut glass fabric according to dimensions of desired test
 - Spin Match: final panels are 17.5" x 6.75" (cut 18" x 7" for safety)
 - Instrumented Target: final panels are 12" x 12" (cut 13" x 13" for safety)
 - Usually, 3 spin match panels or 2 IT panels can be made from one cut of fabric
 - Pick 6ply or 10ply (or other) and cut accordingly
4. Layer 1: thin green peel-ply
 - Dimensions: 28" long x just beyond the width of the panel
 - Cut squares out over resin holes to prevent stoppage (Figure 77)

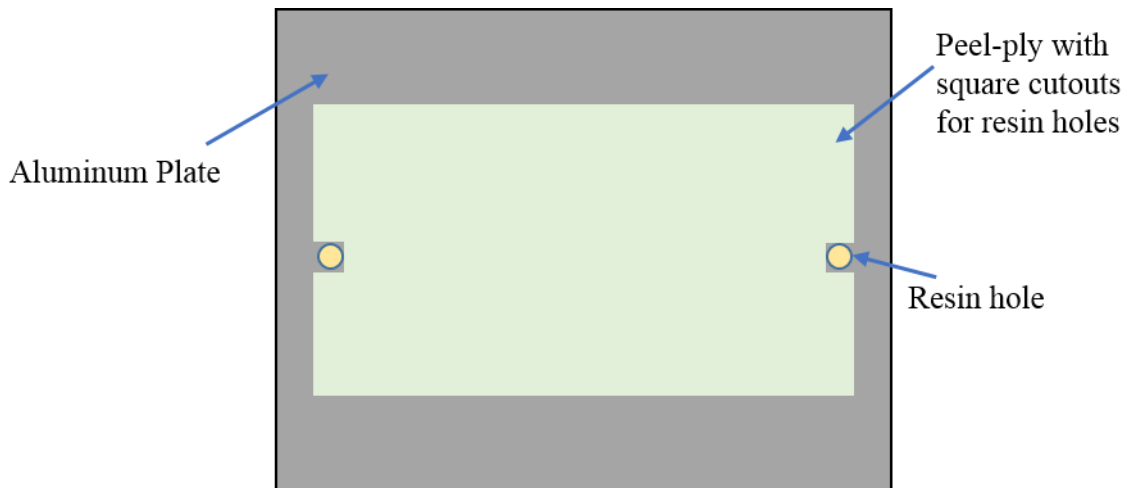


Figure 77 addition of peel-ply layer to Aluminum tool plate

5. Layer 2: panel
 - Stack all panels one on top of the other (Figure 78), ensure no fibers are protruding past the peel-ply

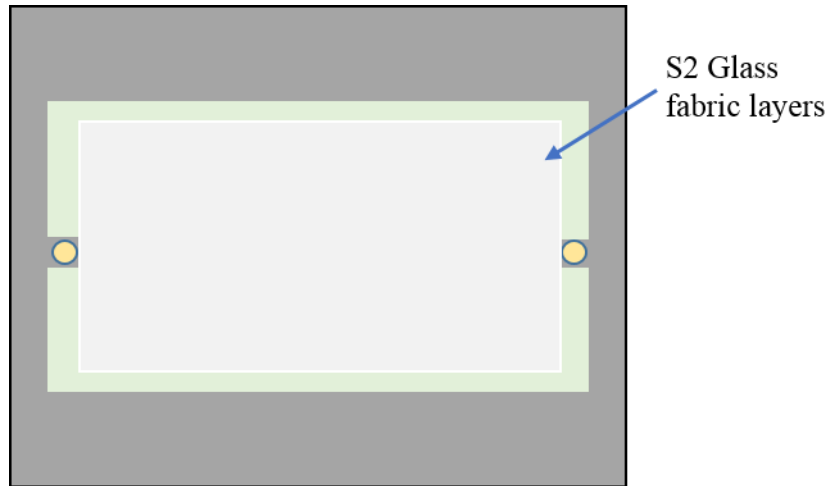


Figure 78 addition of fabric composite layers

6. Layer 3: white fabric

Dimensions: 28" long x just beyond the width of the panel

- Cut squares out over resin holes to prevent stoppage (Figure 79)

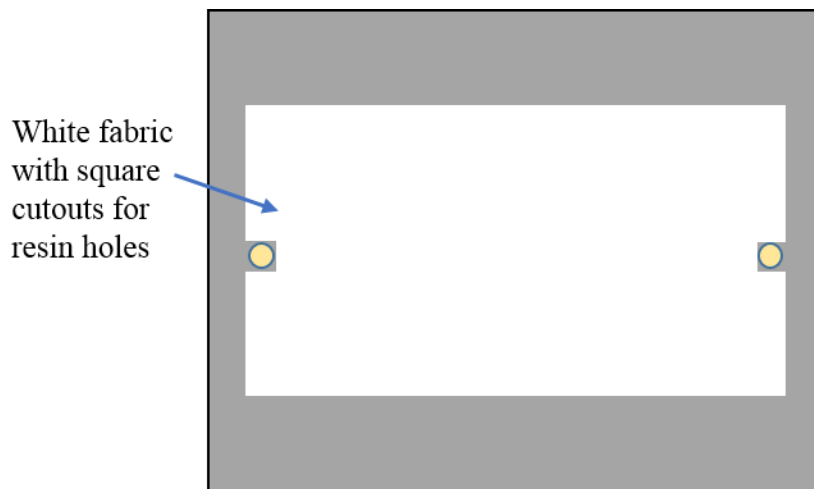
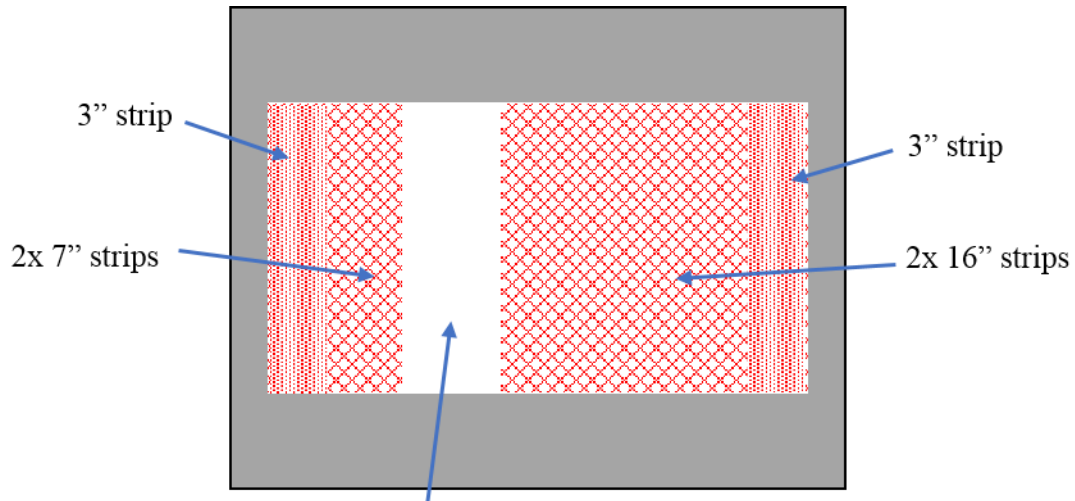


Figure 79 addition of permeable peel ply to top surface

7. Layer 4: red distribution media

Dimensions: 2 strips of 16" x width of panel, 2 strips of 7" x width of panel, 2 strips of 3" x width of panel (Figure 80)



Gap left for top and bottom layer resin fronts to converge which helps to minimize resin race tracking to the vacuum

Figure 80 addition of distribution media layer

8. Layer 5: vacuum bag

Dimensions: 25" x 32" (this is larger than the aluminum plate)

- Place yellow double-sided putty all the way around the panel (Figure 81)
- Avoid touching the putty with fingers, and keep the corners rounded
- Place the vacuum bag tightly over the putty (Figure 81)

*keep the white paper over the putty until the vacuum bag is ready to be

placed

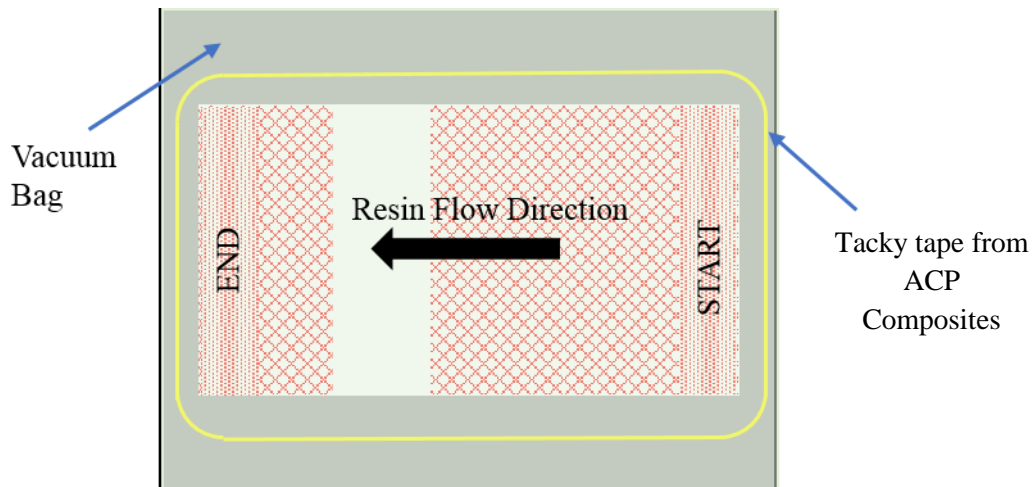


Figure 81 placement of tacky tape and vacuum bag – direction of flow specified

9. Resin Instructions

- Use the scale to weigh the resin/epoxy. Tare the scale with the bucket before pouring. The below calculation works well for the 5x5 S2 glass fabric

Amount of Resin (g) = (.436 g/in²)(Area of Panel)(# of Layers)

Amount of Epoxy (g) = (.3)(Amount of Resin)

- Stir for 4 minutes
- Place in vacuum box for 5-10 minutes

10. Resin Transfer Process

- For all steps; ensure that all connections are sealed with vacuum tacky tape (Figure 82)



Figure 82 depiction of high temp tacky tape used to seal hose connections

- Optional: attach pressure gage to one opening and the vacuum to the other to ensure there are no leaks
- Run one tube from the END opening to the vacuum
- Run one tube from the START opening; keep this tube kinked (Figure 83) and begin vacuuming



Figure 83 tube positioned for infusion

- Once vacuumed and no leaks occur, place kinked tube in resin bucket, THEN unkink
- Clamp tube to bucket as shown. *Tube CANNOT leave resin during process*
- Wait for all resin to flow through panel
- *Continuously check for leaks and air bubbles. Patch when necessary*

Patching tips:

- Tug on vacuum bag and smooth out wrinkles on putty using fingers
 - Clamp down a metal bar using C clamps on leak areas
 - Use caulks/glues (last resort)
- Once resin transfer is complete, kink resin tube and clamp the kink (Figure 84)



Figure 84 a method to kink tube when finished with resin

- Place entire setup in oven (vacuum must be outside – run tube through side vent)

11. Oven cure cycle

- Set oven to 60°C for 6 hours (set timer)
- At 2 hours, manually raise temperature to 94°C and turn off vacuum (close black switch first to prevent oil from slipping through pump and into the vacuum line)

REFERENCES

REFERENCES

- [1] G. Marsh, “Composites get in deep with new-generation engine,” *Reinf. Plast.*, vol. 50, no. 11, pp. 26–29, Dec. 2006.
- [2] J. Turnberg, “33-94 Analysis_08_12_FAA_certification.pdf.” Federal Aviation Administration, 2012.
- [3] T. P. Collins and E. A. Witmer, “Application of the Collision-Imparted Velocity Method for Analyzing the Responses of Containment and Deflector Structures to Engine Rotor Fragment Impact,” Aug. 1973.
- [4] B. Yang, “Blade containment evaluation of civil aircraft engines,” *Chin. J. Aeronaut.*, vol. 26, no. 1, pp. 9–16, 2013.
- [5] K. S. Carney, J. M. Pereira, D. M. Revilock, and P. Matheny, “Jet engine fan blade containment using an alternate geometry,” *Int. J. Impact Eng.*, vol. 36, no. 5, pp. 720–728, May 2009.
- [6] J. M. Pereira and B. A. Lerch, “Effects of heat treatment on the ballistic impact properties of Inconel 718 for jet engine fan containment applications,” *Int. J. Impact Eng.*, vol. 25, no. 8, pp. 715–733, 2001.
- [7] G. D. Roberts, J. M. Pereira, D. M. Revilock, W. K. Binienda, M. Xie, and M. Braley, “Ballistic Impact of Braided Composites with a Soft Projectile,” *J. Aerosp. Eng.*, vol. 18, no. 1, pp. 3–7, Jan. 2005.
- [8] G. D. Roberts, J. M. Pereira, M. S. Braley, W. A. Arnold, J. D. Dorer, and W. R. Watson, “Design and testing of braided composite fan case materials and components,” in *19th International Symposium on Air Breathing Engines, Montreal*, 2009.
- [9] K. F. Heermann, R. H. Kriksson, and K. R. McClure, “Study to Improve Turbine Engine Rotor Blade Containment,” DTIC Document, 1977.
- [10] S.L. Dixon, *Fluid Mechanics and Thermodynamics of Turbomachinery*, Fifth Edition. Elsevier Butterworth-Heinemann, 2005.
- [11] E. Dick, *Fundamentals of Turbomachines*, vol. 109. Dordrecht: Springer Netherlands, 2015.
- [12] L. C. Wright, N. G. Vitale, T. C. Ware, and J. R. Erwin, “High-Tip-Speed, Low-Loading Transonic Fan Stage. Part 1: Aerodynamic and Mechanical Design,” 1973.

- [13] M. E. Backman and W. Goldsmith, "The mechanics of penetration of projectiles into targets," *Int. J. Eng. Sci.*, vol. 16, no. 1, pp. 1–99, 1978.
- [14] W. Goldsmith, "Impact on Moving Structures and Effects of Striker Yaw and Tumbling," DTIC Document, 1993.
- [15] Jonas A. Zukas, *High Velocity Impact Dynamics*. Towson, Maryland: John Wiley & Sons, Inc., 1990.
- [16] A. VanderKlok, A. Dutta, and S. A. Tekalur, "Metal to composite bolted joint behavior evaluated at impact rates of loading," *Compos. Struct.*, vol. 106, pp. 446–452, Dec. 2013.
- [17] M. O. W. Richardson and M. J. Wisheart, "Review of low-velocity impact properties of composite materials," *Compos. Part Appl. Sci. Manuf.*, vol. 27, no. 12, pp. 1123–1131, 1996.
- [18] P. Robinson and G. A. O. Davies, "Impactor mass and specimen geometry effects in low velocity impact of laminated composites," *Int. J. Impact Eng.*, vol. 12, no. 2, pp. 189–207, 1992.
- [19] X. Haijun, L. Lulu, C. Guangtao, Z. Na, F. Yiming, and H. Weirong, "Impact response and damage evolution of triaxial braided carbon/epoxy composites. Part I: Ballistic impact testing," *Text. Res. J.*, vol. 83, no. 16, pp. 1703–1716, Oct. 2013.
- [20] D. Liu and L. E. Malvern, "Matrix cracking in impacted glass/epoxy plates," *J. Compos. Mater.*, vol. 21, no. 7, pp. 594–609, 1987.
- [21] W. J. Cantwell and J. Morton, "Comparison of the low and high velocity impact response of CFRP," *Composites*, vol. 20, no. 6, pp. 545–551, 1989.
- [22] D. Hull and T. W. Clyne, "An introduction to composite materials, 1996," *Camb. Solid State Sci. Ser.*
- [23] B. Z. Jang, L. C. Chen, L. R. Hwang, J. E. Hawkes, and R. H. Zee, "The response of fibrous composites to impact loading," *Polym. Compos.*, vol. 11, no. 3, pp. 144–157, 1990.
- [24] W. J. Cantwell, "The influence of target geometry on the high velocity impact response of CFRP," *Compos. Struct.*, vol. 10, no. 3, pp. 247–265, 1988.
- [25] S. S. Morye, P. J. Hine, R. A. Duckett, D. J. Carr, and I. M. Ward, "Modelling of the energy absorption by polymer composites upon ballistic impact," *Compos. Sci. Technol.*, vol. 60, no. 14, pp. 2631–2642, 2000.
- [26] D. Naik, S. Sankaran, B. Mobasher, S. D. Rajan, and J. M. Pereira, "Development of reliable modeling methodologies for fan blade out containment analysis – Part I: Experimental studies," *Int. J. Impact Eng.*, vol. 36, no. 1, pp. 1–11, Jan. 2009.

- [27] N. K. Naik and P. Shrirao, "Composite structures under ballistic impact," *Compos. Struct.*, vol. 66, no. 1–4, pp. 579–590, Oct. 2004.
- [28] C. Lawrence, K. Carney, and V. Gallardo, "Simulation of aircraft engine blade-out structural dynamics," 2001.
- [29] S. K. Sinha and S. Dorbala, "Dynamic loads in the fan containment structure of a turbofan engine," *J. Aerosp. Eng.*, vol. 22, no. 3, pp. 260–269, 2009.
- [30] T. J. Carter, "Common failures in gas turbine blades," *Eng. Fail. Anal.*, vol. 12, no. 2, pp. 237–247, 2005.
- [31] J. A. Mathis, "Design Procedures and Analysis of Turbine Rotor Fragment Hazard Containment," DTIC Document, 1997.
- [32] C. F. BLADES, "IMPACT RESISTANCE OF COMPOSITE FAN BLADES," 1974.
- [33] A. D. Lane, "Development of an Advanced Fan Blade Containment System," DTIC Document, 1989.
- [34] H. Xuan and R. Wu, "Aeroengine turbine blade containment tests using high-speed rotor spin testing facility," *Aerosp. Sci. Technol.*, vol. 10, no. 6, pp. 501–508, Sep. 2006.
- [35] Q. He, H. Xuan, L. Liao, W. Hong, and R. Wu, "Simulation methodology development for rotating blade containment analysis," *J. Zhejiang Univ. Sci. A*, vol. 13, no. 4, pp. 239–259, Apr. 2012.
- [36] Hagg, A.C., Sankey, G.O., "The Containment of Disk Burst Fragments by Cylindrical Shells," *J. Eng. Power*, pp. 114–123, Apr. 1974.
- [37] S. Sarkar and S. N. Atluri, "Effects of multiple blade interaction on the containment of blade fragments during a rotor failure," *Finite Elem. Anal. Des.*, vol. 23, no. 2, pp. 211–223, 1996.
- [38] R. Jain, "Prediction of transient loads and perforation of engine casing during blade-off event of fan rotor assembly," *Scientist*, vol. 91, p. 9945082491, 2010.
- [39] G. D. Roberts, "Private Communication," 2014.
- [40] M. Lucy, R. Hardy, E. Kist, J. Watson, and S. Wise, "Report on alternative devices to pyrotechnics on spacecraft," DTIC Document, 1996.
- [41] R. W. Hertzberg, "Deformation and Fracture Mechanics of Engineering Materials John Wiley and Sons," N. Y., 1996.
- [42] J. Zukas, "Impact dynamics," *John Wiley Sons Inc 605 Third Ave N. Y. N 10158 U 1982 452*, 1982.

- [43] W. Goldsmith, "Non-ideal projectile impact on targets," *Int. J. Impact Eng.*, vol. 22, no. 2, pp. 95–395, 1999.
- [44] M. V. Hosur, M. R. Karim, and S. Jeelani, "Studies on Stitched Woven S2 Glass/Epoxy Laminates under Low Velocity and Ballistic Impact Loading," *J. Reinf. Plast. Compos.*, vol. 23, no. 12, pp. 1313–1323, Aug. 2004.
- [45] L. J. Deka, S. D. Bartus, and U. K. Vaidya, "Damage evolution and energy absorption of E-glass/polypropylene laminates subjected to ballistic impact," *J. Mater. Sci.*, vol. 43, no. 13, pp. 4399–4410, Apr. 2008.
- [46] G. D. Roberts, D. M. Revilock, W. K. Binienda, W. Z. Nie, S. B. Mackenzie, and K. B. Todd, "Impact testing and analysis of composites for aircraft engine fan cases," *J. Aerosp. Eng.*, vol. 15, no. 3, pp. 104–110, 2002.
- [47] M. A. Sutton, S. R. McNeil, J. D. Helm, and Y. J. Chao, "Advances in 2-D and 3-D computer vision for shape and deformation measurements," *Top. Appl. Phys.*, vol. 77, pp. 323–372, 2000.
- [48] T. E. Cordova, P. L. Reu, and D. J. Vangoethem, "Measurement of steel plate perforation tests with digital image correlation.," Sandia National Laboratories, 2009.
- [49] V. Tiwari, M. A. Sutton, G. Shultis, S. R. McNeill, S. Xu, X. Deng, W. L. Fourney, and D. Bretall, "Measuring full-field transient plate deformation using high speed imaging systems and 3D-DIC," in *Proceedings of the society for experimental mechanics annual conference, Albuquerque*, 2009.
- [50] B. Gulker, R. Lureau, and D. Liu, "Investigation of Impact Response of Composites with Projection Moiré Enhancement," *Exp. Mech.*, vol. 54, no. 1, pp. 35–43, 2014.
- [51] S. A. Ritt and A. F. Johnson, "Load pulse determination in gas gun impact tests," in *Applied Mechanics and Materials*, 2007, vol. 7, pp. 259–264.
- [52] G. Li, D. Liu, and D. Schleh, "An Innovative Instrumented Projectile for Measuring Impact-Induced Force History," *Exp. Tech.*, 2015.
- [53] F. Plassard, J. Mespoulet, and P. Hereil, "Analysis of a single stage compressed gas launcher behaviour: from breech opening to sabot separation," in *8th European LS-DYNA Users Conference*, 2011, pp. 1–11.
- [54] A. A. Ramadhan, A. R. Abu Talib, A. S. Mohd Rafie, and R. Zahari, "High velocity impact response of Kevlar-29/epoxy and 6061-T6 aluminum laminated panels," *Mater. Des.*, vol. 43, pp. 307–321, Jan. 2013.
- [55] M. Denny, "Gas gun dynamics," *Eur. J. Phys.*, vol. 34, no. 5, pp. 1327–1336, Sep. 2013.
- [56] M. J. Moran, D. D. Boettner, H. N. Shapiro, and M. B. Bailey, *Fundamentals of Engineering Thermodynamics*, 7th ed. Wiley.

- [57] K. Wark Jr., *Thermodynamics*, 5th ed. McGraw-Hill.
- [58] X. Su and Q. Zhang, “Dynamic 3-D shape measurement method: a review,” *Opt. Lasers Eng.*, vol. 48, no. 2, pp. 191–204, 2010.
- [59] E. Hu and Y. He, “Surface profile measurement of moving objects by using an improved π phase-shifting Fourier transform profilometry,” *Opt. Lasers Eng.*, vol. 47, no. 1, pp. 57–61, 2009.
- [60] M. Takeda and K. Mutoh, “Fourier transform profilometry for the automatic measurement of 3-D object shapes,” *Appl. Opt.*, vol. 22, no. 24, pp. 3977–3982, 1983.
- [61] D. Bender, J. Schuster, and D. Heider, “Flow rate control during vacuum-assisted resin transfer molding (VARTM) processing,” *Compos. Sci. Technol.*, vol. 66, no. 13, pp. 2265–2271, Oct. 2006.
- [62] V. P. W. Shim, V. B. C. Tan, and T. E. Tay, “Perforation of Woven Fabric by Spherical Projectiles,” *Impact Waves Fract.*, vol. 205, pp. 293–306, Dec. 1995.
- [63] P. J. Hazell, G. J. Appleby-Thomas, and G. Kister, “Impact, penetration, and perforation of a bonded carbon-fibre-reinforced plastic composite panel by a high-velocity steel sphere: an experimental study,” *J. Strain Anal. Eng. Des.*, vol. 45, no. 6, pp. 439–450, 2010.
- [64] L. J. Deka, S. D. Bartus, and U. K. Vaidya, “Multi-site impact response of S2-glass/epoxy composite laminates,” *Compos. Sci. Technol.*, vol. 69, no. 6, pp. 725–735, 2009.
- [65] S.-W. R. Lee and C. T. Sun, “Dynamic penetration of graphite/epoxy laminates impacted by a blunt-ended projectile,” *Compos. Sci. Technol.*, vol. 49, no. 4, pp. 369–380, Jan. 1993.
- [66] K. S. Pandya, J. R. Pothnis, G. Ravikumar, and N. K. Naik, “Ballistic impact behavior of hybrid composites,” *Mater. Des.*, vol. 44, pp. 128–135, Feb. 2013.
- [67] D. Liu and W. J. Stronge, “Ballistic limit of metal plates struck by blunt deformable missiles: experiments,” *Int. J. Solids Struct.*, vol. 37, no. 10, pp. 1403–1423, Mar. 2000.
- [68] K. L. Presley, “Assessment of an Advanced Containment System,” DTIC Document, 1999.
- [69] J. S. Wilbeck, “Tests of spinning turbine fragment impact on casing models,” *Nucl. Eng. Des.*, vol. 77, no. 3, pp. 321–329, 1984.
- [70] I. R. D. Balancing, *Balance quality requirements of rigid rotors: the practical application of ISO 1940/1*. 2001.
- [71] Andy VanderKlok, A. Stamm, and Xinran Xiao, “Fan-blade-out Experiment at Small Scale,” *Submitted to Experimental Techniques*, 2016.

- [72] Andy VanderKlok, Andy Stamm, Matthew Auvenshine, Eryi Hu, James Dorer, Mike Pereira, and Xinran Xiao, "Investigation of high velocity impact responses of composite panels with a gas gun," *Unpubl. Manuscr.*, 2016.
- [73] B. W. Grimsley, R. J. Cano, P. Hubert, A. C. Loos, C. B. Kellen, and B. J. Jensen, "Preform characterization in VARTM process model development," 2004.
- [74] L. Meirovitch, *Elements of vibration analysis*. 1986. Singapore, McGraw-Hill. ISBN 0-07-041342-8.
- [75] S. S. Kessler, S. M. Spearing, M. J. Atalla, C. E. S. Cesnik, and C. Soutis, "Damage detection in composite materials using frequency response methods," *Compos. Part B Eng.*, vol. 33, no. 1, pp. 87–95, Jan. 2002.
- [76] D. R. Sanders, Y. I. Kim, and N. Stubbs, "Nondestructive evaluation of damage in composite structures using modal parameters," *Exp. Mech.*, vol. 32, no. 3, pp. 240–251, Sep. 1992.
- [77] O. S. Salawu, "Detection of structural damage through changes in frequency: a review," *Eng. Struct.*, vol. 19, no. 9, pp. 718–723, Sep. 1997.
- [78] R.C. Hibbeler, *Engineering Mechanics Dynamics*, 11th ed. New Jersey: Pearson Prentice Hall, 2007.
- [79] N. Jones, "Some comments on several phenomena in structural impact," *Am. Soc. Mech. Eng.*, pp. 153–167, 1995.
- [80] "MIL-P-46593A.pdf." .
- [81] W. J. Cantwell and J. Morton, "Geometrical effects in the low velocity impact response of CFRP," *Compos. Struct.*, vol. 12, no. 1, pp. 39–59, 1989.